CODEN:LUTEDX/(TEIE-5538)/1-117/(2025)

Industrial Electrical Engineering and Automation

Electric Drivetrain for Gas Turbines in Aviation Applications

Truls Nilsson
Niklas Frennfelt

Division of Industrial Electrical Engineering and Automation
Faculty of Engineering, Lund University

Electric Drivetrain for Gas Turbines in Aviation Applications

Truls Nilsson & Niklas Frennfelt

June 2025

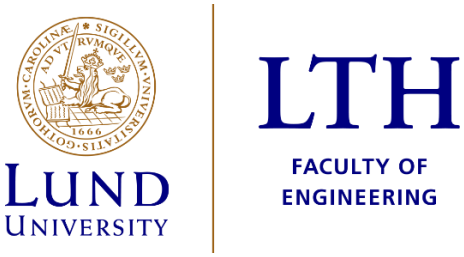

Master's Thesis in Electrical Engineering carried out at the

Division of Industrial Electrical Engineering and Automation and GKN Aerospace

Faculty supervisor: Mats Alaküla

Industrial supervisor: Lars Hoffmann

Examiner: Avo Reinap

ACKNOWLEDGEMENT

We would like to express our gratitude to those who have helped and guided us through this thesis. Thank you to Marcus, Dennis, Alexander, Örjan and Lasse at GKN Aerospace. Your encouragement and help with everything from component decisions to IT issues has been a huge help during the process. Our weekly meetings has really been joyful, sharing laughs and insightful conversations.

We also want to thank Johan, Max and Samuel at the Division of Industrial Electrical Engineering and Automation for the technical support in the lab as well as giving us valuable technical insights. Without you, this thesis would have been impossible. Finally, we also extend our deepest thanks to our faculty supervisor Mats Alaküla for being very generous with your time and knowledge, both supporting us through the project but also supporting us as persons when times were challenging.

ABSTRACT

Due to higher demands on the electrical systems in the aviation industry, the generation and distribution of electrical power, in aircrafts, needs to be researched and developed further. Key requirements include increased power capacity to meet future demands, a transition from AC to DC supply and an increased voltage level.

For power generation, a generator is coupled to the jet turbine which must endure a demanding environment with high temperatures and limited cooling capability due to the available coolants. By developing a simulation model of a PMSM operating as a generator, various machine designs, cooling strategies, and materials can be evaluated to identify configurations that meet the system requirements.

The transition to a DC supply, when AC has historically been used, and an increased voltage level, is an effect of the increasing power demand. But with the switch to DC supply, new onboard electronics is needed in order to convert it to AC and back. In order to maximize the on-board power generation, a over-modulation strategy is implemented. Electrical and thermal simulations are made in Simulink to evaluate possible solutions, including the over-modulation technique and the use of different types of transistors for the converter.

The PMSM model is developed in both Simulink, to ensure integration with the power electronics model, and in Motor-CAD, to enable more accurate loss estimation and thermal analysis. Simulation results indicate that, under the demanding environmental conditions and with the available cooling fluids of Jet fuel and a water-glycol mixture, slot cooling with direct contact to the windings is essential, without it, conventional materials are not suitable for the application. However, with materials such as samarium cobalt magnets and winding insulation materials with higher thermal capabilities, the machine achieves a significant thermal margin.

The over-modulation strategy developed is able to control the currents and voltages going from linear modulation to six-step modulation. The transition from linear to six-step is controlled with an algorithm in order to make it a smooth as possible. The over-modulation strategy works but the transition from linear modulation to six-step is not as smooth as desired. The thermal simulation showed that SiC transistors significantly reduces the cooling requirements compared to IGBTs. Partly due to its lower losses, but also because SiC transistors can operate under higher temperatures than IGBTs can. Although the performance differed a lot even between the two different SiC transistors used.

CONTENTS

1 INTRODUCTION

This chapter introduces the background of the thesis, outlines the premises and requirements on it is based on and the goals. The chapter starts off with a general background on the electrification of the aviation industry in Section 1.1. Section 1.2 gives a brief introduction of GKN Aerospace and Section 1.3 explains the more technical side of the background. The aims and objectives of the thesis are covered in Section 1.4, followed by the validation and limitations in Section 1.5 and 1.6. Finally, Section 1.7 covers the system requirements.

1.1 Background

In the field of aviation electrification, various approaches can be pursued to implement electrification. Three main frameworks have been proposed within this research area: all-electric aircraft (AEA), hybrid electric aircraft (HEA) and more electric aircraft (MEA). The AEA approach aims to fully electrify the aircraft, with propulsion driven by electric motors powered by an energy storage system, such as batteries.

In contrast the HEA approach also utilizes electric motors for propulsion but with the power generated by a conventional engine. The MEA framework, which is the framework used in this thesis, focuses on electrification of the secondary systems including hydraulic, pneumatic and actuation systems, by generating the electrical power from a conventional jet turbine through an electric machine operating as a generator.

The MEA electrification offers potential advantages in terms of redundancy, decrease in repair time, weight reduction, and system control which also can lead to improved environmental effect since weight reduction decreases the fuel consumption. By replacing pneumatic and hydraulic systems with fully electric alternatives, it is anticipated that both the overall system size and the risk of leaks or damage to surrounding components will be reduced [1].

1.2 GKN Aerospace

This thesis was conducted in a collaboration with GKN Aerospace, a global supplier of various aircraft systems including engine structures and electrical systems. As the trend toward increased electrification in future aircraft continues, there is a growing need to understand how this shift will impact the company's products. By exploring areas such as electrical machines and power electronics, GKN aims to build knowledge on how to adapt and integrate electric drivetrains into its systems. The current focus is primarily on learning and developing a deeper technical understanding.

1.3 Technical Background

In order to electrify the secondary systems, the aircraft's electrical power must increase. This is achieved by integrating a generator with higher power output than those previously used. Additionally, new power electronics capable of handling those power levels are required. In aircrafts there is a DC bus voltage

standard of 270 VDC which could be increased to 540 VDC (± 270 VDC) with a common ground potential of 0 V [2].

The conventional electrical systems in aircrafts are typically based on a 115 VAC bus, with power supplied by a constant-speed generator driven through a gearbox to maintain a fixed rotational speed. Transitioning from AC to DC power, enabled by power electronics, eliminates the need for this gearbox since the converter can output AC of the required frequency. Furthermore, increasing the system voltage from 115 VAC to 540 VDC allows for a reduction in cable size, thereby an overall decrease in the weight of the electrical system.

Since aircrafts are very sensitive to weight increase, the integration of new electric systems for replacement of the conventional systems must be well designed in order to improve the performance of the aircraft. The primary limitation of those systems are the thermal performance. Too high temperature increases in system components, significantly elevate the risk of damage, making thermal management a critical consideration in component design.

Since the weight of the system is of such importance, the system's size must be minimized which also includes minimizing the weight of coolant fluids, further increasing the challenges associated with thermal design. To reduce the weight of the coolant fluid, using jet fuel as a coolant is a desirable approach, as it leverages an existing fluid on the aircraft, eliminating the need for additional coolant and thereby reducing overall weight. Since jet fuel does not have as good heat transfer coefficients as water, it poses a challenge to the system design.

By implementing over-modulation, a technique where the voltage is increased more than traditional linear modulation, the power of the machine can be increased. Although over-modulation has a lot of advantages, it also has a few drawbacks including a control algorithm that is very complex due to its wide operation range, the fact that it should be able to control the currents in linear modulation, six-step modulation and transition region between the two states with a minimal amount of voltage transients. Six-step also introduces higher order harmonics, power losses, cooling demands which influences the expected outcome of the power density into the system.

In addition to the weight limitations, the environmental impact on the electrical system particularly concerning ambient temperature present a significant challenge. As the aircraft reaches high velocities, the resulting ram pressure increases the temperature of the air up to 100-120 °C around the electrical system while the temperature at launch operation can reach temperatures down to -40 °C. All these parameters must be taken into account in the investigation of what design that is the most preferable.

1.4 Aims and Objectives

The main objective for this thesis is to develop electric drive simulation models to identify the functional requirements and limitations of an electric drivetrain operating in a demanding environment. This includes the performance and the thermal management system of the electrical machine, covered in Section 1.4.1.

Development of a control strategy used to run the generator in linear modulation, over-modulation and a smooth transition between the two is also to be developed. This is important in order to optimize the use of the hardware. In addition to this, the power electronics to power the generator is also developed

and the performance and thermal management simulated. The control and power electronics are covered in Section 1.4.2.

1.4.1 Electric Machine

The main objective for the electric machine is to build a simulation model of a permanent magnet synchronous machine (PMSM) using Simulink and Motor-CAD. The machine simulation parameters are based on a compilation of system requirements including voltages, currents, coolant fluid specifications, thermal environment and should be operating with given drive cycles corresponding to operation during flight. Furthermore, the thermal behavior is modeled, where a simplified thermal model is constructed using Simulink. In addition to the simplified thermal model a more advanced model in Motor-CAD is used for testing different cooling topologies. Lastly, the developed PMSM models is validated towards a reference machine and then the models are tested in an environment corresponding to the application.

1.4.2 Control & Power Electronics

For the control & Power Electronics, the goal is to build simulation-model with the performance requirements and the parameters of a given reference machine into account. The primary objective is to develop a control strategy for the generator to run in both linear modulation and over-modulation with a smooth transition between the two states. Over-modulation is used to get more power out of the electrical machine and does so by developing a modulation method that allows controlled operation a higher voltages than can be reached by linear PWM modulation. A more complex control strategy is implemented in order to be able to measure and control the current in this state. The secondary objective is to implement a multi-level-converter, instead of commonly used 2-level-converter, into the simulation model. The main advantage with a multi-level-converter is that by dividing U_{dc} in to more levels the output currents ripple decreases. Although this comes with the cost of more components and a more complex switching sequence.

1.4.3 Research Questions

- What thermal management strategies are necessary to ensure reliable operation of a PMSM in aircraft environments with limited access to effective cooling fluids?
- What can a current control algorithm, which can go from linear modulation to six-step modulation and work in the transition region in between the two states, look like?
- What cooling capabilities are needed in order for the converter to operate without the transistors exceeding their maximum operating temperature?

1.5 Validation

In order to validate the simulation environment, measurements of a reference electric machine, are gathered and incorporated into the simulation model for comparison. This is used to check the validity of the simulation model and measure the discrepancy, between it and the real machine, allowing for necessary adjustments. The final simulation model and the existing machines are then tested using the drive cycles from GKN Aerospace to evaluate the performance.

1.6 Limitations

This thesis aims to develop and test simulation models of the power electronics and the electric machine. Hence, there will not be any development work on the physical construction such as modifications or prototyping.

The development of the electric machine model is restricted to a single topology, specifically a radial flux machine with internally mounted permanent magnets. It will be evaluated with different cooling topologies limited to the configurations available in the software Motor-CAD.

In order to be able to conduct real tests with the same components that are used in the simulations, only power electronics components used in consumer products are used both in specifying models and in conducting tests.

1.7 System Requirements

Below are the requirements for the electric machine and power electronics that are developed in this thesis.

1.7.1 Electric Machine

In order for the electric machine to function in the tough environment and produce enough power for the subsystems in the aircraft, system requirement is listed below.

Table 1: System requirement for the PMSM under study

Parameter	Value	Unit
DC-Link Voltage	540	V
Line to Line Voltage	382	V_{rms}
Output Power	100	kW
Peak Torque	150	Nm
Maximum Shaft Speed	17000	rpm
Ambient Temperature min	-40	°C
Ambient Temperature max	120	°C

The reference machine used for validation of the simulation models is designed for the automotive industry and has the following specifications.

Table 2: Magneti Marelli MGU011 nameplate specifications

Parameter	**Value**	**Unit**
Line to Line Voltage	350	V
Nominal current	380	A
Output Power	120	kW
Peak Torque	140	Nm
Maximum Speed	16000	rpm

1.7.2 Power Electronics

The requirements for the electronics are, just like the electrical machine, quite extreme due to the environment the systems operates in (surrounding air temperature can be from -40 °C, e.g. before take-

off in northern Sweden, to 120 ℃, during flight due to RAM pressure). The power electronics needs to be able to handle the system requirements of the PMSM which can be seen in **Table 1**. This, as well as the thin atmosphere at high altitudes, which decreases the ability to cool down the equipment with the surrounding air, and a jet engine, where some parts of the engine can reach over 1000 ℃, makes it a difficult problem to solve, even before the technical requirements has been introduced. The power electronic converter is further described in Section 2.2.

2 THEORY

This chapter presents the theoretical foundation underlying the development of the simulation models. It includes the mathematical modeling of the electric machine, power electronics, and control strategies, as well as the thermal models for both the electric machine and the power electronics. Furthermore, some material properties for the electric machine is explained. Additionally, relevant material properties of the electric machine are discussed to explain the thermal limitation.

2.1 Modelling of PMSM

The permanent magnet synchronous machine or PMSM, is assumed to consist of two main parts, a rotating part called the rotor and a stationary part called the stator as depicted in.

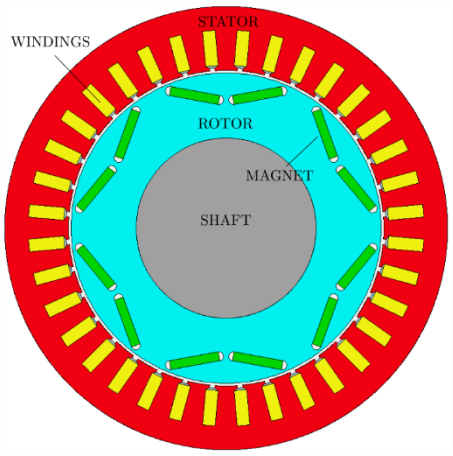

Figure 1: PMSM Geometry

The fundamental operational principle of a PMSM is based on the interplay between the magnetic field in the stator and rotor. By applying an electric current to the windings in the stator, a magnetic field is generated. By controlling the direction of the currents, a rotating magnetic field can be established. In contrast, the magnetic field in the rotor is produced by the permanent magnets which has a constant field. As the rotor is free to rotate and the two magnetic fields strive to align while the stator's magnetic field is rotating, a mechanical torque is produced.

There are two main types of magnet configurations in a PMSM, one with surface mounted magnets which has no saliency and one with internally mounted magnets which has a saliency. The main difference of the two types of magnet configurations is that the internally mounted magnet machine has a variable reluctance depending on the rotor position as seen from the stator windings, while the surface mounted magnet machine has a fixed reluctance independent of the rotor position.

This reluctance difference contributes to the magnetizing inductances in the direct axis (L_d) and quadrature axis (L_q) to have the relationship ($L_\mathrm{q} > L_\mathrm{d}$). This relationship can be utilized in order to produce additional torque called reluctance torque. In the scope of this thesis the magnets are embedded in the rotor which is taken into account in the mathematical model of the interior-mounted permanent magnet synchronous machine (IPMSM). [3]

In order investigate what the most suitable electric machine for a jet turbine application is, a suitable model of a machine is necessary. In this section, the dynamical and thermal behavior of the machine is mathematically described. The transformation from a three phase stationary reference frame to a two phase rotating reference frame is adopted using the power invariant Clarke's & Park's transformation [4].

2.1.1 Mathematical Model of a IPMSM

Since the machines used for validation are interior-mounted synchronous machines, the mathematical model is presented for this kind of machine. The model includes the influence from iron losses and magnetic cross-coupling and saturation but is not calculated analytically. The influence from these effects is instead added to the model through measurements on the real machine. Since the complexity of the mathematical model must be at a reasonable level for this thesis, the mathematical model is derived from the following assumptions:

- The magnets are interior-mounted.
- The stator windings are distributed and balanced.
- The stator windings are connected in a Y-configuration.
- The winding losses are only analytically calculated for resistive dc-losses.

2.1.1.1 Voltage equation

The voltage equation is crucial as it defines the voltage levels within the stator windings of the machine. To generate torque, a current must flow through the windings, which requires a voltage difference between the supply voltage and the machine. Additionally, it is essential to ensure that the machine voltage does not exceed the supply voltage, as this could potentially damaging the electronics and destabilizing the current control system. With a voltage supply of U_{dc}, the voltage limitation of the of the machine can be expressed as [5]:

$$|U_{dqs}| < \frac{U_{\mathrm{dc}}}{\sqrt{2}} \tag{2.1}$$

Where U_{dqs} is the voltage in stator windings expressed in the power-invariant *dq* domain where the subscripts *d* and *q* denote the direct and quadrature axis and *s* refers to the stator. The voltage limitation value is described in section 2.3.3. The stator voltage can be expressed as follows [3]:

$$\vec{u}_{dqs} = R_{\mathrm{s}}\,\vec{\imath}_{dqs} + \frac{d\vec{\psi}_{dqs}}{dt} \tag{2.2}$$

Where R_s is the stator resistance, $\vec{\imath}_{dqs}$ is the stator currents, $\vec{\psi}_{dqs}$ is the flux linkage between the stator and rotor. The flux linkage which is the magnetic coupling between the stator and rotor field can be expressed as follows [3]:

$$\vec{\psi}_{dqs} = L_{dq}\vec{\imath}_{dqs} + \vec{\psi}_{\mathrm{m}} \tag{2.3}$$

Where $\vec{\psi}_{\mathrm{m}}$ is the magnetizing flux from the permanent magnets which only contribute to the magnetic flux in the *d*-axis. L_{dq} are the inductances in *d*- and *q*-axis and since the type of machine investigated in this thesis is an IPMSM with salient poles, these inductances have the relationship [5]:

$$L_q > L_d \tag{2.4}$$

By including the saturation and magnetic cross-coupling effects of the iron core, the inductances are dependent on the stator currents. This dependency on currents is complicated to calculate analytically and is measured instead through experimental data and by finite element analysis. Therefore, the mathematical model neglects these effects and uses fixed inductances in the following equations.

Equation (2.2) can be written in its expanded form where the voltage in the *d*- and *q*-axis are expressed separately: [6] [7]

$$u_{ds} = R_{\mathrm{s}} i_{ds} + \frac{d\psi_{ds}}{dt} - \omega_{\mathrm{rel}} \psi_{qs} \tag{2.5}$$

$$u_{qs} = R_{\mathrm{s}} i_{qs} + \frac{d\psi_{qs}}{dt} + \omega_{\mathrm{rel}} \psi_{ds} \tag{2.6}$$

Where $\omega_{r_{\mathrm{el}}}$ is the electrical angular velocity. The flux linkage in *d*-axis ψ_{ds} is primarily due to the permanent magnets, while the flux linkage in the *q*-axis ψ_{qs} is influenced by the stator currents and can be expressed as follows:

$$\psi_{ds} = \psi_{\mathrm{m}} + L_d \cdot i_{ds} \tag{2.7}$$

$$\psi_{qs} = L_q \cdot i_{qs} \tag{2.8}$$

By combining equation (2.5) and (2.6) with (2.7) and (2.8), the voltage equations can be expressed as:

$$u_{ds} = R_s i_{ds} + \frac{d\psi_{ds}}{dt} - \omega_{\mathrm{rel}} \left(L_q \cdot i_{qs} \right) \tag{2.9}$$

$$u_{qs} = R_{\mathrm{s}} i_{qs} + \frac{d\psi_{qs}}{dt} + \omega_{\mathrm{rel}} (\psi_{\mathrm{m}} + L_d \cdot i_{ds}) \tag{2.10}$$

By applying a negative *d*-axis current, counteracts the flux produced by the permanent magnets, a technique known as field weakening which lowers the induced voltage and is used to keep the voltage below the voltage limitation.

The inductances, winding resistance and permanent magnet flux are dependent on the physical geometry of the machine and since the geometry is unknown these parameters must therefore be measured on the existing machines. The voltages and currents are set by the power electronics control system, hence the flux linkages are unknown values. In order to build the dynamic model, the flux linkage must be calculated which is done by rearranging equation (2.5) and (2.6). By moving the resistive voltage drop and the induced voltage to the left side of the equal sign, the change in magnetic flux can be derived which then can be integrated into the magnetic flux linkage as shown in equation (2.11) and (2.12).

$$\frac{d\,\psi_{ds}}{dt} = U_{ds} - R_{\mathrm{s}} i_{ds} + \omega_{\mathrm{r_{el}}} \psi_{qs} \rightarrow$$

$$\psi_{ds} = \int \left(U_{ds} - R_{\mathrm{s}} i_{ds} + \omega_{\mathrm{r_{el}}} \psi_{qs} \right) dt \tag{2.11}$$

$$\frac{d\psi_{qs}}{dt} = U_q - R_{\mathrm{s}} i_{qs} - \omega_{\mathrm{r_{el}}} \psi_{ds} \rightarrow$$

$$\psi_{qs} = \int \left(U_{qs} - R_{\mathrm{s}} i_{qs} - \omega_{r_{\mathrm{el}}} \psi_{ds} \right) dt \tag{2.12}$$

Since the flux linkage in *d*- and *q*-axis also can be expressed as equation (2.7) and (2.8), the currents in *d*- and *q*-axis can be derived as equation (2.13) and (2.14) which is how currents are calculated for the simulation model.

$$i_d = \frac{\psi_d - \psi_{\mathrm{m}}}{L_d} \tag{2.13}$$

$$i_q = \frac{\psi_q}{L_q} \tag{2.14}$$

2.1.1.2 Torque Equation

The electrical torque is produced by the interplay between the field from one rotor pole and the stator field and is divided in two components, the first being independent of the saliency of the rotor and is called Lorentz torque which is the torque produced from the permanent magnetic field in interplay with the stator field and is expressed as [5]:

$$T_{e_{\mathrm{Lorentz}}} = \psi_{\mathrm{m}} i_q \tag{2.15}$$

The second component is independent of the permanent magnet field and is called reluctance torque. The reluctance torque is generated not by the interaction between stator and rotor magnetic fields as in Lorentz torque production, but instead through the rotor aligning itself in a position that minimizes the magnetic reluctance in the magnetic flux path. The reluctance torque can be expressed with the inductances in *d*- and *q*-axis shown in the following equation [5].

$$T_{e_{\mathrm{Reluctance}}} = \left(L_d - L_q \right) i_{ds} i_{qs} \tag{2.16}$$

The two torque components together creates the electrical torque which is expressed as [5]:

$$T_{\mathrm{e}} = T_{\mathrm{e_{Lorentz}}} + T_{\mathrm{e_{Reluctance}}} = \psi_{\mathrm{m}} i_q + \left(L_d - L_q \right) i_{ds} i_{qs} \tag{2.17}$$

The total torque produced by the machine called the mechanical torque T_{mech} which is combined electrical torque from all the pole pairs and is defined as:

$$T_{\mathrm{mech}} = \frac{N_{\mathrm{p}}}{2} T_{\mathrm{e}} \tag{2.18}$$

Where N_{p} is the number of poles.

2.1.1.3 Motor dynamics

The relation between the rotational speed and mechanical torque is given by equation (2.19) where the load torque consists of two components. One is dependent on the viscous component and the second component is the external torque input. In this model, the viscous component is neglected and thereby the speed dynamics equation is formulated as [8]:

$$J \frac{d\omega_{\mathrm{r,mech}}}{dt} = T_{\mathrm{mech}} - T_{\mathrm{L}} \tag{2.19}$$

Where J is the inertia of the motor and T_{L} is the load torque. By rearranging equation (2.19), the mechanical rotor angular velocity $\omega_{\mathrm{r,mech}}$, can be calculated through integration and is given by:

$$\omega_{\mathrm{r,mech}} = \int \frac{T_{\mathrm{mech}} - T_{\mathrm{L}}}{J} \tag{2.20}$$

The angular velocity and the position of the rotor has the relationship:

$$\omega_{\mathrm{r,mech}} = \frac{d\theta_{\mathrm{r,mech}}}{dt} \tag{2.21}$$

Hence, the position of the rotor can be expressed as:

$$\theta_{r,mech} = \int \omega_{r,mech} \tag{2.22}$$

The electrical rotor position which is used for control of the stator field is given by:

$$\theta_{\mathrm{r,el}} = \frac{N_{\mathrm{p}}}{2} \cdot \theta_{\mathrm{r,mech}} \tag{2.23}$$

2.1.1.4 Winding Losses

Some of the input power is dissipated as heat in the stator windings due to the internal resistance in the conductor. This resistance is known as the DC resistance and is defined as:

$$R_{\mathrm{s}} = \frac{l_{\mathrm{w}}}{\sigma_{\mathrm{w}} A_{\mathrm{w}}} \tag{2.24}$$

Where $l_w$is the length of the winding, A_w is the cross section area of the winding conductor and $\sigma_w$is the electrical conductivity of the conductor. The resistive losses are often referred to as Joule losses and is expressed as [9]:

$$P_{\text{Joule}} = |I_s^2|R_s = (i_{ds}^2 + i_{qs}^2)R_s \tag{2.25}$$

Since the resistance of the conductors increases with temperature due to the temperature dependent conductivity, it's essential to account for this dependency. The relationship between temperature and resistance can be formulated as Equation (2.26),

$$R_s = R_{20^\circ C}\big(1 + \alpha(T^\circ - 20)\big) \tag{2.26}$$

Where $R_{20^\circ C}$ is the resistance of the conductor in 20 degrees Celsius, α is the temperature coefficient of the conductor and T° is the temperature of the conductor. [10]

2.1.1.5 Iron Losses

Iron losses in electrical machines primarily originate from two physical phenomena: eddy current losses and hysteresis losses. These two mechanisms occur concurrently within the magnetic core material, making it challenging to isolate and quantify them individually through experimental measurements. Consequently, they are typically grouped together under the term *iron losses*. One approach for estimating the iron losses in an electrical machine involves measuring the total power losses and subtracting the components that are less complex to calculate, such as dc resistive losses. Assuming that the remaining portion of the losses stems entirely from iron losses, a simplified loss model can be established fitting the measured losses to the specific operating point of the machine.

An alternative approach explored in this thesis involves estimating the core losses using the Steinmetz equation (2.27) , combined with approximations of the core geometry and flux density [10].

$$\rho_{\text{fe}} = (1 + k_c B^2)k_{\text{hyst}} f_{\text{el}} B^\alpha + 2\pi^2 k_{\text{eddy}} f^2 B^2 \tag{2.27}$$

In this context, ρ_{fe} denotes the iron loss density W/kg, while k_{hyst}, k_{eddy} and α are material-specific coefficients associated with hysteresis and eddy current losses, respectively. k_c is the minor hysteresis loop coefficient which is 0.65 as default value in Motor-CAD. The parameter f_{el} represents the electrical frequency of the magnetic field, and B is the magnetic flux density within the iron core.

As the Steinmetz equation provides the iron loss density while the equation also includes the magnetic flux density, which are both dependent on the geometry, an approximation of the core geometry is essential. The majority of the varying magnetic field occurs within the stator, as the rotating magnetic field is produced by the alternating currents flowing through the stator windings. Furthermore, this effect is enhanced by the interaction with the rotor's permanent magnetic field, which rotates relative to the stator and contributes to the time-varying magnetic flux experienced by the stator core. Hence the majority of the iron losses is produced in the stator and is thereby the only iron loss component of interest in this thesis.

Since the stator consists of both teeth and a yoke (also referred to as back iron), the iron losses are typically divided into tooth losses and yoke losses. To compute these losses accurately, both the geometry and the magnetic flux density in the respective regions must be estimated.

The geometry of the stator teeth can be approximated in a simplified manner using three parameters: tooth width w_{st}, tooth depth d_{st} and the stack length l_{stk} which together define a rectangular cuboid. In

machines utilizing hairpin windings, the stator slots are parallel, resulting in a non-uniform tooth width that differs between the tooth tip w_{stt} and the yoke connection w_{str} shown in **Figure 2**.

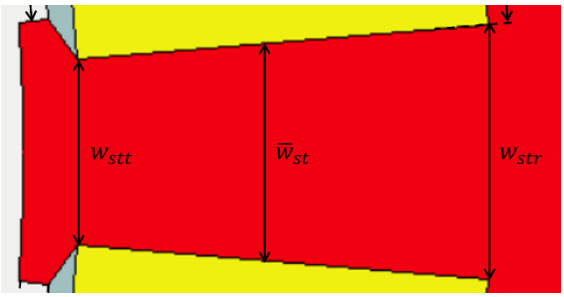

Figure 2: Stator tooth geometry.

To account for this, the effective tooth width can be approximated as three different cuboids with the widths at the tooth tip and yoke but also the average of the two widths which is given by:

$$\overline{w}_{\mathrm{st}} = \frac{w_{\mathrm{stt}} + w_{\mathrm{str}}}{2} \tag{2.28}$$

Using these widths, the cross-sectional area of the tooth in the radial direction, A_{st} and the volume V_{st} can be calculated as:

$$A_{\mathrm{st}} = w_{\mathrm{st}} \cdot l_{\mathrm{stk}} \tag{2.29}$$

$$V_{\mathrm{st}} = A_{\mathrm{st}} \cdot l_{\mathrm{stk}} \tag{2.30}$$

Likewise the stator yoke geometry can be parameterized into: yoke width w_{sy}, stator outer diameter D_{stator} and stack length L_{stk}. The stator yoke cross section area A_{sy} and volume V_{sy} can be expressed as:

$$A_{sy} = w_{sy} \cdot l_{stk} \tag{2.31}$$

$$V_{\mathrm{sy}} = \pi \cdot \left(D_{\mathrm{stator}} - w_{\mathrm{sy}}\right) \cdot A_{\mathrm{sy}} \cdot l_{\mathrm{stk}} \tag{2.32}$$

In order to calculate the total iron losses in those parts, the Steinmetz loss density has to be multiplied with the mass of the respective parts. The mass is dependent on the material's specific mass density ρ_{core} and is given by:

$$m_{\mathrm{tooth}} = V_{\mathrm{st}} \cdot \rho_{\mathrm{core}} \tag{2.33}$$

$$m_{\mathrm{yoke}} = V_{\mathrm{sy}} \cdot \rho_{\mathrm{core}} \tag{2.34}$$

The magnetic flux density in the stator tooth and stator yoke, denoted as B_{st} and B_{sy}, is defined as the magnetic flux ϕ passing through the radial cross-sectional area of the tooth and the tangential cross section area of the yoke. It can be expressed as:

$$B_{\mathrm{st}} = \frac{\phi_{\mathrm{st}}}{A_{\mathrm{st}} \cdot \mathrm{k_i}} \tag{2.35}$$

$$B_{\mathrm{sy}} = \frac{\phi_{sy}}{A_{\mathrm{sy}} \cdot \mathrm{k_i}} \tag{2.36}$$

The constant $\mathrm{k_i}$ represents the stacking factor of the laminated steel sheets. It is defined as the ratio between the effective height of the core and the total height of the laminated steel sheet, including both steel and insulation layers. Since magnetic losses are generated exclusively within the steel, only the cross-sectional area occupied by the steel is of interest. Consequently, the stacking factor must be accounted for in the calculation of the magnetic flux density to ensure accurate representation of the effective magnetic area.

Since the magnetic flux Φ is not directly measurable, it is calculated from the flux linkage ψ_{sdq}. The relationship between the magnetic flux and the flux linkage is given by [11]:

$$\psi = k_{\mathrm{w}} N_{\mathrm{tph}} \phi \tag{2.37}$$

Here, N_{tph} denotes the number of turns per phase, and k_{w} is the winding factor that accounts for the distribution and pitch of the stator windings. By rearranging the expression and transform it from the power invariant domain to amplitude invariant domain which corresponds to the physical amplitude of the flux, the magnetic flux from one pole ϕ_{pole} can be obtained:

$$\phi_{\mathrm{pole}} = \sqrt{\frac{2}{3}} \cdot \frac{|\psi_{sdq}|}{N_{\mathrm{tph}} \cdot k_{\mathrm{w}}} = \sqrt{\frac{2}{3}} \cdot \frac{\sqrt{\psi_d^2 + \psi_q^2}}{N_{\mathrm{tph}} \cdot k_{\mathrm{w}}} \tag{2.38}$$

The winding factor is defined as:

$$k_w = k_d \cdot k_p \tag{2.39}$$

Where k_d is the distribution factor and k_p is the pitch factor. The distribution factor is a measure of the resultant electromotive force (emf) of a distributed winding compared to a concentrated winding and is defined as: [10]

$$k_{\mathrm{d}} = \frac{sin\left(\frac{q\beta}{2}\right)}{qsin\left(\frac{\beta}{2}\right)} \tag{2.40}$$

Where, q is the number of slots per pole per phase and β is the slot angle and are defined as:

$$q = \frac{N_{\mathrm{s}}}{N_{\mathrm{p}} \cdot m} \tag{2.41}$$

$$\beta = \frac{\pi}{\frac{N_{\mathrm{s}}}{N_{\mathrm{p}}}} \tag{2.42}$$

Where, N_{s} is the number of slots and m is the number of phases.

The pitch factor k_{p} is a measure of the resultant emf of a short pitched winding compared to a full pitched winding and is defined as [12]:

$$k_{\mathrm{p}} = cos\left(\frac{\alpha}{2}\right) \tag{2.43}$$

Where α is the short pitch angle which is defined as:

$$\alpha = \pi\left(1 - \frac{W \cdot N_{\mathrm{p}}}{N_{\mathrm{s}}}\right) \tag{2.44}$$

Here, W is the coil span which is the number of slots that the coil is distributed over shown in **Figure 3**.

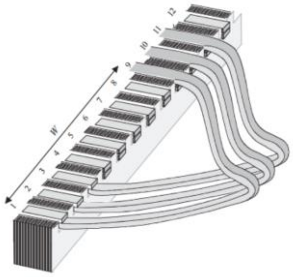

Figure 3: Illustration of coil span [10].

By substituting equation (2.44) into (2.43) the pitch factor can be expressed as:

$$k_{\mathrm{p}} = cos\left(\frac{\pi}{2}\left(1 - \frac{W \cdot N_{\mathrm{p}}}{N_{\mathrm{s}}}\right)\right) = sin\left(\frac{\pi}{2} \cdot \frac{W \cdot N_{\mathrm{p}}}{N_{\mathrm{s}}}\right) \tag{2.45}$$

In order to estimate the flux density in the stator tooth, the flux passing through the tooth can be estimated as the maximum flux passing through the tooth which can be calculated given by: [10]

$$\phi_{\mathrm{st}} = \frac{\phi_{\mathrm{pole}}}{2} \cdot \sin\left(\frac{\pi N_{\mathrm{p}}}{N_{\mathrm{s}}}\right) \tag{2.46}$$

Furthermore, the flux passing through the stator yoke is approximated as the maximum flux passing through the yoke which is half the pole flux since the flux is flowing from one pole to the two adjacent poles which divides the flux in two paths seen in **Figure 4**.

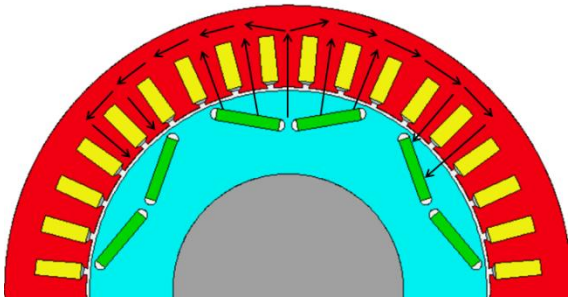

Figure 4: Flux path from one pole to the adjacent poles.

Hence the estimated stator yoke flux is given by:

$$\phi_{\mathrm{sy}} = \frac{\phi_{\mathrm{pole}}}{2} \tag{2.47}$$

2.1.2 Thermal Modeling

A thermal model of a PMSM is critical since the heat generated by the losses in the machine has a great influence on the performance and lifetime of the machine.

The thermal model developed in this thesis is implemented in Simulink using the lumped parameter modeling approach. This model is coupled with the mathematical electromagnetic model to estimate the temperature rise within the machine. However, since the electromagnetic model relies on measured data from a real machine and utilizes a rough estimation of iron losses, an additional lumped parameter thermal model is employed using Motor-CAD. This complementary model is based on the machine's approximated geometry and utilizes finite element analysis to provide higher accuracy in the loss estimation while it is independent of experimental data.

2.1.2.1 Lumped Parameter Thermal Model

The Lumped Parameter Thermal Model (LPTM) is an analytical approach of calculating the temperature rise at different nodes in the machine creating a lumped parameter network. By dividing the electric

machine into several subdomains, the geometry can be simplified which reduces the complexity of the parameter network. The geometry of these subdomains can be simplified to rectangular solids. The thermal behavior of the subdomain can be described by an electrical circuit by using the analogy between thermal and electrical conduction as depicted in **Figure 5**.

Each subdomain circuit consists of capacitors, resistors and sources connected in a network where the potential is equivalent to the average temperature in that node. The losses which generate the heat flux Q in the machine can be represented as a current source and the circuit resistance R describes the heat transfer ability between two sub-elements. Lastly, the capacitor C is equivalent to the thermal mass which stores the thermal energy [13].

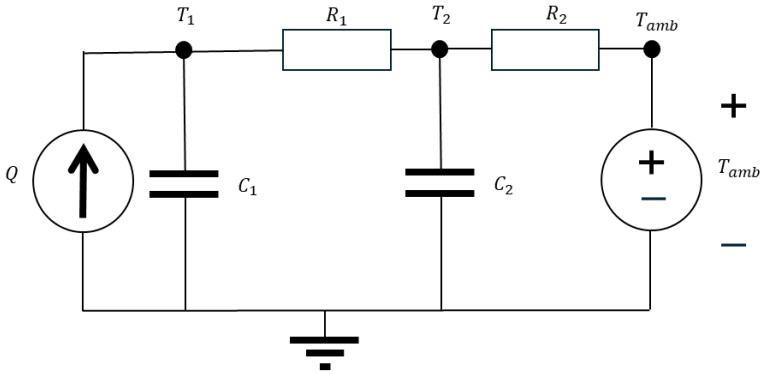

Figure 5: Example of a thermal circuit.

2.1.2.2 Thermal Resistance

Thermal resistance is categorized into four distinct types: conductive resistance, convective resistance, radiative resistance, and contact resistance. However, due to the limited timeframe and lack of detailed geometry information of the machines used for validation, only conductive and convective resistance is considered.

Conductive resistance characterizes heat transfer within a material, occurring in both solids and stationary fluids. This phenomenon can be mathematically expressed as follows:

$$R_{\mathrm{cd}} = \frac{l}{\lambda A} \tag{2.48}$$

Where l is the length between the nodes, A is the heat transfer cross sectional area and λ W/°C is the thermal conductivity [14].

Convective thermal resistance characterizes heat transfer through a moving fluid, which is inherently more complex due to its dependence on multiple factors, including motion of adjacent solids, surface structure, geometry, and forced flow, etc. The thermal resistance between a solid surface and the adjacent fluid can be expressed as [14]:

$$R_{\mathrm{cv}} = \frac{1}{\alpha A} \tag{2.49}$$

Where A is the surface area subjected to convection and α $\mathrm{W/m^2{}^\circ C}$ is the so-called heat transfer coefficient. The heat transfer coefficient value depends on several factors, including the viscosity of the coolant, its thermal conductivity, specific heat capacity, and flow velocity. Due to the heat transfer coefficient's dependence on numerous factors, accurately determining its value requires computational fluid dynamics (CFD) and finite element method (FEM) based approaches. Since this is very demanding and requires expertise in those methods, it is more convenient to use a value based on formulas from empirical studies [13] [14].

2.1.2.3 Thermal Capacitance

The thermal capacitor represents the heat capacity of respective parts in the nodal network. It is required in order to simulate the transient behavior temperature. The thermal capacity can be expressed as [13]:

$$C_{\mathrm{th}} = V_{\mathrm{n}} \rho_{\mathrm{v}} C_{\mathrm{p}} \tag{2.50}$$

Where V_{n} is the volume of the respective part, ρ_{v} is the density of the material and C_{p} $\mathrm{J/kg^\circ C}$ is the specific heat capacity of the material.

2.1.3 Temperature Limitations in PMSM

One of the key challenges in the design and operation of an electric machine is handling the thermal stress, particularly in environments with high ambient temperatures and limited access to effective cooling. High temperatures during operation can significantly affect the performance, reliability and lifetime due to thermal limitations in critical components such as winding insulation and permanent magnets. In order to manage this thermal stress, one approach is to the use high temperature materials.

2.1.3.1 Winding insulation

The insulation material around the conductors is applied in order to prevent a short circuit between the conductors in the windings of the stator. A short circuit between the conductors would lead to a significantly performance decrease. To prevent this, temperature limitations are used and where the commonly used insulation materials are divided into different classes as seen in **Figure 6**. The specified temperature limits correspond to an insulation lifetime of approximately 20 000 hours.

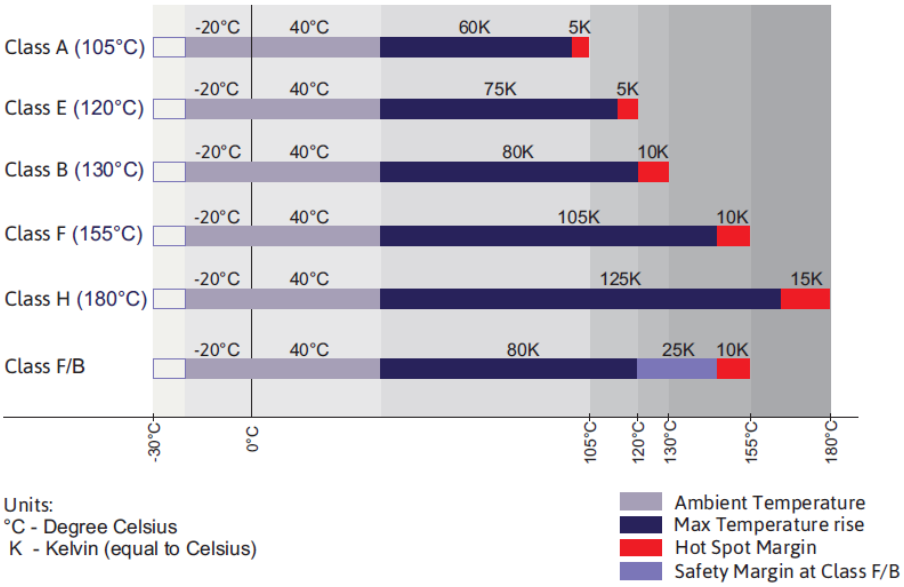

Figure 6: Insulation temperature classes gathered from Welkon Limited [15].

By using standard insulation materials from class H, a maximum temperature of the windings can reach up to 180 °C. This temperature is not recommended as nominal temperature and should be avoided. As seen in **Figure 6**, the hot spot margin for class H is 15 °C meaning that the insulation temperature should not exceed 165 °C. At reduced temperatures, the lifetime of the winding wire increases significantly, approximately doubling for every 10 °C decrease below the maximum operating temperature [16]. Therefore, the system requirement to operate at subzero temperatures does not appear to pose a significant limitation.

To enable operation at higher temperatures, alternative insulation materials must be employed. An interesting example is the S-2 glass-fibre insulation which can operate up to 425 °C [17]. It consists of numerous filaments, each with a diameter of approximately 0.005 mm, woven into a "knitted sock" around the conductor. The S-2 glass-fibre sock has a total thickness of approximately 0.075 mm which is comparable to conventional insulation coatings of roughly 0.1 mm which makes it possible to keep a similar fill factor in the slot. Since it is woven as a sock it is also flexible, making it suitable for windings.

2.1.3.2 Magnets for High-Temperature Operation

The most commonly used magnets for permanent magnet synchronous machines (PMSM) are rare earth magnets such as Neodymium-Iron-Boron (NdFeB) which has a high remanence B_r around 1.1 to 1.4 Tesla and a maximum operating temperature of around 150 °C [18]. An example of a grade 30UH NdFeB magnet is shown in **Figure 2**, which illustrates its demagnetization behavior.

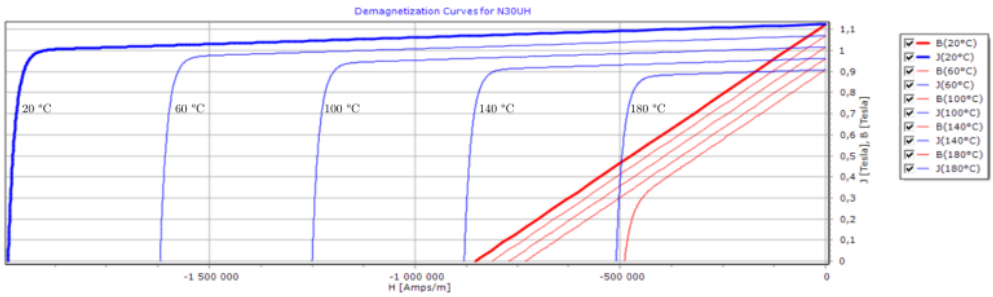

Figure 7: N30UH demagnetization curves from Motor-CAD. Intrinsic curve (blue) and normal curve (red).

The remanence is a measure of the magnetic polarization that remains in the magnet because of the hysteresis after the magnet has been fully saturated. In **Figure 7**, the remanence is shown as the intersection point of the demagnetization curves and the vertical axis. When the magnet is exposed to an external magnetic field (H) in the opposite direction, the magnetic flux density (B) is reduced since the fields are canceling each other out which can be seen as the red lines. The coercivity (H_c) is the external reverse field required to reduce the net flux density to zero.

If the magnet is being exposed to a too strong magnetic field in the opposite direction, there is a risk of demagnetization meaning that the remaining flux density in the magnet is zero after the external field is removed. The required field strength for this occurrence is called intrinsic coercivity (H_{ci}) which can be seen as the intrinsic curves intersect with the horizontal axis [19]. The magnet can also be partially demagnetized. This happens when the external field is strong enough to exceed the knee point of the intrinsic demagnetization curve.

The remanent flux density B_r and coercivity H_c & H_{ci} are all dependent on the temperature. With higher temperature, the remanent flux decreases and so does the coercivity, meaning that the performance of the magnet is reduced at higher temperatures. The risk for demagnetization is also increased since the knee point of the intrinsic demagnetization curve is significantly shifted towards the right at higher temperatures meaning that the external field is limited to a lower strength before exceeding the knee point.

Additionally, the magnet material has a Curie temperature which is the temperature where the magnet loses all its magnetic properties without any external field applied. In order to not risk the demagnetization, it is important to monitor the temperature of the magnet while not exceeding the field strength beyond the knee point.

For high temperature operation an alternative to decreasing the applied magnetic field is to use magnets which has a higher coercivity. An example of this is the Samarium Cobalt magnet which can withstand temperature up to 350 °C with a similar coercivity as the Neodymium magnets at 180 °C as seen in **Figure 8**. The Curie temperature of SmCo-magnets is approximately 700-850 °C compared to NeFeB-magnets with a curie temperature of 310-350 °C [18].

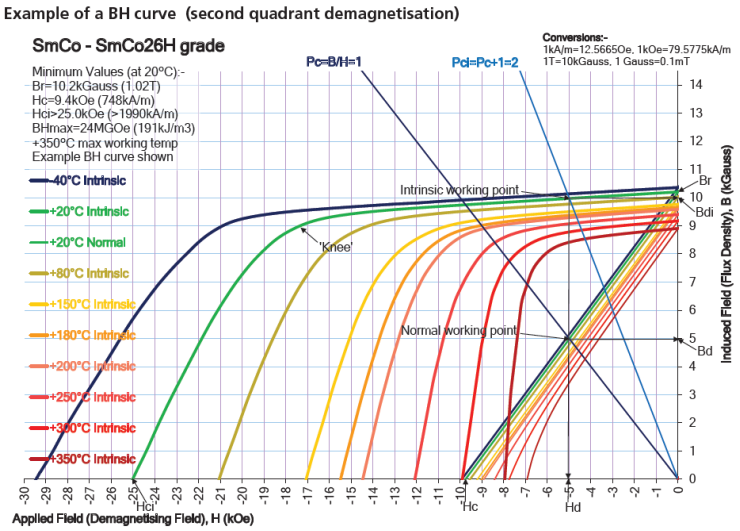

Figure 8: Demagnetization curve of SmCO26H [20].

One drawback of SmCo magnets is their lower remanence, typically in the range of 0.95–1.1 T, compared to NdFeB magnets. Additionally, SmCo magnets have a higher mass density [20]. As a result, achieving the same magnetic flux requires larger magnets with higher mass density which increases the weight of the machine and therefore the power density decreases.

Another alternative for high temperature operating magnets is Aluminum Nickel magnets which have a very high maximum operating temperature exceeding 500 °C [18]. The drawback of these types of magnets are their low coercivity of around 50 kA/m which makes it unsuitable for this type of electric machine operation since the applied magnetic field might exceed this limit.

As with winding insulation, subzero temperatures does not seem to have any negative effect on the magnets and does instead increase the remanence flux density, hence improving its magnetic properties [21].

2.1.4 Rough dimensioning of the electric machine

In order to build a geometry based model in Motor-CAD of the existing machine from Magneti Marelli, some assumptions must be made since the inside geometry is unknown. By utilizing some commonly used design approaches, the inside geometry can be estimated. The size of an electric machine is generally characterized by the torque per rotor volume which is also related to the airgap shear stress, σ. The shear stress which is the tangential torque producing force per rotor surface area depicted in and is defined as [11]:

$$\sigma = \frac{T}{2V_{\mathrm{r}}} = \frac{2T}{\pi D_{\mathrm{r}}^2 l_{\mathrm{stk}}} \tag{2.51}$$

Here, T is the peak torque, V_{r} is the volume of the rotor, D_{r} is the diameter of the rotor and l_{stk} is the axial length of the rotor. Typical values for the shear stress for a PMSM with rare earth magnets is approximately 14-42 kN/m^2 [11].

2.2 Power Electronic Motor Drive

Power electronics is used to control the currents and voltage that in turn are used to power the electrical machine. Section 2.2.1 and 2.2.2 goes in depth on the converter and its components. Why this exact type of converter is used, what materials are used, how it is controlled it and how its characteristics are affecting the overall system. The whole system operates in a very demanding environment with potentially very high temperatures. A model to handle these temperatures is presented in section 3.4.5 and section 2.2.3 includes the theory necessary for the calculations used.

2.2.1 Converter

The converter modelled in this thesis is used bidirectionally convert power between the AC and DC sides. This is because the bus is DC and the machine uses AC. Since the machine operates both as a motor and a generator the power goes both to and from the machine, and therefore both ways in the converter. As the generator has three phases, the converter also has to be able to control all three phases. A simple way to implement an AC/DC converter is to use diodes since they are cheap and reliable [22]. But to overcome the drawbacks of these, such as low power factor as well as increased harmonic content on the AC side and to provide bi-directionality, transistors are used instead [23]. A 3-phase converter has three half-bridges with U_{dc} on the DC side and the outputs (Phase A, B and C) of the half-bridges connected to the AC side as seen in **Figure 9**.

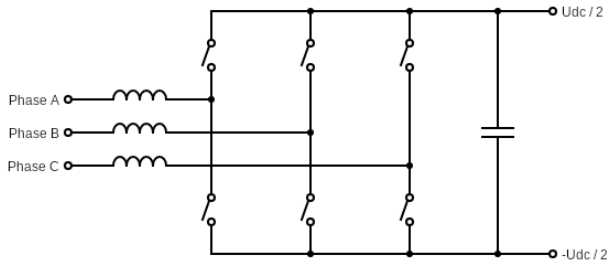

Figure 9: 3-level 2-phase AC-DC converter

2.2.2 Component Selection

Historically, Insulated Gate Bipolar Transistors (IGBT) are used for high power applications, but lately, Metal Oxide Semiconductor Field Effect Transistors (MOSFETs) based on Wide Bandgap (WBG) semiconductor materials, like Silicon Carbide (SiC) and Gallium Nitride (GaN), are used instead. These new materials allow transistors to reach higher heat tolerances, have shorter switching time and lower their switching losses [24].

2.2.3 Thermal Modeling

This section describes the theory behind thermal modeling from a transistor to the heat sink and do so only with regard to thermal resistance. For more advanced models, simulations can be made of the entire thermal impedance of higher orders also with radiation taken into account.

The losses in one transistor can in turn be split into two different parts: switching losses and conduction losses. These two types of losses are covered in section 2.2.3.1 and 2.2.3.2 respectively. The switching losses are calculated with energy lost, E_{on}, E_{off} and E_{rr}, while in the conduction losses section the losses are calculated with the power loss instead. This is due to the fact that the energy lost during a switching of a transistor usually is given in the datasheet. For conduction losses, the easiest approach is to do the calculation since the losses vary greatly on several different variables.

2.2.3.1 Switching losses

These two losses from the switching on and off a transistor are calculated with the following equations:

$$E_{\mathrm{on}} = U_{\mathrm{dc}} \cdot I_0 \cdot \frac{t_{\mathrm{on}}}{2} \tag{2.52}$$

$$E_{\mathrm{off}} = U_{\mathrm{dc}} \cdot I_0 \cdot \frac{t_{\mathrm{off}}}{2} \tag{2.53}$$

Where I_0 is the current through the transistor, t_{on} is the time, when the transistor switches on, from when the transistor starts conducting current until the voltage drop has reached $U_{S(on)}$ and t_{off} is the time, when the transistor switches off, from when the voltage drop has started to increase until the current has gone to zero.

For the losses associated with the reverse recovery current of the diode, which happens when a transistor is turned on, the following equation calculates the power lost.

$$P_{\mathrm{rr}} = U_{\mathrm{dc}} \cdot Q_{\mathrm{f}} \cdot f_{\mathrm{sw}} \tag{2.54}$$

But as stated in [5] Q_{f} has to be approximated and since E_{rr} is given in datasheets that is the value that is used in this thesis.

In a 2-level converter, in order to prevent a short-circuit, transistors always have to switch in pairs. This means that the total energy loss per switching event per phase can be calculated with the following equation:

$$E_{\mathrm{switch}} = E_{\mathrm{on}} + E_{\mathrm{off}} + E_{\mathrm{rr}} \tag{2.55}$$

2.2.3.2 Conduction losses

The conduction losses for one phase of the converter are calculated by the following equation:

$$P_{\mathrm{cond}} = V_{\mathrm{f0}} \cdot i + R_{\mathrm{s}} \cdot i^2 \tag{2.56}$$

V_{f0} is the voltage drop over the transistor when it is conducting but is not conducting any current, i is the instantaneous current and R_S is the resistance of the transistor and is given in the datasheet but is often temperature dependent [5].

2.3 Modulation and Control

The modulation of the phase potential reference, before it is sent to the converter, can be done in a multitude of ways. In this thesis Space Vector Pulse Width Modulation is used (SVPWM) which is introduced in Section 2.3.1. Section 2.3.2 covers linear modulation and Section 2.3.3 explains over-modulation and sex-step modulation.

2.3.1 SVPWM

Space Vector Pulse Width Modulation (SVPWM) is a modulation technique used to achieve precise control of the output voltage waveform [25]. It is especially superior to other simpler modulation techniques when it comes to voltage quality, harmonic content reduction, and efficiency optimization. It does this by representing the three-phase output voltage of the converter in a two-dimensional space vector plane, see **Figure 11** [26].

The three phases of the converter, with two transistor states per phase (high or low), gives rise to $2^3 = 8$ combinations. These eight combinations can be represented as eight different vectors which can be used in SVPWM to control the output voltage waveform, creating the current that in turn control the motor. These eight states can be seen in **Figure 10** and an important detail to note is that both the (0,0,0) and the (1,1,1) states have all their phases short-circuited to one potential (high and low respectively). These two states are called zero-states and does not create any currents since there is no potential difference between any of the states.

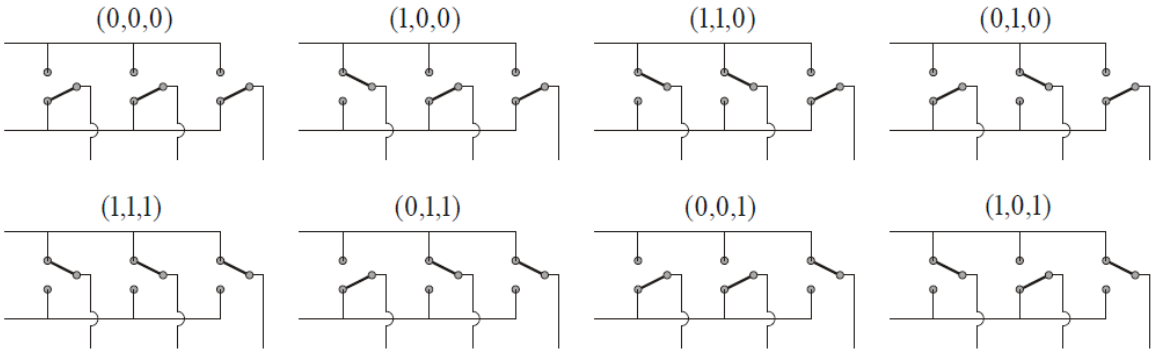

Figure 10: Eight switching combinations determined by the state of the three phases [5].

In **Figure 11** the vector created by each state and the two zero vectors in the middle. Even though both vectors gives the same outcome, both are used. This is because any one of these two equations can be switched two from the other six by only switching on state (one transistor pair) thus minimizing losses. The magnitudes and angles of the eight vectors can be described by the following equations:

$$\vec{u}(1,0,0) = \sqrt{\frac{2}{3}} \cdot U_{\mathrm{dc}} = -\vec{u}(0,1,1) \tag{2.57}$$

$$\vec{u}(0,1,0) = \sqrt{\frac{2}{3}} \cdot U_{\mathrm{dc}} \cdot e^{j\frac{2\cdot\pi}{3}} = -\vec{u}(1,0,1) \tag{2.58}$$

$$\vec{u}(0,0,1) = \sqrt{\frac{2}{3}} \cdot U_{\mathrm{dc}} \cdot e^{j\frac{4\cdot\pi}{3}} = -\vec{u}(1,1,0) \tag{2.59}$$

$$\vec{u}(0,0,0) = 0 = \vec{u}(1,1,1) \tag{2.60}$$

Switching between all these vectors at a high frequency, creates an average vector with an angle and magnitude of our choice.

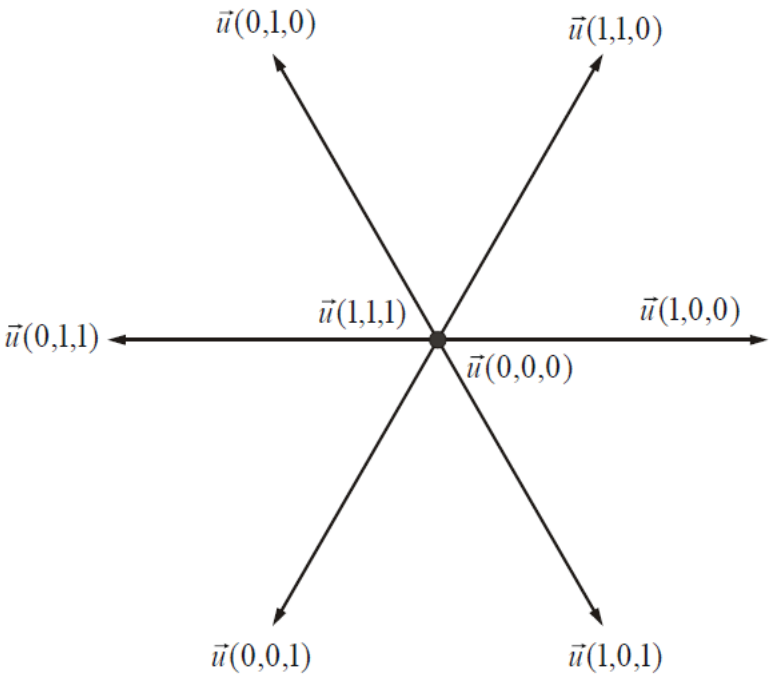

Figure 11: Voltage vector from a 3-phase 2-level converter [5].

2.3.2 Linear Modulation

2.3.2.1 Sinusoidal modulation

The simplest way to modulate the currents after a given input signal is with a triangular carrier wave with an amplitude of half of U_{dc} and a frequency of half the switching frequency. By comparing the triangular carrier wave with the voltage of a certain phase, this decides the output of that certain phase according to the following equation:

$$U_{out} = \begin{cases} \frac{U_{dc}}{2}, U_n > U_{cw} \\ -\frac{U_{dc}}{2}, U_n < U_{cw} \end{cases} \quad (2.61)$$

Where U_{out} is the output current from the modulator to the converter, U_n is the voltage reference of phase n and U_{cw} is the voltage of the triangular carrier wave. A high switch position outputs a voltage of +270V and a low switch position outputs a voltage of -270V, as can be seen in **Figure 12** for phase A.

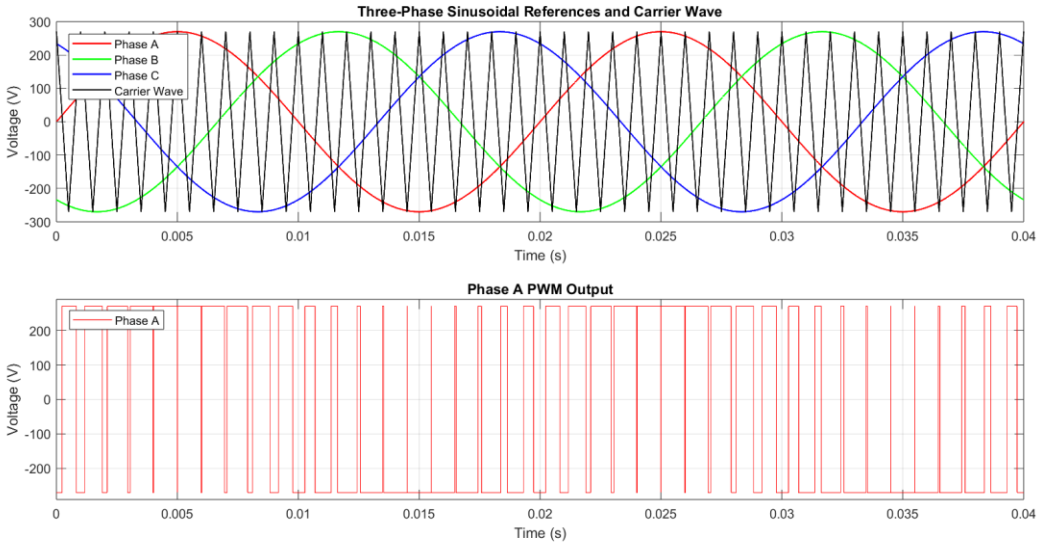

Figure 12: Three-Phase Sinusoidal References with the Carrier Wave and the output of Phase A.

2.3.2.2 Symmetrical Modulation

As can be seen in **Figure 12**, the entire available U_{dc} is not utilized. When any one of the three phases reaches its peak, the other two phases are far from their peak value. This issue arises because of sinusoidal modulation. If the zero potential, the neutral point for all three voltages, is modified with a so called zero-sequence voltage injection, the available DC-link voltage can be utilized to a larger extent. One way of doing this is called “Symmetrical Modulation” where the added zero-sequence voltage is calculated by:

$$v_0 = \frac{max(u_a^*, u_b^*, u_c^*) + min(u_a^*, u_b^*, u_c^*)}{2} \quad (2.62)$$

Where v_0 is the zero potential, v_a^*, v_b^* and v_c^* are the reference voltages for Phase A, B and C respectively. v_0 can be seen in **Figure 13** as the orange wave. The three dashed lines in **Figure 13** shows the phase potential references for Phase A, B and C if the zero potential is subtracted from the phase voltage references. The signals rise and fall faster and the maximum amplitude of all three phases decreases. A consequence of this is that the amplitude of the three signals can be increased with an additional 15.4% without the amplitude of the signal exceeding U_{dc} [27]. The three solid lines show the result of adding 15.4 % to the dashed lines.

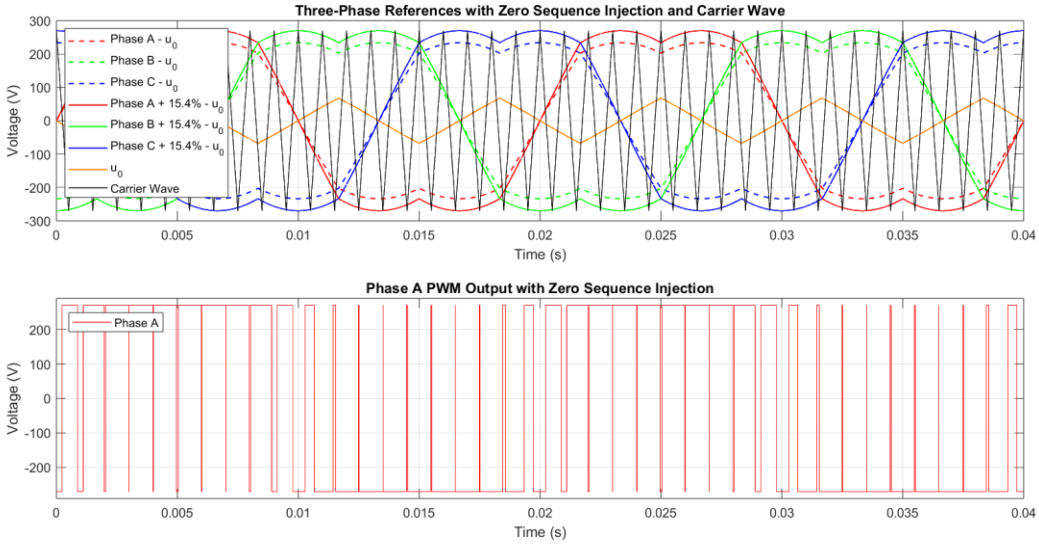

Figure 13: Three-Phase References with Zero Sequence Injection, the Carrier Wave and the output of Phase A.

2.3.3 Over-modulation and Six-step-modulation

The maximum phase voltage when using linear modulation, for a power invariant system, is $\frac{U_{\mathrm{dc}}}{\sqrt{2}}$ but a voltage space vector has a magnitude of $\sqrt{\frac{2}{3}} \cdot U_{\mathrm{dc}}$ as seen in **Figure 14**. When trying to push an electrical machine to its absolute limit, six-step-modulation can be used. The reason that linear modulation clamps the voltage at $\frac{U_{\mathrm{dc}}}{\sqrt{2}}$ is because any voltage vector with a magnitude exceeding that voltage would not be able to reach the reference for every angle. To circumvent this, over-modulation can be used [28].

2.3.3.1 Over-modulation

The term over-modulation refers to when the voltage reference vector is larger than $\frac{U_{\mathrm{dc}}}{\sqrt{2}}$ which constrains the use of linear modulation. Voltage references vector lengths above $\frac{U_{\mathrm{dc}}}{\sqrt{2}}$ can be put into two different

categories. The range between $\frac{U_{\mathrm{dc}}}{\sqrt{2}}$ and $\sqrt{\frac{2}{3}} \cdot U_{\mathrm{dc}}$, in this thesis called over-modulation. As well as voltage references with a magnitude of $\sqrt{\frac{2}{3}} \cdot U_{\mathrm{dc}}$ and above, usually called six-step-modulation.

Six-step-modulation is a completely different way of controlling the currents going into the machine. Although it is different, it is not that difficult to implement. The primary challenge lies in the so-called over-modulation, the transition between linear modulation and six-step-operation. The reason for this is that when the reference voltage vector (the red vector in **Figure 14**) is not constrained by the black hexagon that represents the available voltage vectors, i.e. its angle is smaller than $\frac{\theta_{\mathrm{e}}}{2}$, the modulator can be operated in linear operation just like when the magnitude is smaller than or equal to $\frac{U_{\mathrm{dc}}}{\sqrt{2}}$. But when the magnitude is bigger than the side of the hexagon at that specific angle, i.e. its angle is greater than $\frac{\theta_{\mathrm{e}}}{2}$, regular linear modulation is not able to control the reference vector. The over-modulation strategy that is used in this thesis is only one way of doing it, so bear that in mind.

The over-modulation strategy used in this thesis is a single-zone strategy where the voltage reference vector magnitude is modified and the angle is not.

$$U_{\mathrm{om}}^{*} = \begin{cases} U^{*}, |U^{*}| < U_{\mathrm{max}} \\ U_{\mathrm{max}}, |U^{*}| \geq U_{\mathrm{max}} \end{cases} \tag{2.63}$$

$$U_{\mathrm{max}} = \frac{\frac{U_{\mathrm{dc}}}{\sqrt{2}}}{cos\left(\theta_{\mathrm{sector}} - \frac{\pi}{6}\right)} \tag{2.64}$$

$$\theta_{\mathrm{sector}} = \theta_{\mathrm{el}}\ mod\left(\frac{\pi}{3}\right) \tag{2.65}$$

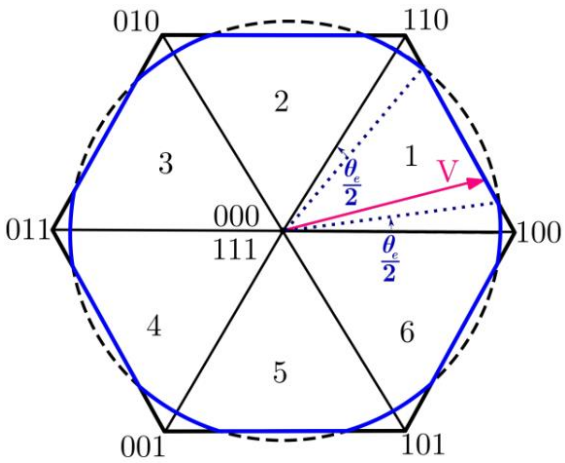

Figure 14: Voltage space vector and the periphery that the space vector traverses [28].

2.3.3.2 Six-step-modulation

In six-step-modulation the voltage magnitude of each modulated phase voltage is the maximum phase to phase voltage possible with SVPWM, $\sqrt{\frac{2}{3}} \cdot U_{\mathrm{dc}}$. This means that zero vectors are not used at all, which ensures maximum use of the available voltage [29]. Each phase doesn't switch back and forth in six-step operation compared to linear operation as can be seen in the lower graph of **Figure 12** and **Figure 13**, instead Phase A during six-step operation looks like the lower graph of **Figure 15**.

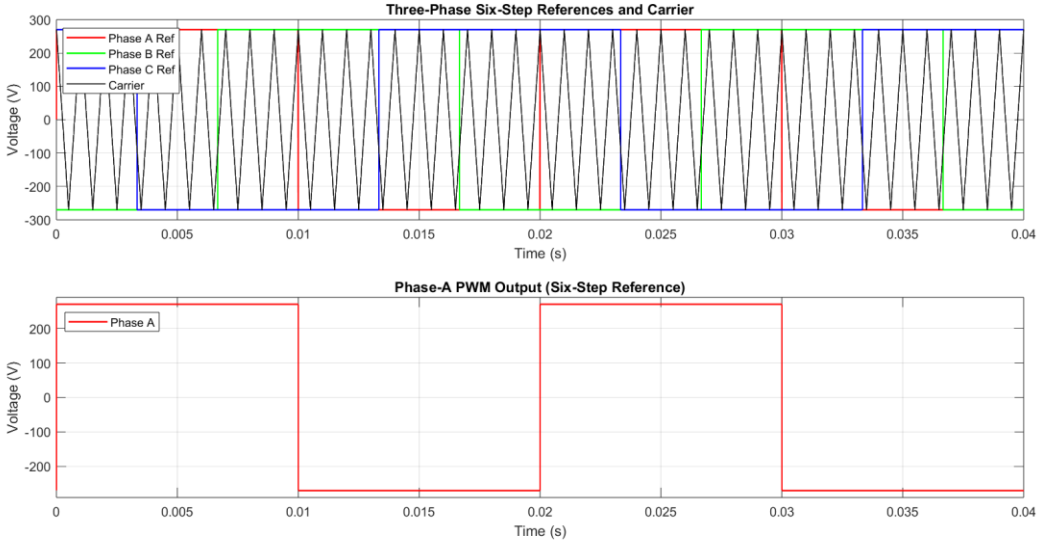

Figure 15: Theoretical Three-Phase Six-step Reference with the Carrier Wave and the output of Phase A.

3 SIMULATION MODEL DEVELOPMENT

The simulation model is developed using both Simulink and Motor-CAD, each serving complementary roles. Simulink is employed to construct a complete system-level model, integrating the power electronics and the PMSM. In contrast, Motor-CAD is utilized for detailed analysis of machine losses and thermal behavior, leveraging its capabilities in finite element analysis (FEA).

The Simulink model is based on the mathematical representations of the PMSM and relies on measurement data to represent an existing machine. However, with missing measurement data, the data from the Motor-CAD model is used, approximating the parameters such as inductances of the reference machine despite the limited access to experimental measurements.

This section outlines the data collection of the reference machine, followed by the Motor-CAD design process, which is based on a combination of the measurements and geometrical assumptions. Additionally, the development of a Simulink model representing both the power electronics and the PMSM is explained. Finally, the model validation process is presented, where the performance of the simulated PMSM is compared against measurement data.

3.1 Electric Machine Data Collection

To develop an accurate simulation model which can be validated with the reference machine geometrical and electrical data is crucial. In this case, it is assumed that no detailed information is available about the electric machine beyond its external dimensions. As a result, the model is built using estimations for internal parameters, such as material properties and internal geometry. Where possible, these assumptions are supported by available documentation or measurements. The materials employed in the models are listed in **Table 3**.

Table 3: Materials of PMSM model

Machine Part	Material
Stator Iron	M350-50A
Rotor Iron	M350-50A
Magnets	N30UH
Windings	Copper
Winding Insulation	Motor-CAD default material
Liner	Motor-CAD default material

3.1.1 Outer Dimension Measurements

Due to the inaccessibility of the internal geometry, only the external dimensions are measured. These dimensions was measured using a caliper and measurement tape seen illustrated in **Figure 16** and the dimensions are listed in **Table 4**.

Figure 16: Outer diameter and length measurement of MGU011 using a caliper and measurement tape.

Table 4: Measurements of MGU011 outer geometry.

Dimension	Value	Unit
Machine Outer diameter (D_m)	210	mm
Machine Length (l_m)	240	mm

3.1.2 Determination of pole-number

The number of poles in the machine can be determined by measuring the frequency of the phase-to-phase voltage waveform while spinning the shaft with a known constant speed due to the relationship between electric and mechanical frequency which is expressed as:

$$f_{el} = f_{\text{mech}} \cdot \frac{N_{\text{p}}}{2} \tag{3.1}$$

Where, N_p is the number of poles. With a known rotational speed of the shaft and a measurement of the voltage waveform, the number of poles were calculated to be 6 poles.

3.1.3 Determination of Permanent Magnet flux Linkage

To determine the flux linkage from the permanent magnets, a no-load test was conducted. During no-load, no currents were applied to the machine, meaning that the induced voltage on the terminals are only dependent on the magnetic flux given by equation (2.10). During this test, the rotor was manually rotated at approximately 217 rpm while the line-to-line voltages were measured and recorded for post-processing. The resulting voltage waveform is illustrated in **Figure 17**.

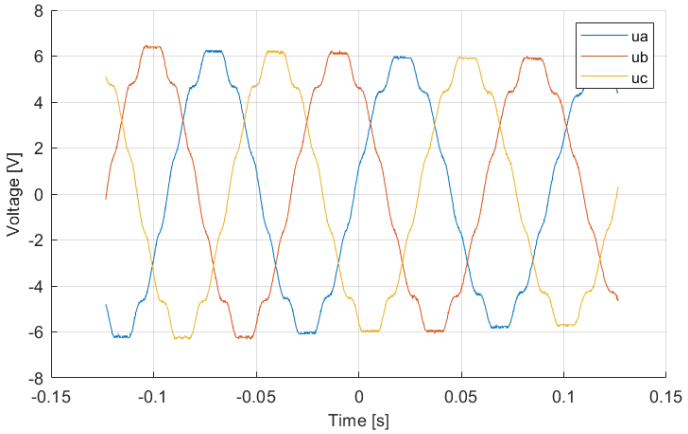

Figure 17: Measured induced voltage between three phases at a rotational speed of 217rpm.

Table 5: Back-EMF peak and rms voltage.

Parameter	Value	Unit
$\hat{u}_{LL}$	6.24	V
$u_{LL,rms}$	4.41	V

Two different methods were tested to calculate the flux linkage from the measured voltage data. The first method assumed a constant rotor speed, which provided a rough estimation since the rotor was manually turned, leading to speed variations. By rearranging equation (2.10) and assuming no currents the flux linkage from the magnets can be calculated using the following expression:

$$\psi_{\mathrm{m}} = \frac{u}{\omega_{\mathrm{e}}} \tag{3.2}$$

The electrical speed was not measured directly but instead determined from one period time of the fundamental frequency component in the measured voltage waveform giving the following expression:

$$\omega_{\mathrm{e}} = \frac{2\pi}{t_{\mathrm{period}}} \approx 69.7\ rad/s \tag{3.3}$$

Under the assumption of constant speed, the flux linkage can be estimated using the expression:

$$\psi_{\mathrm{m,LL,rms}} = \frac{u_{\mathrm{LL,rms}}}{\omega_{\mathrm{e}}} = 0.0631\ Vs \tag{3.4}$$

$$\psi_{\mathrm{m,ph}} = \sqrt{\frac{2}{3}}\,\psi_{\mathrm{LL,rms}} = 0.0515 Vs$$

The second method is based on numerical integration of the measured voltage waveform. By integrating the back electromotive force (EMF), the flux linkage waveform was obtained seen in **Figure 18**.

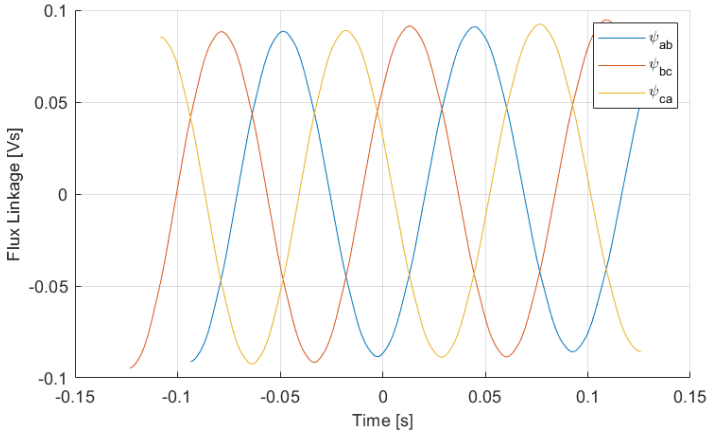

Figure 18: Flux linkage between three phases at a rotational speed of 217 rpm calculated with numerical integration.

The rms value of this flux linkage waveform was then computed to estimate the overall flux linkage. This approach provides a more direct calculation and is less sensitive to speed variations during the test.

$$\psi_{\mathrm{m,LL,rms}} = 0.0632\,Vs \tag{3.5}$$

$$\psi_{\mathrm{m,ph}} = \sqrt{\frac{2}{3}}\,\psi_{\mathrm{LL,rms}} = 0.0516\,Vs$$

The two methods shows a similar result of roughly 52 mVs. Since the mathematical model in Simulink utilizes a power invariant Clarke & Park transformation, the permanent magnet flux must be scaled with $\sqrt{\frac{3}{2}}$ which gives a value of ψ_{m} to 63 mVs.

3.1.4 Measurement of Winding Resistance

The resistance of the electric machine windings was measured using a four-point probe multimeter to ensure accurate low-resistance measurements by minimizing the influence of lead and contact resistances, depicted in **Figure 19**.

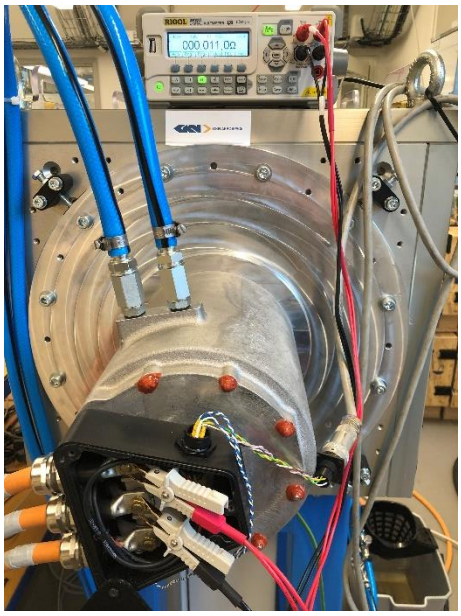

Figure 19: Resistance measurement using a four-point probe multimeter.

The resistance was measured line-to-line across all three phase combinations**:** A to B, B to C, and C to A. The measured resistance in all three cases is measured to 10-11 $\mathrm{m\Omega}$**,** indicating a symmetrical winding resistance across all phases.

Since the machine windings are assumed to be connected in a wye (star) configuration, the phase resistance R_{phase} can be derived from the line-to-line resistance R_{line} using the relationship:

$$R_{\mathrm{line}} = 2R_{\mathrm{phase}} \tag{3.6}$$

Solving for R_{phase}:

$$R_{\mathrm{phase}} = \frac{R_{\mathrm{line}}}{2} = \frac{10\ \mathrm{m\Omega}}{2} = 5\ \mathrm{m\Omega} \tag{3.7}$$

Thus, the calculated phase resistance is 5 mΩ. This resistance value is a key parameter in determining the machine's electrical losses and thermal behavior. This value is incorporated into the simulation model to enhance accuracy and ensure the simulated results closely align with real-world performance.

3.1.5 Measurement of Water Flow and temperature in the Cooling System

To calibrate the cooling parameters of the electric machine to the simulation model, the water flow rate through the cooling system was measured. A timer was set while allowing water to flow through the cooling circuit, the water was then collected in the end of the cooling circuit in a 1-liter container depicted in **Figure 20**.

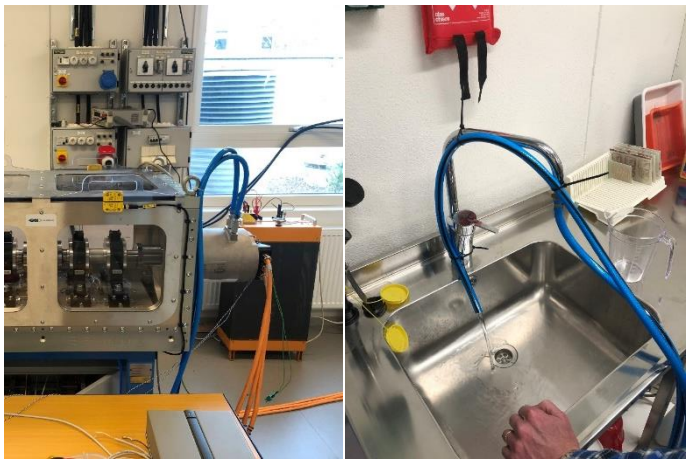

Figure 20: Water flow measurement of the MGU011 cooling system.

The time taken to fill the container was recorded as 17 seconds and from this measurement, the flow rate is calculated as:

$$Flowrate = \frac{1\ liter}{17\ seconds}\ x\ 60\ seconds = 3.53 \approx 4\ \text{liter/min} \tag{3.8}$$

Rounding this to a practical approximation, the measured flow rate is determined to be approximately 4 liters per minute. This flow rate is an important parameter in evaluating the cooling behavior of the electric machine. The obtained value can be used to verify whether the cooling system in the simulated model gives the same thermal result.

The temperature of the cooling water is approximated based on environmental conditions. Since tap water is used in the cooling system, its temperature is not constant and is assumed to be slightly above the local ground temperature. The typical ground temperature in the area is approximately 6 °C, and considering the minor heating effects that occur in water pipes and distribution systems, the tap water temperature is estimated to be around 10 °C.

3.2 Motor-CAD Model Development

In the absence of detailed test data from the MGU011 machine, a reference model is constructed in Motor-CAD. This model is approximated based on the external dimensions, nameplate specifications and measurements of the induced back-EMF. Due to the lack of information regarding the internal geometry, a combination of rough estimations based on a picture of a CAD-model depicting the stator and its windings of the 60kW version MGU012, shown in **Figure 21**, and iterative tuning is employed to achieve a realistic output behavior.

Figure 21: Inside geometry of Magneti Marelli MGU012 (Not verified) [30]

3.2.1 Main dimensions

The first step of the modeling in Motor-CAD consists of inserting the measured external dimensions from section 3.1.1 which creates the limiting cylindrical space available for fitting the cooling sleeve, stator and rotor. The stack length l_{stk} of the machine is estimated based on the available space, taking the end winding height into account. To accommodate a cooling sleeve, a 20 mm thick housing is assumed to be reasonable.

In order to determine the diameter of the rotor, the shear stress equation (2.51) is rearranged giving the expression seen in equation (3.9). Since the MGU011 is supposed to be a relatively high performance machine, the shear stress is assumed to be 35 kN/m^2 and the torque value is taken from the nameplate of the machine at 140Nm which resultes in a rotor diameter of 119mm.

$$D_{\mathrm{r}} = \sqrt{\frac{2T}{\pi\sigma L_{\mathrm{stk}}}} = \sqrt{\frac{2 \cdot 140}{\pi \cdot 35000 \cdot 0.180}} = 0.119\ m \tag{3.9}$$

With the rotor diameter determined and assuming an air gap length of 1 mm, the inner/bore stator diameter is determined resulting in the main dimensions of the machine listed in **Table 6** and the geometry is shown in **Figure 22**.

Table 6: Main dimensions of MGU011 Motor-CAD model.

Dimension	Value	Unit
Machine Outer Diameter (D_m)	210	mm
Machine Length (l_m)	240	mm
Housing Thickness ($w_{housing}$)	20	mm
Stator Outer Diameter (D_{so})	170	mm
Stator Bore Diameter (D_{si})	121	mm
Stack Length (l_{stk})	180	mm
Rotor Diameter (D_r)	119	mm
End Windings Length (l_{EW})	23	mm
Air Gap Length (g)	1	mm

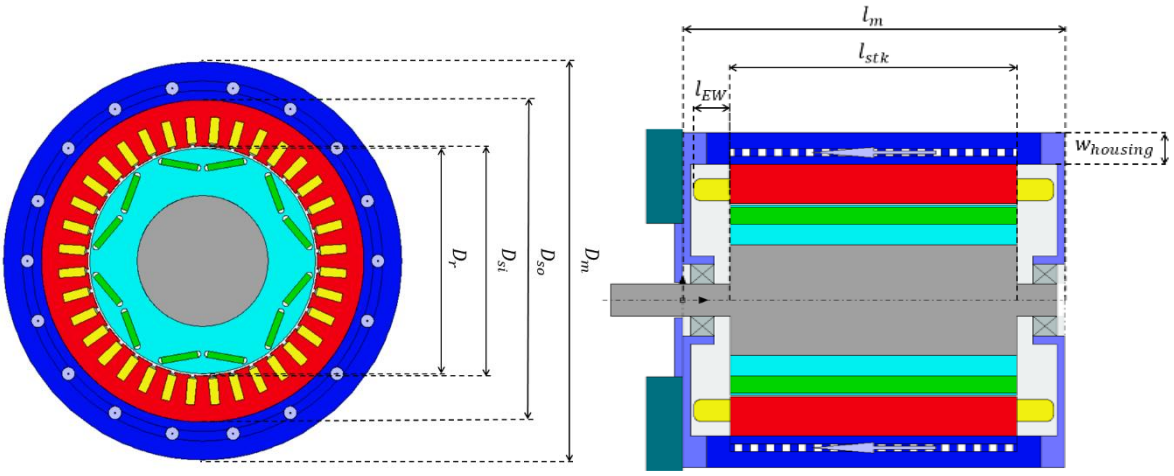

Figure 22: Radial and axial cross section view of the MGU011 Motor-CAD Model.

3.2.2 Winding configuration

With the number of poles determined from the measurements in section 3.1.2, the number of slots can be estimated. The number of slots is not possible to measure, instead it can be based on commonly used pole and slot configurations. For a machine with distributed windings, the number of slots per pole per phase, q, is usually an integer value greater than 1 [11]. In this case, the non-verified CAD-model depicted in **Figure 21** shows a slot number of 36 slots which corresponds to a q equal to 2 which is a reasonable number of slots based on the previous statement and is the chosen slot number for the model.

With the main dimensions and slot number determined, the winding pattern and number of turns is added. By analyzing the CAD-model depicted in **Figure 23**, the number of conductors per slot is 4 with a coil span of 6 slots.

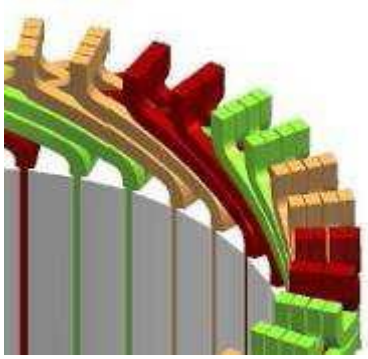

Figure 23: Close up view of the windings of Magneti Marelli MGU012 (Not verified)

The number of turns per phase is determined by comparing the d-axis flux linkage with measurements from the real machine described in Section 3.1.3. With all coils per phase connected in series, resulting in 24 turns per phase, the resulting flux linkage is approximately 100 mVs, twice the measured value. By

instead connecting the windings in two parallel paths as shown in **Figure 24**, the flux linkage is halved, bringing it closer to the measured value of 52 mVs.

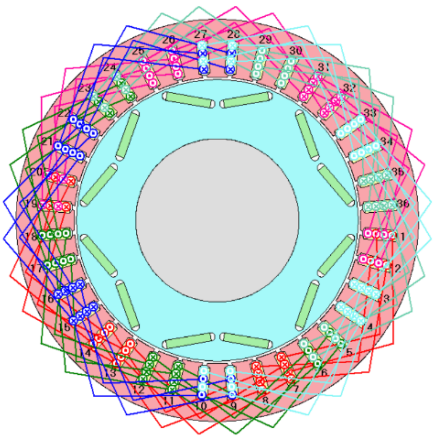

Figure 24: Winding pattern of the Motor-CAD model.

3.2.3 Conductor sizing

With the winding configuration determined, the sizing of the conductors can be determined. Since the winding is assumed to be a hairpin winding, the conductors has a rectangular shape which also is seen in **Figure 23**. As explained in equation (2.24), the resistance is dependent on the length, conductivity and cross sectional area of the conductor. Since the stack length, end windings and coil span is determined, the length of the conductors is automatically calculated by Motor-CAD. With the assumption that the conductors are made of copper with its corresponding conductivity, the sizing of the conductor consists of determine the width and depth. From the resistance measurements in section 3.1.4, the resistance is measured to $5\mathrm{m}\Omega$ which is used as the reference value to get the correct cross sectional area. The resulting dimensions are listed in **Table 7** and the geometry depicted in **Figure 25**.

Table 7: Conductor dimensions.

Dimension	Value	Unit
Conductor Width (w_{cu})	3.8	mm
Conductor Height (h_{cu})	3	mm
Insulation Thickness (ins)	0.1	mm
Liner Thickness ($liner$)	0.3	mm

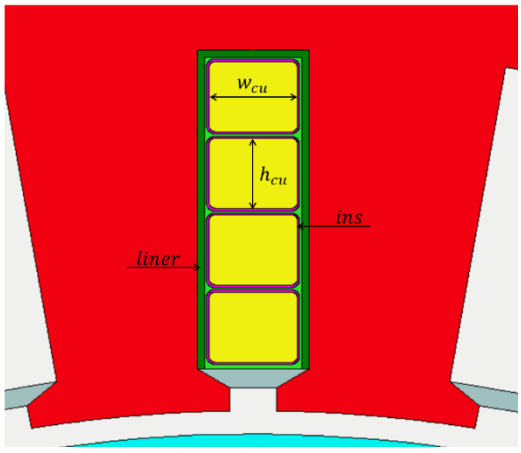

Figure 25: Conductor dimensions.

3.2.4 Magnet sizing

The permanent magnet flux linkage of 52 mVs is not only dependent on the winding configuration, but also on the permanent magnet sizing and positioning. By iterating the width, thickness and v-shape angle, the flux linkage is calibrated to match the measured value. The bridge between the rotor circumference and the magnet pocket w_{bridge} is kept at Motor-CAD default thickness and likewise for the rib between to magnet pockets w_{post}. The resulting dimensions are listed in **Table 8** and the geometry is depicted in **Figure 26**.

Table 8: Magnet dimensions.

Dimension	Value	Unit
Magnet Width (w_m)	19.1	mm
Magnet Height (h_m)	3.5	mm
(V_{angle})	160	deg
(w_{bridge})	1	mm
(w_{post})	2	mm

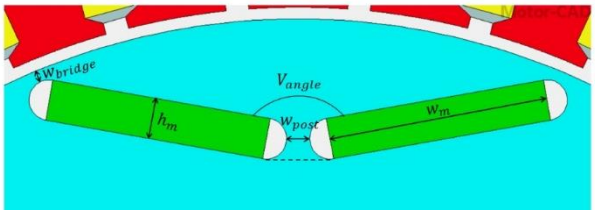

Figure 26: Magnet dimensions.

3.2.5 Cooling sleeve sizing

Due to the lack of detailed information regarding the cooling sleeve geometry in the MGU011, a conventional spiral water jacket configuration is assumed as the basis for the model. The dimensions of the cooling channel are estimated and summarized in **Table 9** and shown in **Figure 27**.

Table 9: Water jacket dimensions.

Dimension	Value	Unit
WJ Channel Width	5	mm
WJ Channel Height	5	mm
WJ Channel Spacing	5	mm
WJ Lamination	5	mm

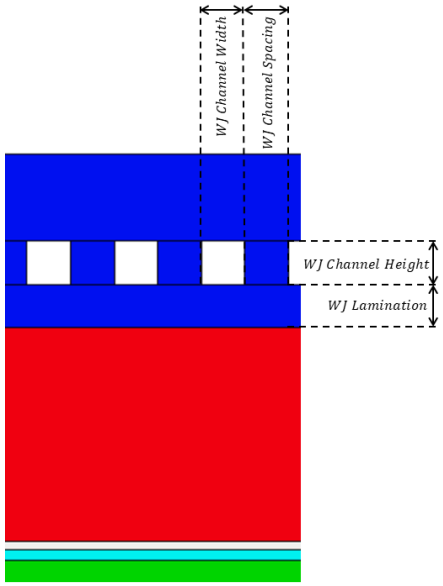

Figure 27: Water jacket dimensions.

3.2.6 Efficiency Map Generation

In order to get an understanding of the overall performance of the machine an efficiency map of the different torque speed combinations is crucial. To create an efficiency map in Motor-CAD, a maximum current and the DC voltage is required. The DC-voltage is given from the system requirements at 540 V DC while the maximum current is not given. However, the maximum current experimentally tested on the MGU011 machine corresponds to a current combination of 500 A along the *q*-axis and -300 A along the *d*-axis, resulting in a total current magnitude of 583 A. Consequently, this value is set as the maximum current limit in Motor-CAD. With the maximum speed defined according to the system requirements, the resulting efficiency map generated by Motor-CAD is presented in **Figure 28**.

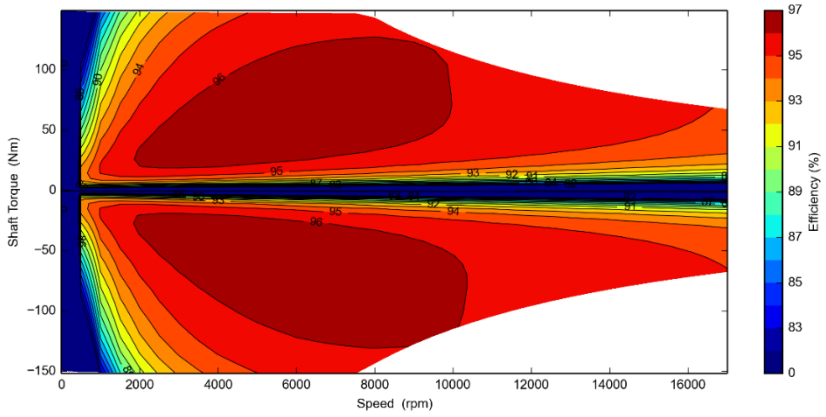

Figure 28: Efficiency map of MGU011 Motor-CAD model.

3.3 Motor-CAD Thermal Model

To achieve a representation of the thermal behavior of the electric machine, the thermal model developed in Motor-CAD is used. Motor-CAD offers a hybrid modeling approach that combines a detailed lumped parameter thermal network with losses calculated through finite element analysis providing enhanced prediction of temperature distributions within the machine components. The lumped parameter network in Motor-CAD, depicted in **Figure 29**, provides a detailed representation of the thermal circuit including ambient and magnet temperature, which are essential to get an accurate view of the thermal performance.

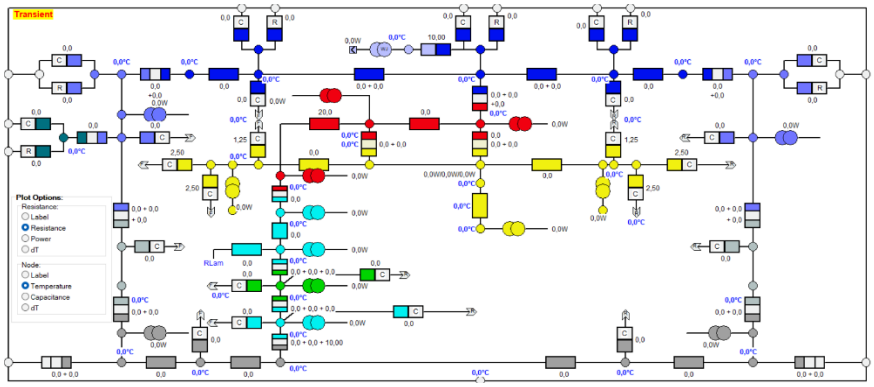

Figure 29. Lumped parameter thermal network in Motor-CAD.

Motor-CAD enables a variety of cooling topologies where coolant flow and fluid properties can be adjusted to evaluate the thermal performance. With Motor-CAD, the sensitivity analysis of different cooling topologies and geometries simplifies, since the thermal model automatically updates as the design changes.

3.4 Simulink Simulation Model

In this section the full Simulink simulation model, seen in **Figure 30**, is explained.

Controlling the power electronics is not just about the linear modulation zone where a common space vector control scheme is implemented. It also concerns over-modulation, six-step operation and the transition between linear and six-step modulation. Section 3.4.1 explains the look-up tables to set the currents and how to simulate six-step for lower speeds. The induced voltage in the simulation model does not exceeding the voltage limitation of $\frac{U_{\mathrm{dc}}}{2}$, until speeds of up to 50000 rpm, which results in the model not entering six-step until it reaches very high speeds. The “Compensation of decreasing Udc” area in **Figure 31** compensates for the high rpm requirements to enter over-modulation, so that the machine enters in to over-modulation at lower rpm. The current controller block that sets the voltage references from the error between the reference currents and the actual currents is introduced in section 3.4.2 followed by an in depth explanation of how they work since one of the challenging aspects is combined field weakening control and modulation transition.

Section 3.4.3 describes the modulator and how symmetric modulation is implemented followed by an explanation of the implementation of the converter block. The simulation model of the PMSM is introduced in Section 3.4.6 and is developed based on the mathematical model in Section 2.1.1. Additionally, the thermal model of the PMSM is explained in Section 3.4.7 where an approximation of the thermal behavior is developed.

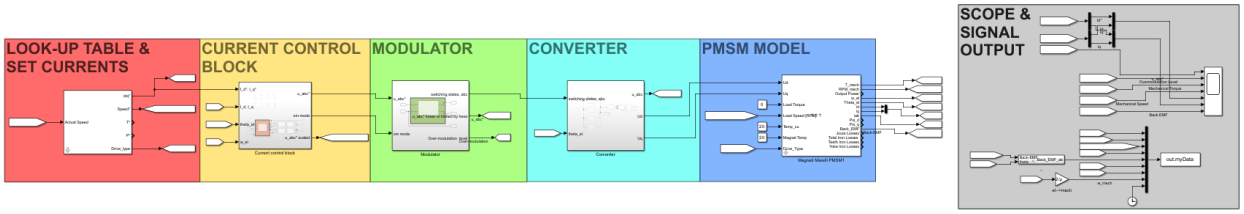

Figure 30: Full Simulink simulation model.

3.4.1 Current Reference Block

In order to control the torque of the machine, the reference currents corresponding to the desired torque is set to the power electronics model through the current reference model illustrated in **Figure 31**.

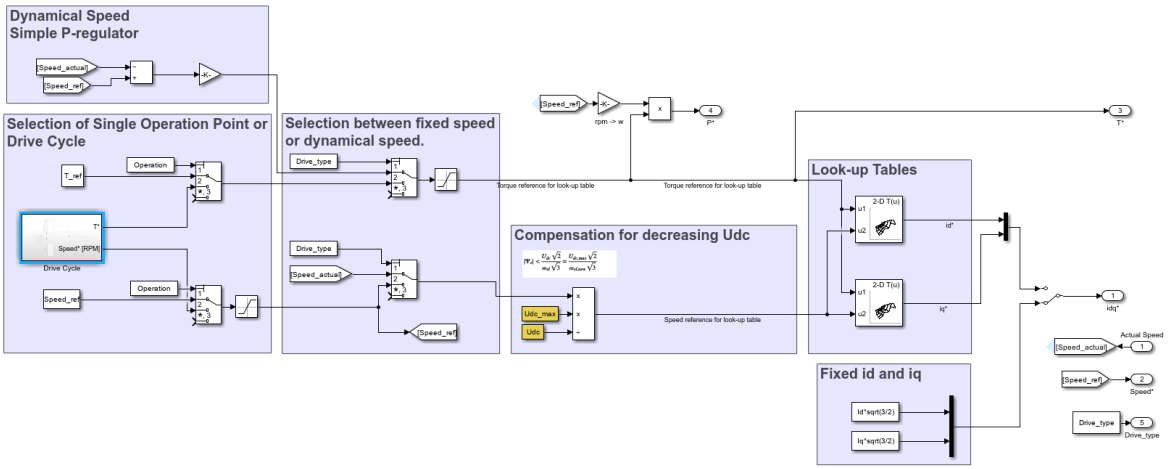

Figure 31: Simulink current reference model.

3.4.1.1 Torque & Speed Look-Up Tables

By providing a torque reference and the machine's rotational speed as inputs to two look-up tables, the corresponding current references i_d^* and i_q^* are obtained and subsequently used in the current control block explained in Section 3.4.2. These look-up tables contain the current combinations with lowest total losses for each torque and speed operating point. The data in these tables can be acquired experimentally by operating the machine at various fixed speeds while sweeping the current values to measure the resulting torque and losses.

In the absence of experimental data, the efficiency map generated from the Motor-CAD model is used as an alternative source where the currents for each operating point can be extracted from the Motor-CAD software. By then interpolating the currents for each operating point a torque speed map is generated for i_d and i_q illustrated in **Figure 32** and **Figure 33**.

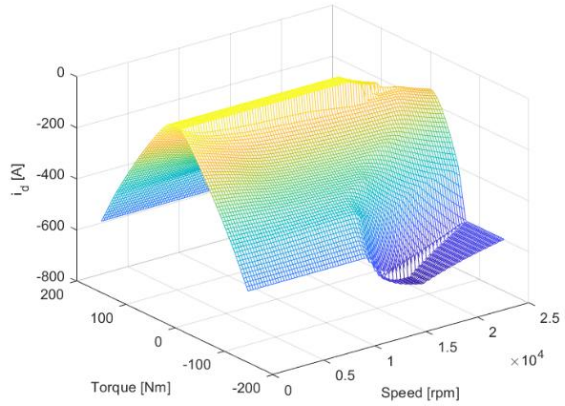

Figure 32: Look-up table for i_d with torque and speed as inputs.

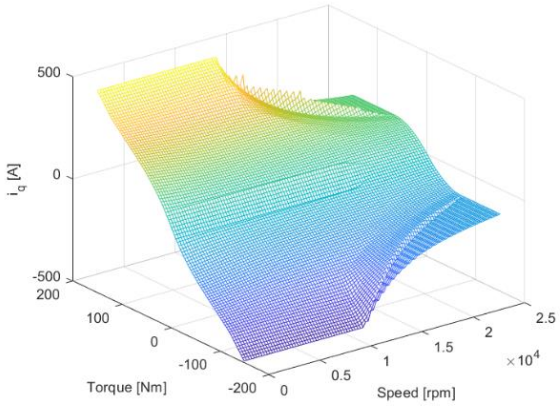

Figure 33: Look-up table for i_q with torque and speed as inputs.

The implementation of overmodulation and six-step modulation in the control algorithm enables a higher achievable phase voltage compared to linear modulation. However, since Motor-CAD only supports linear modulation, the generated look-up tables are limited by a maximum phase voltage of $\frac{U_{\mathrm{dc}}}{\sqrt{2}}$. In contrast, six-step modulation allows the voltage to reach $\frac{U_{\mathrm{dc}}\sqrt{2}}{\sqrt{3}}$, approximately 15 % higher than with linear modulation. To ensure that the current references in the look-up tables remain valid even when the actual system operates beyond the linear modulation range, the look-up tables are generated using a DC-link voltage that is 15 % greater system requirements of 540 V. This approach compensates for Motor-CAD's linear modulation constraint, allowing the resulting tables to better reflect the extended voltage capabilities enabled by the control strategy.

The current reference model includes multiple options for defining the reference currents. It features both a dynamic speed option and a fixed speed option, which can be utilized either for a single operating point or across a drive cycle with four operating points. These options are set in the Simulink block mask.

3.4.1.2 Dynamic speed

The dynamic speed option activates the speed control of the PMSM model which includes the motor dynamics explained in Section 2.1.1.3. As the inertia from the load is included, the dynamical behavior of the machine can be evaluated. This is useful when running the machine as a motor, since the time it takes to reach a certain speed can be evaluated.

The torque reference is calculated using a simple proportional (P) controller, where the speed error serves as the control signal. By specifying a desired reference speed, the regulator computes the difference between the reference speed and the actual machine speed, multiplies this error by a proportional gain constant, and outputs the result as the torque reference and can be expressed as:

$$T^* = k_\mathrm{p} \cdot (Speed^* - Speed_\mathrm{actual}) \tag{3.10}$$

As the machine has a maximum torque the control signal has a limitation block which limits the torque reference to the peak torque of the machine.

3.4.1.3 Fixed speed

Since the electric machine primarily operates as a generator connected to the turbine output shaft, its rotational speed is dictated by the turbine's output shaft speed. With the fixed speed option activated, a fixed speed can be set to the PMSM shaft which neglects the motor dynamics. This approach is particularly useful for simulating machine operation during testing with a braking machine, where the shaft speed is externally controlled and maintained at a constant value.

3.4.1.4 Manual current references

For testing the different current combinations, a manual switch is implemented, connected to two constant blocks where fixed current references can manually be specified. This option enables a comparison between the output torque for the specified currents of the electric machine model and experimental measurements from the physical machine.

3.4.1.5 DC-link voltage limitation block

With six-step modulation, the line to line voltage is limited to $\frac{U_\mathrm{dc}\sqrt{2}}{\sqrt{3}}$. This induced voltage limitation can be expressed as:

$$\omega_\mathrm{el}|\psi_\mathrm{s}| < \frac{U_\mathrm{dc}\sqrt{2}}{\sqrt{3}} \tag{3.11}$$

As the rotational speed increases the induced voltage increases until it reaches the voltage limitation. To keep increasing the speed the look-up tables must output current references that field weakens the flux. By reformulating Equation (3.12) the flux limitation can be expressed as:

$$|\psi_\mathrm{s}| < \frac{U_\mathrm{dc}\sqrt{2}}{\omega_\mathrm{el}\sqrt{3}} \tag{3.12}$$

Since the look-up tables are generated based on a fixed DC-link voltage, a decrease in the DC-link voltage is not accounted for. As a result, the reference current does not adapt to the reduced voltage limit under these conditions. To incorporate this compensation directly into the look-up tables, an additional dimension representing the DC-link voltage would be required. However, this approach would necessitate generating a separate look-up table for each DC-link voltage level. As an alternative, a practical workaround is implemented. Instead of reducing the DC-link voltage, the reference speed is artificially increased. This adjustment can be computed using the following expression:

$$\frac{U_\mathrm{dc}\sqrt{2}}{\omega_\mathrm{el}\sqrt{3}} = \frac{U_\mathrm{dc,max}\sqrt{2}}{\omega_\mathrm{el,new}\sqrt{3}} \rightarrow \omega_\mathrm{el,new} = \omega_\mathrm{el} \cdot \frac{U_\mathrm{dc,max}}{U_\mathrm{dc}} \tag{3.13}$$

Here, $U_\mathrm{dc,max}$ represents the fixed DC-link voltage used during the generation of the look-up tables in Motor-CAD, and $\omega_\mathrm{el,new}$ denotes the modified electrical speed. As the actual DC-link voltage decreases,

the reference speed input to the look-up tables is artificially increased. This adjustment makes the look-up tables to increase the field weakening effect, thereby reducing the induced voltage and compensating for the lower DC-link voltage.

3.4.2 Current Control Block

The current control block contains several different sections that together gives the model the control necessary to not only work in linear modulation. They also allow it to control the current in over-modulation. The different areas of **Figure 30** is covered in the following sub-sections, from the inputs, all the way to the outputs of the current control block.

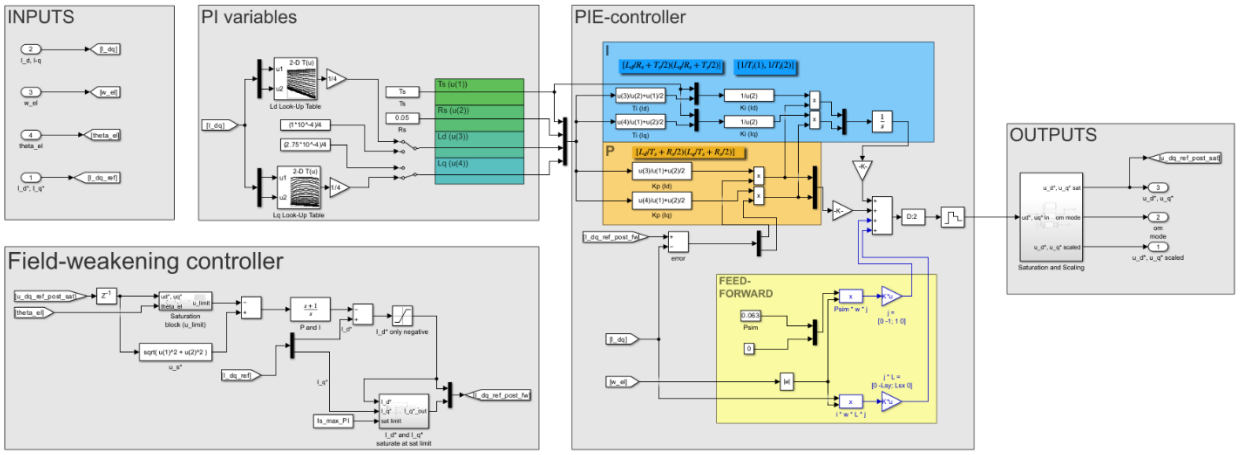

Figure 34: Current control block.

3.4.2.1 Inputs and Outputs

The input and output blocks can be seen in **Figure 35** and **Figure 36** respectively. Before the phase reference voltages are sent to the modulator in the outputs block, the pass through a saturation block. This block limits the reference voltage vector in the alpha- beta-plane to always stay inside the hexagon. It does this by making sure that the amplitude of the voltage reference never exceeds the maximum voltage it does this by calculating the maximum voltage for a specific angle with Equation (2.64) and then scaling the voltage equally in both d- and q-axis according to the following equation:

$$U_{ref,scaled} = \frac{U_{ref}}{U_{max}} \cdot U_{ref} \tag{3.14}$$

It is this block that makes the transition from linear modulation to six-step modulation. The “Saturation and Scaling” block also outputs a signal that represents the current over-modulation mode (om mode). In om mode 1, the controller operates in linear modulation; in om mode 2, it operates in the transition region between linear and six-step modulation; and in om mode 3, it uses six-step operation.

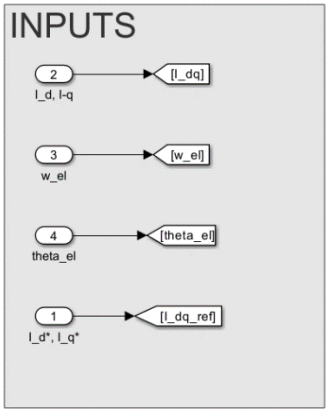

Figure 35: Inputs to the current control block.

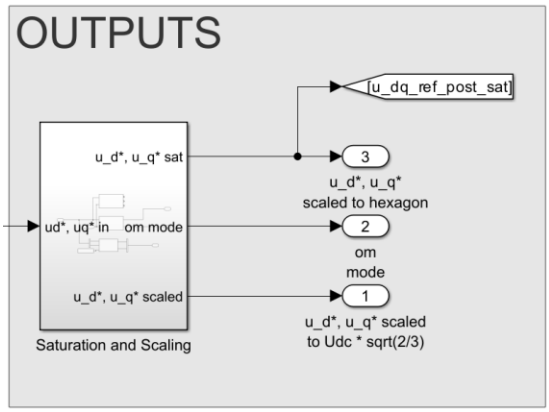

Figure 36: Outputs from the current control block.

3.4.2.2 Field-weakening controller

The reference signals coming from the input have been decided with a look-up table. This look-up table works great if the model is running in linear modulation but is no longer applicable if the machine goes into six-step operation. This is where the Field-weakening controller steps in. The role of the flux-weakening controller is to determine the current references satisfying voltage and current constraints imposed by over-modulation. The controller is taken from an article on six-step operation [31] and can be seen in detail in **Figure 37**. When asked to run at a speed and torque that it does not have enough current to handle, the controller prioritizes the *d*-axis-current to have the same amount of field-weakening even though the this means that the *q*-axis current might not be enough to reach the torque level that is asked of it. It does this by restricting the *q*-axis current so that the total current never exceeds the maximum current magnitude.

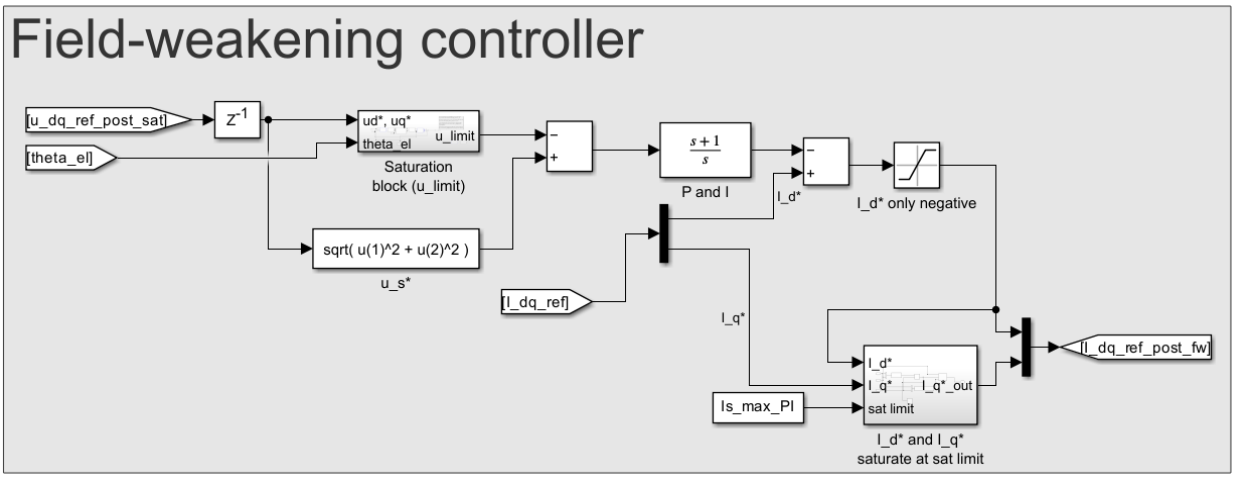

Figure 37: Field-weakening controller [31].

3.4.2.3 Current-controller

After the field weakening controller, the reference currents are sent to the Current-controller, seen in **Figure 38**, which has a Proportional part (P), and Integrating part (I) and a feed-forward part (E) that feed-forwards the back-EMF.

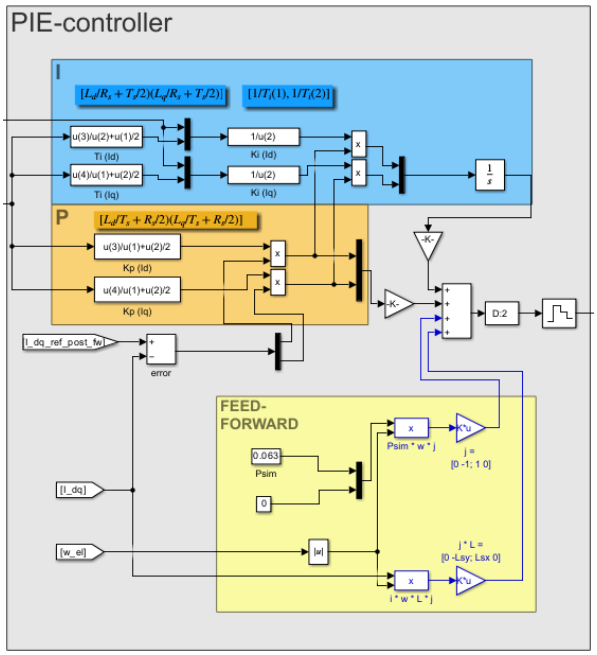

Figure 38: PIE Current-controller.

Proportional part

The proportional part of the PIE regulator calculates K_p, for the *d*- and *q*-current, by using the following equations:

$$K_{\mathrm{p}(I_d)} = \frac{L_d}{T_\mathrm{s}} + \frac{R_\mathrm{s}}{2} \tag{3.15}$$

$$K_{\mathrm{p}(I_q)} = \frac{L_q}{T_\mathrm{s}} + \frac{R_\mathrm{s}}{2} \tag{3.16}$$

Where L_d and L_q are the *d* and *q* inductances respectively, T_s is the sampling frequency and R_s is the stator winding resistance for one phase. L_d and L_q is implemented in two ways, either the values are extracted from look-up tables or the are set to a constant value which in this case was set to the average values for each look-up table.

Integral part

The integral part also calculates the relevant constants, K_i and T_i, for both I_d and I_q. These are calculated by the following four equations:

$$K_{\mathrm{i}(I_d)} = \frac{1}{T_{\mathrm{i}(I_d)}} \tag{3.17}$$

$$K_{\mathrm{i}(I_q)} = \frac{1}{T_{\mathrm{i}(I_q)}} \tag{3.18}$$

$$T_{\mathrm{i}(I_d)} = \frac{L_d}{R_\mathrm{s}} + \frac{T_\mathrm{s}}{2} \tag{3.19}$$

$$T_{\mathrm{i}(I_q)} = \frac{L_q}{R_\mathrm{s}} + \frac{T_\mathrm{s}}{2} \tag{3.20}$$

Feed-forward part

The feed-forward part, feed-forwards the calculated back-EMF. The back-EMF calculated consists of two parts and originates from the rotor's permanent-magnet inductance equation (3.21) and the stator winding's inductance equation (3.22).

$$j \cdot \omega_{\mathrm{el}} \cdot L \cdot \vec{\imath} \tag{3.21}$$

$$j \cdot \omega_{\mathrm{el}} \cdot \Psi_{\mathrm{m}} \tag{3.22}$$

Where ω_{el} is the electrical angular frequency, L is the inductance, $\vec{\imath}$ is the current vector and Ψ_{m} is the permanent-magnet flux linkage and was calculated to be 63 mVs as can be seen in Section 3.1.3. 63 mVs was calculated by Equation (3.2).

3.4.2.4 PI variables

When K_{p} and K_{i} are calculated, they use the sampling time (T_{s}), winding resistance (R_{s}) and the *d*- and *q*-axis inductances (L_d) and (L_q) respectively. T_{s} and R_{s} are constant values but L_d and L_q vary with the current. To get accurate inductance values they are extracted from look-up tables as seen in **Figure 39**.

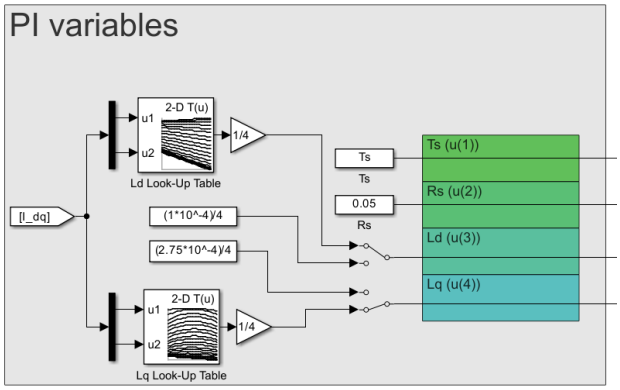

Figure 39: PI variables.

Even the look-up tables were implemented to get better values for K_{p} and K_{i}, for unknown reasons the reference voltage had a lower ripple at lower inductances, specifically with inductances with a gain of ¼. This was tested empirically by simulating different gains and why a gain of ¼ performed the best is unclear but is not investigated within this work. However, an important observation is that the theoretical values should be reduced, at least for practical experimentation. With a gain of ¼, the reference voltages had less ripple and the controller therefore performed better.

3.4.3 Modulator

Before the signal is sent into the modulator it passes through a switch block. As seen in **Figure 40** the block considers the current over-modulation mode. If “om mode” is 3 it means that it is running in six-step operation and the modulator should be sent square waves instead **Figure 41**. **Figure 42** shows a graph of u_abc*, the output from the six-step block, the output from the switch block and the over-modulation level. The modulator itself is in **Figure 43** and can switch between sinusoidal and symmetric modulation, it is a modification of the modulation block from a Simulink model from Mats Alaküla’s course in power electronics [32].

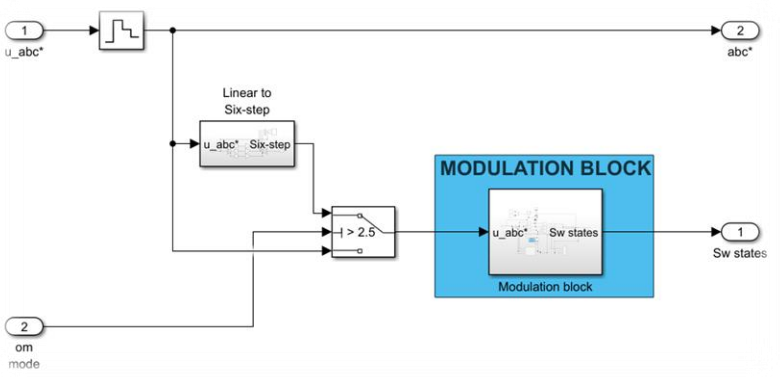

Figure 40: Switch from linear to six-step modulation.

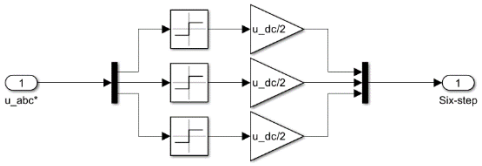

Figure 41: Linear to six-step.

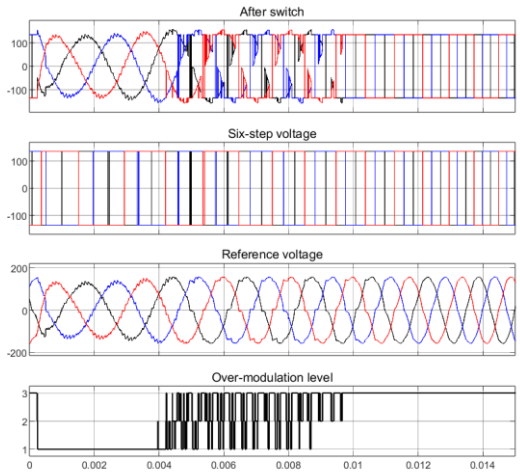

Figure 42: The resulting output to the modulator, the six-step blocks output, the voltage reference before the switch and the Over-modulation level.

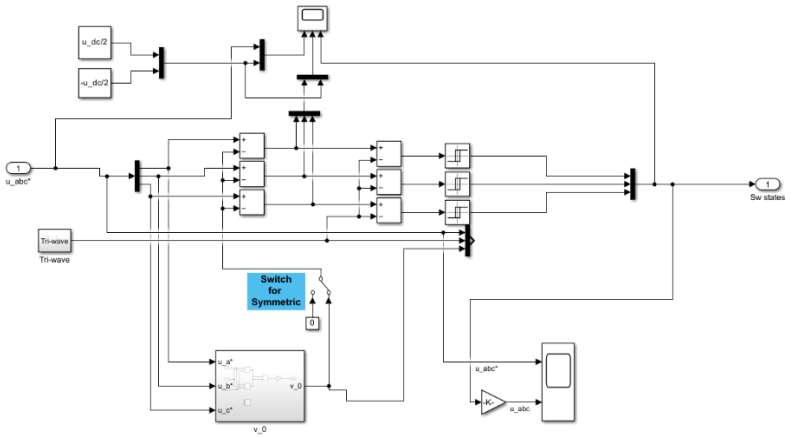

Figure 43: Modulator block with either sinusoidal or symmetric modulation [32].

3.4.4 Converter

In order to compare different types of transistors and their performance, several converter models are implemented, with ideal switches, multiple converters were built in the simulation model.

In Simulink, there are blocks that represents the entire 3-phase converter. These blocks are easy to implement and fast to run, but does not allow for changes of the characteristics of the individual transistors. Since one of the objectives is to compare the use of different transistors with different characteristics, these blocks are not an option for the model. Instead, discrete components are used from the Simscape-Electrical library. This make it possible to characterize the transistors after the specifications from the datasheet. As can be seen in **Figure 44**, the different types of transistors have different delay times. The fastest switching transistor is the SiC FF6, but even if the rising and falling time is fast there is still a delay until the switching starts compared to the ideal switch.

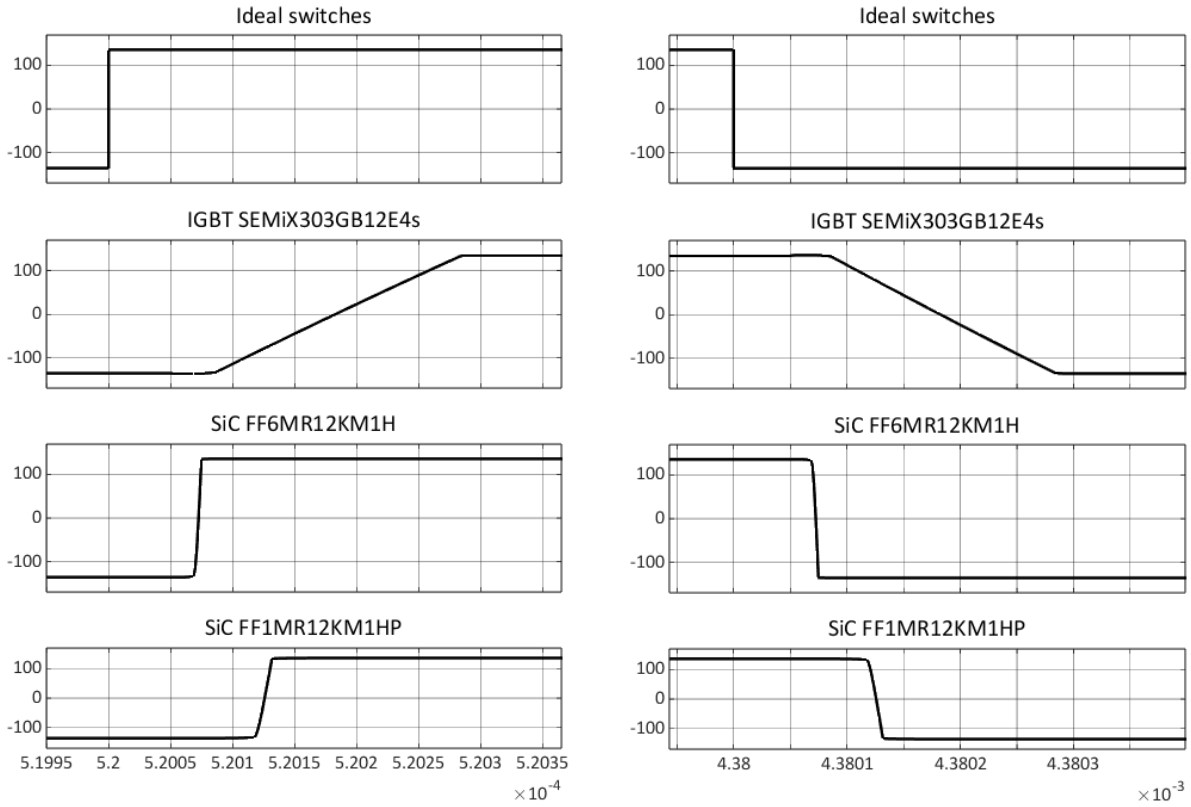

Figure 44: Rise- and fall times of different switches in the converter block in the full electrical Simulink simulation.

Altogether, four different converters are included in the simulation model and can easily be switched between. The first of the four types of switches/transistors being used is an ideal logical switch with no delay or rise/fall time (**Figure 45**). The second converter uses IGBTs of the model SEMiX303GB12E4s [33]. The reason for using this exact transistors is that they are used in the test-rig that was used to verify the simulation model (**Figure 46**). The third and fourth converters, uses SiC transistors, that in theory should have faster rise and fall times, as well as lower losses. The converters uses different types of SiC, FF6MR12KM1H [34] and FF1MR12KM1HP [35] for the third (**Figure 47**) and fourth (**Figure 48**) respectively. The difference between these two is mainly that FF1MR12KM1HP can handle higher currents but in turn has slower rise and fall times which increases switching losses.

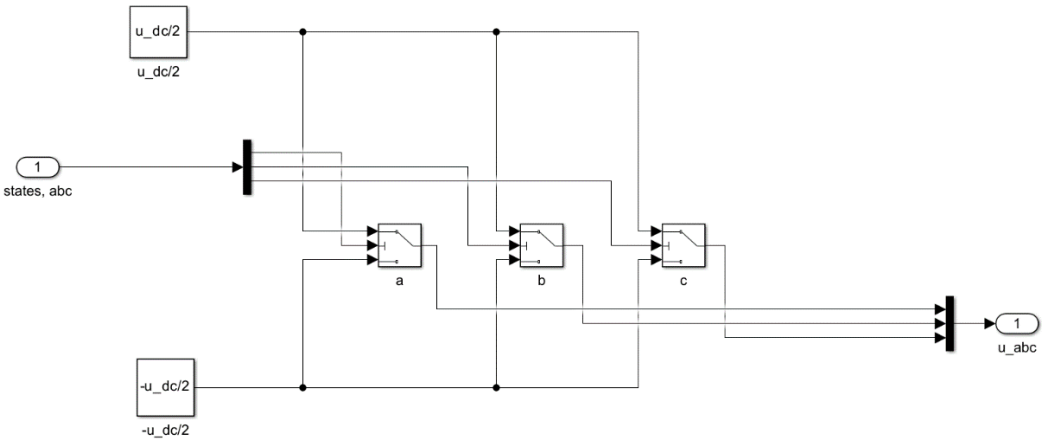

Figure 45: Converter with Ideal switches.

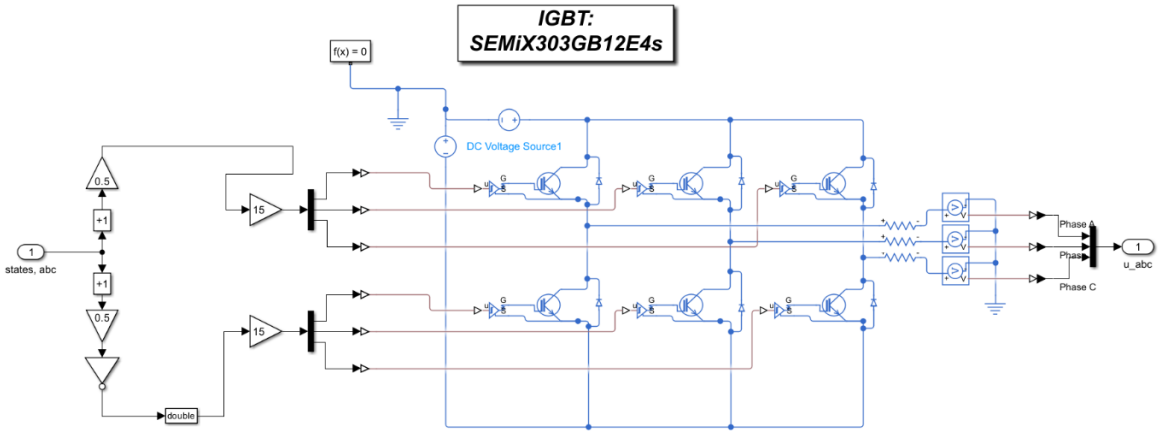

Figure 46: Converter with IGBTs.

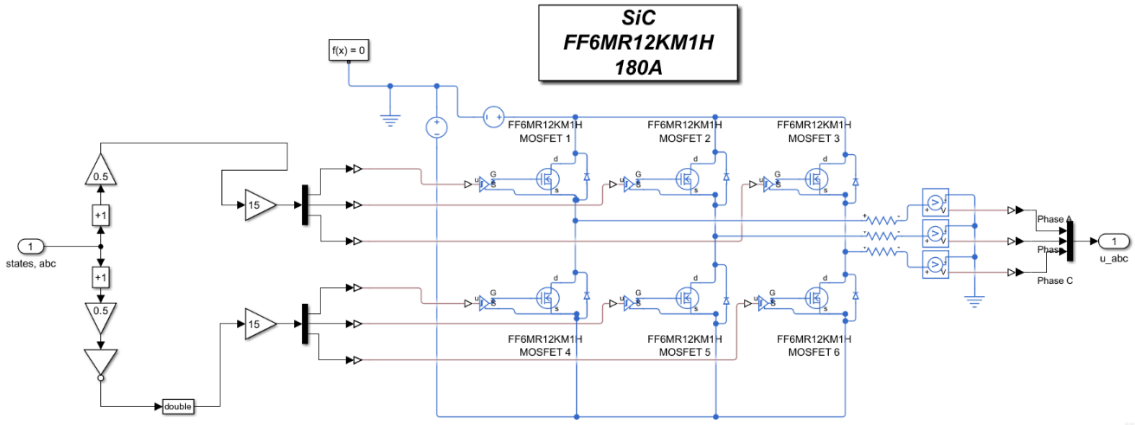

Figure 47: Converter with SiC, FF6.

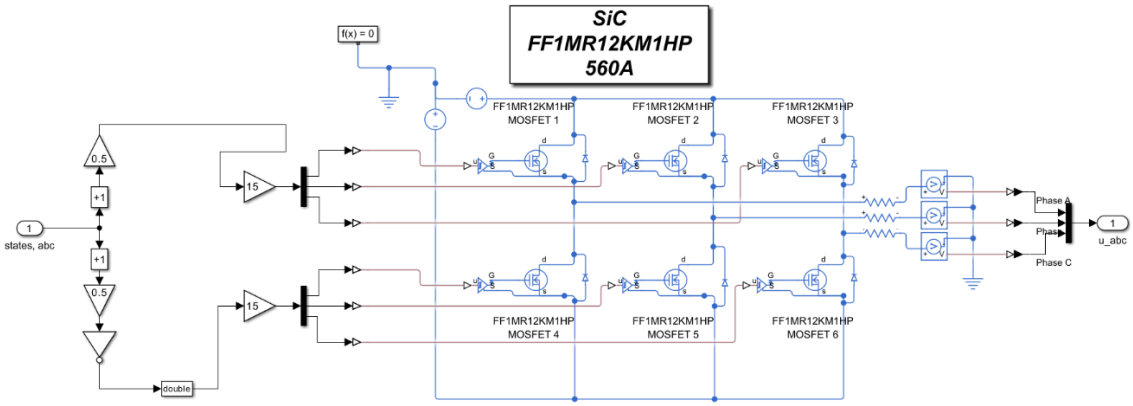

Figure 48: Converter with SiC, FF1.

3.4.5 Power Electronics Thermal Modeling

Due to the slow processing time of the full simulation model the thermal circuit model is simulated in a different file. In the power electronics simulation model, no simulation runs for longer than 1 second. This is due to the long time it takes for the power electrical simulation model to run in Simulink. In order for a component in the separate thermal simulation to reach its steady-state temperature the simulation time needs to be a lot longer than that. To get around this issue the values (switching states, voltages, currents, etc.) from the simulation done in the power electronics model are saved as vectors in Matlab. A script is then run that splits all the vectors in two halves, the first and second half of the vectors. The first half of the values is run in the beginning, the second half of the values, on a loop, for the remainder of the thermal simulation time. This is done in order to represent the switching patterns as accurately as possible in both the beginning and as time increases.

Figure 49 shows the entire thermal circuit Simulink document. What the different areas do and how they relate to each other is explained later in this chapter. At a high level, it works by having the saved data from a previous power electronics simulation imported in the “Inputs signals” area which is then distributed to the “Switching losses” and “Conduction losses” areas. These two areas also get data from the relevant transistor (which is chosen in the “Choose transistor” area) and uses all of this to calculate the total losses. These losses are sent to the “Heat dissipation” area that calculates different local temperatures with a thermal circuit using first degree thermal models.

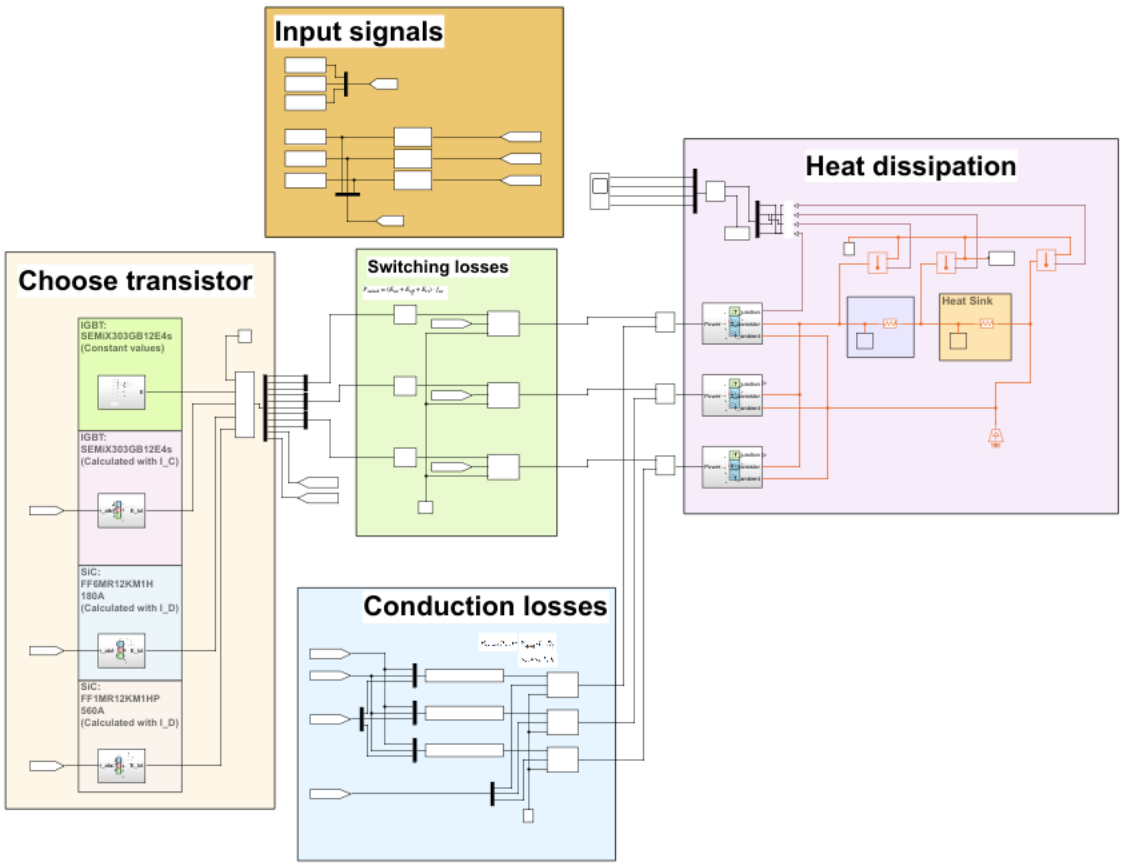

Figure 49: The full Simulink simulation for the thermal calculation.

3.4.5.1 Input signals

The "Input signals" area, which can be seen in **Figure 50** imports the voltage and current of phase a, b and c. The vectors, with the data describing the voltage and current, have been lengthened by repeating the second half of the vector to make sure that the thermal simulation can run for as long as it needs. The blocks between the voltage imports, u_a_simulink, u_b_simulink and u_c_simulink, and the goto blocks called change_a, change_b and change_c, are detect-change blocks. Detect-change blocks outputs a 1 for a sampling period when its input has changed and outputs a 0 if its inputs remains the same. This is used in the "Switching losses" area to decide when the transistors on a given phase are switching. The voltage from the converter changes from $+\frac{U_{\mathrm{dc}}}{2}$ to $-\frac{U_{\mathrm{dc}}}{2}$ when a certain phase's transistors are switching which makes the changes in voltages great indicators for the occurrence of switching losses.

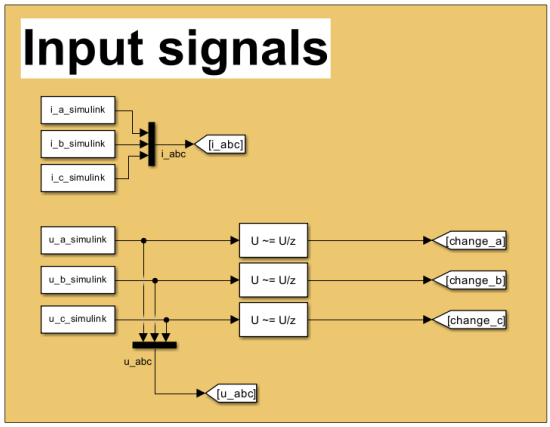

Figure 50: Input signals for the thermal calculation.

3.4.5.2 Choose transistor

In the "Choose transistor" area a choice between three different transistors can be made. The reason that there are four blocks to choose between, as can be seen in **Figure 51**, is that the first transistor can be used both with constant values taken from the datasheet or with more exact values interpolated from the graphs of the datasheet and calculated with the instantaneous current.

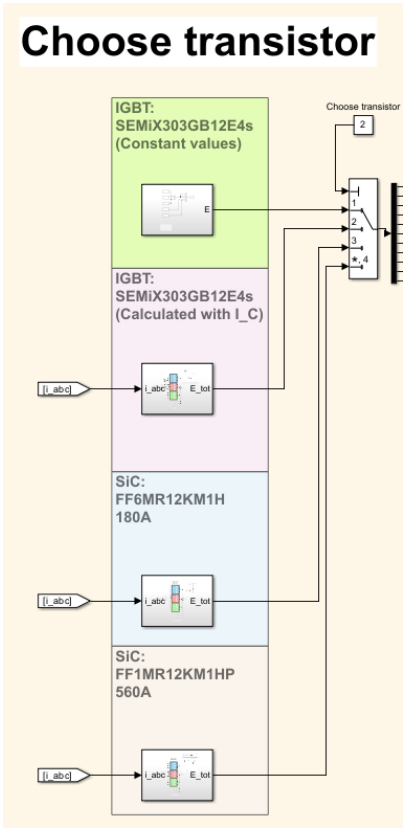

Figure 51: Transistors choice for the calculation.

Figure 52 shows one of the transistor parameter calculation blocks. It uses a current to calculate E_{on}, E_{off} and E_{rr} (which only exists for IGBTs) for each phase, since they are current dependent. The block also holds values for the resistance (R_{CE} for IGBTs or R_{DS} for SiC) and forward voltage at zero current V_{f0} (which only exists for IGBTs). The "E_on calc" function blocks calculates the energy loss by linearizing the graph from that components formula sheet (the graph can be seen in the top right of **Figure 52**).

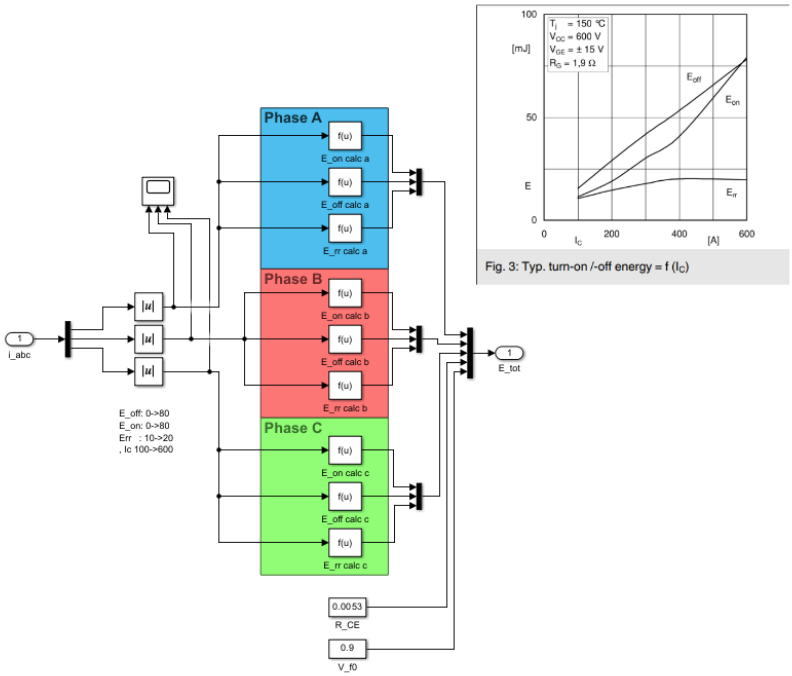

Figure 52: Transistor parameters calculation block.

3.4.5.3 Switching losses

In the "Switching losses" area, the output is a pulsed signal that represents the power losses. As can be seen in **Figure 53**, it does this by first creating a signal representing the power lost if the transistors were to switch once every sampling period (T_{s}). This power is calculated from Equation (2.55) that calculatesE_{tot}. Multiplying E_{tot} with the switching frequency (f_{sw}) results in the power if the transistors were switching ones every T_{s}.

$$P_{\mathrm{switch}} = (E_{\mathrm{on}} + E_{\mathrm{off}} + E_{\mathrm{rr}}) \cdot f_{\mathrm{sw}} = E_{\mathrm{tot}} \cdot f_{\mathrm{sw}} \tag{3.23}$$

This power is then pulsed by letting the power through of phase a,b or c if the corresponding change variable (i.e. change_a, change_b or change_c) is equal to 1, otherwise the output is set to 0.

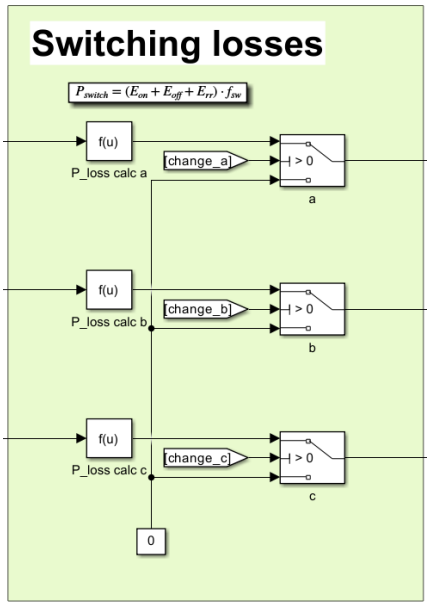

Figure 53: Switching losses calculation.

3.4.5.4 Conduction losses

Conduction losses (P_{loss}) are calculated with Equation (2.56) for each phase and are sent on to the "Heat dissipation" area only when that specific phase is conducting current. V_{f0} and R_{s} are extracted from the relevant transistors block. SiC transistors for example doesn't have a V_{f0}, which means that if one of those blocks is chosen V_{f0} is equal to zero. To make sure that losses only are sent to the "Heat dissipation" area when one transistor in each transistor pair actually is conducting, (so that there is no need to calculate losses during the dead-time when no transistor is conducting) the condition that lets P_{loss} through is that the magnitude of the current in a given phase should be bigger than zero. Otherwise the output becomes zero.

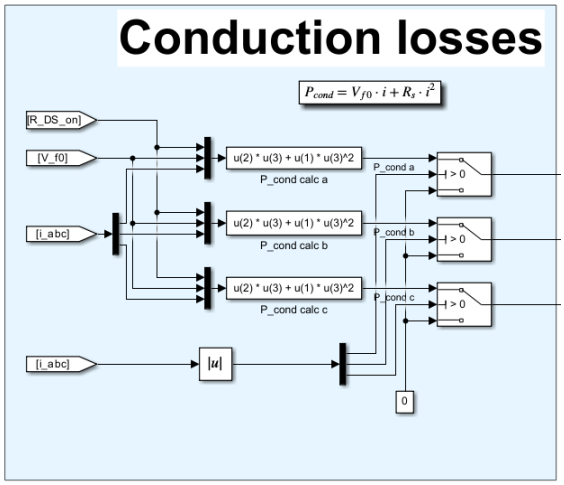

Figure 54: Conduction losses.

3.4.5.5 Heat dissipation

Calculation of the steady-state temperature of the converter and its components is implemented in **Figure 55** in order to determine if the components are able to handle the heat produced. A first order model of each transistor pair, the module or casing, the thermal grease in between the converter and the heat sink and of the heat sink itself, is implemented, as can be seen in the **Figure 56**. This is also where the transistor type for the thermal calculations can be chosen by connecting the relevant transistor pair to the input and output.

The reason for using a first order RC-circuit to represent the heat sink and thermal grease is that the cooling capabilities of both in general, and of the heat sink in particular, is dependent on a lot of different factors. Therefore it is better to give the possibility to the modeler to have the investigation and simulation result in requirements on the thermal resistance of the heat sink, than to present different types of cooling. These results can then be used when looking at heat transfer options to study the cooling requirements and possible solutions. T_ambient is set to 20 ℃ and 60 ℃ to simulate different temperatures on the cooling fluid. The heat dissipation block outputs temperatures from four different locations in the thermal simulation model. A plot showing how they are presented can be seen in **Figure 57**.

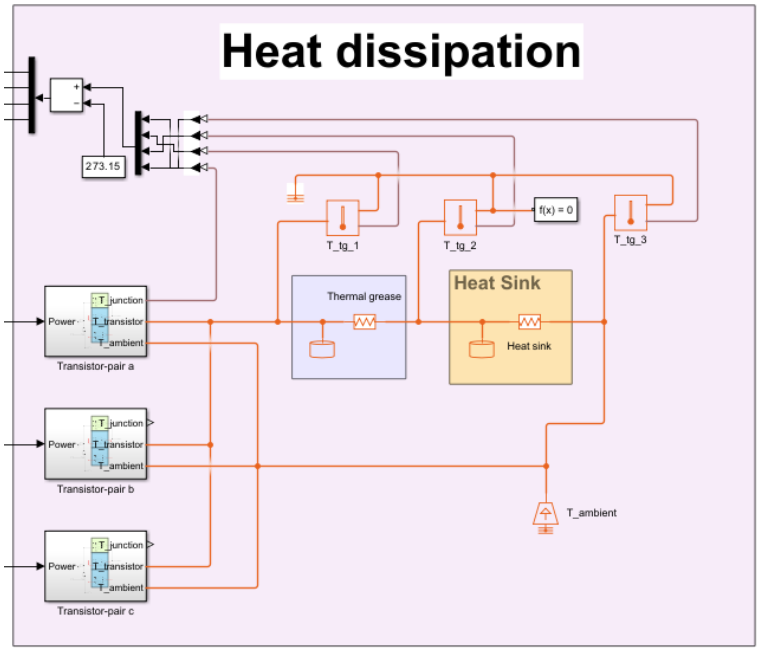

Figure 55: Thermal circuit Simulink model.

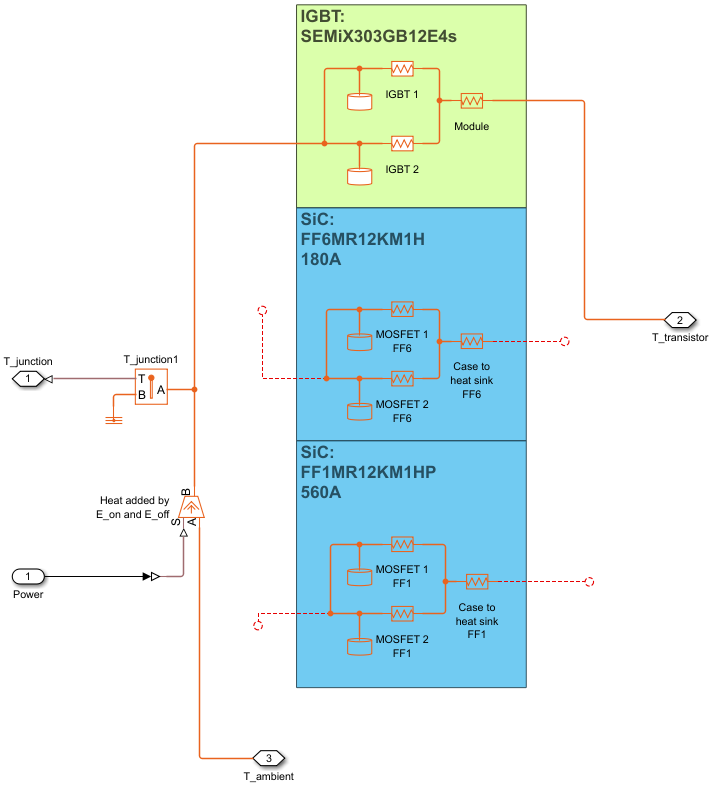

Figure 56: Thermal circuit transistors-pair block.

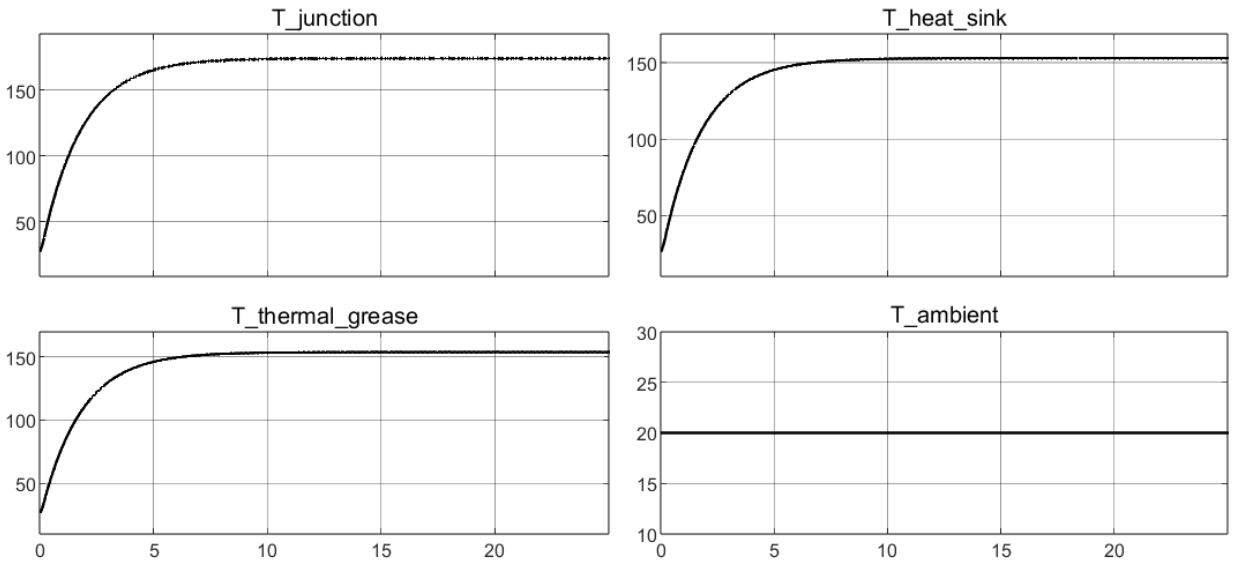

Figure 57: Temperatures at different locations of the thermal circuit.

3.4.6 PMSM Electromagnetic Model

The electromagnetic model calculates the dynamics of the PMSM by utilizing the equations from the mathematical model in section 2.1.1. It is divided into five main blocks: flux linkage equation, current equation, torque equation, dynamics and machine losses as can be seen in **Figure 58**. In this model the voltages from the power electronics simulation model are inputted and the physical parameters based on the measurements of the MGU011 consisting of winding resistance and permanent magnet flux are applied. The inductances and stator geometry are based on the Motor-CAD model which serves as a reference of the MGU011 in absence of detailed measurement data.

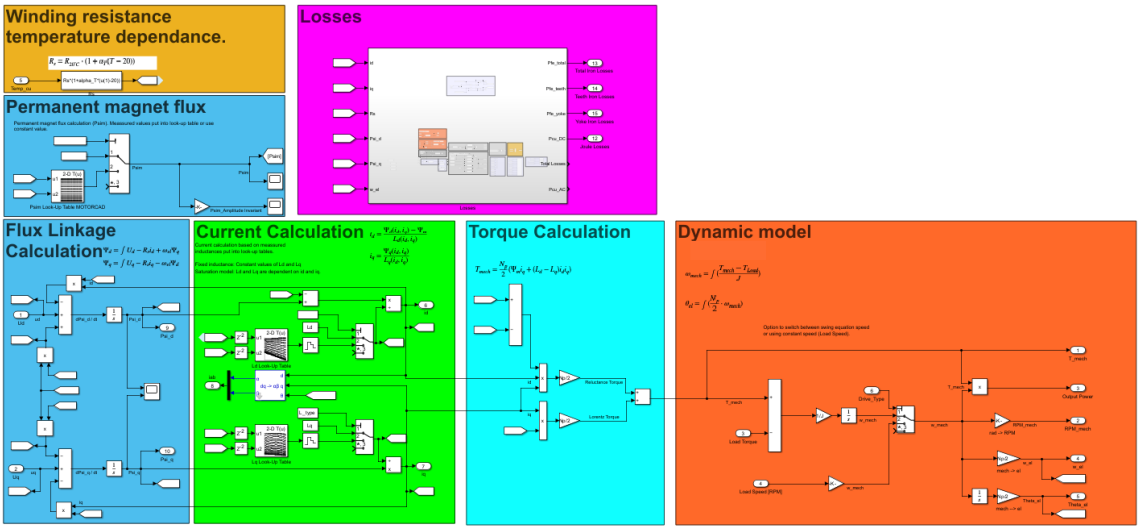

Figure 58: Full Simulink electromagnetic model.

3.4.6.1 *Flux linkage calculation*

The first block integrates the voltages in the machine into flux linkage using the rearranged voltage equations (2.11) and (2.12) and is implemented in Simulink as depicted in **Figure 59**.

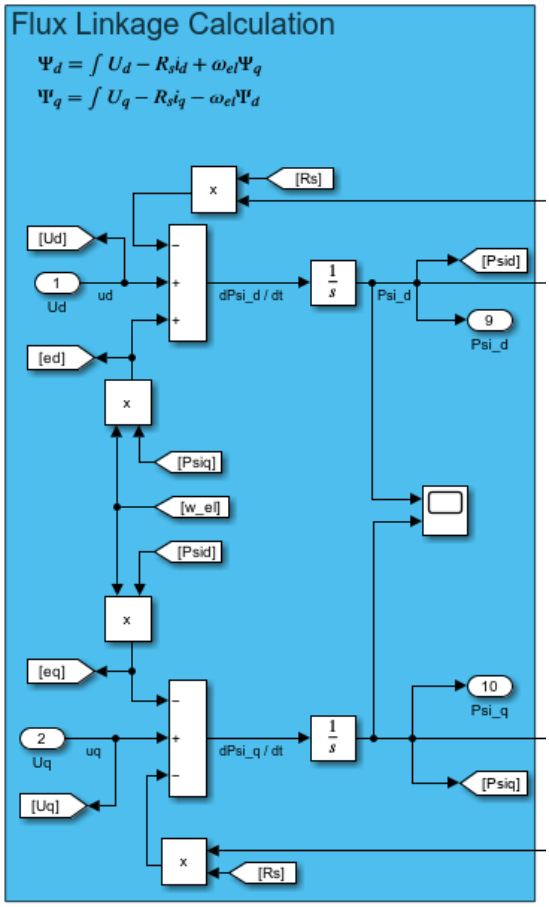

Figure 59: Simulink flux linkage calculation model.

As seen in **Figure 59**, the voltages u_d and u_q are input values from the power electronics model. These voltages are then run through the voltage integration which outputs the flux linkages Ψ_d and Ψ_q. The flux linkages are then routed back and multiplied with the electrical angular velocity ω_{el} to calculate the induced voltage. The resistive voltage drop is calculated by multiplying the winding resistance R_{s} with the currents i_d and i_q.

3.4.6.2 *Resistance temperature dependancy*

Since the resistance R_{s} is dependent on the temperature, equation (2.26) has been implemented to include this dependency which is represented in the Simulink model as depicted in **Figure 60**. However, the thermal model where the temperature is calculated is not bidirectional connected to the electromagnetic model and therefore must the winding temperature be set manually in the electromagnetic model.

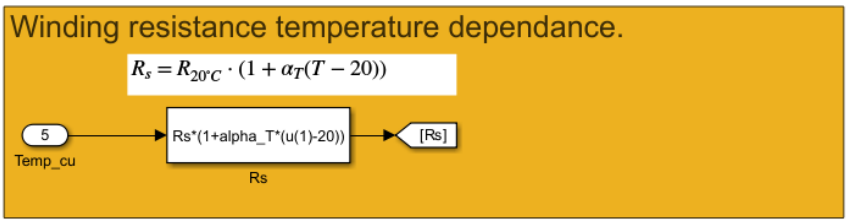

Figure 60: Resistance temperature dependence calculation.

3.4.6.3 Current Calculation

The currents i_d and i_q are calculated through equation (2.13) and (2.14) which is represented in Simulink model depicted in **Figure 61**.

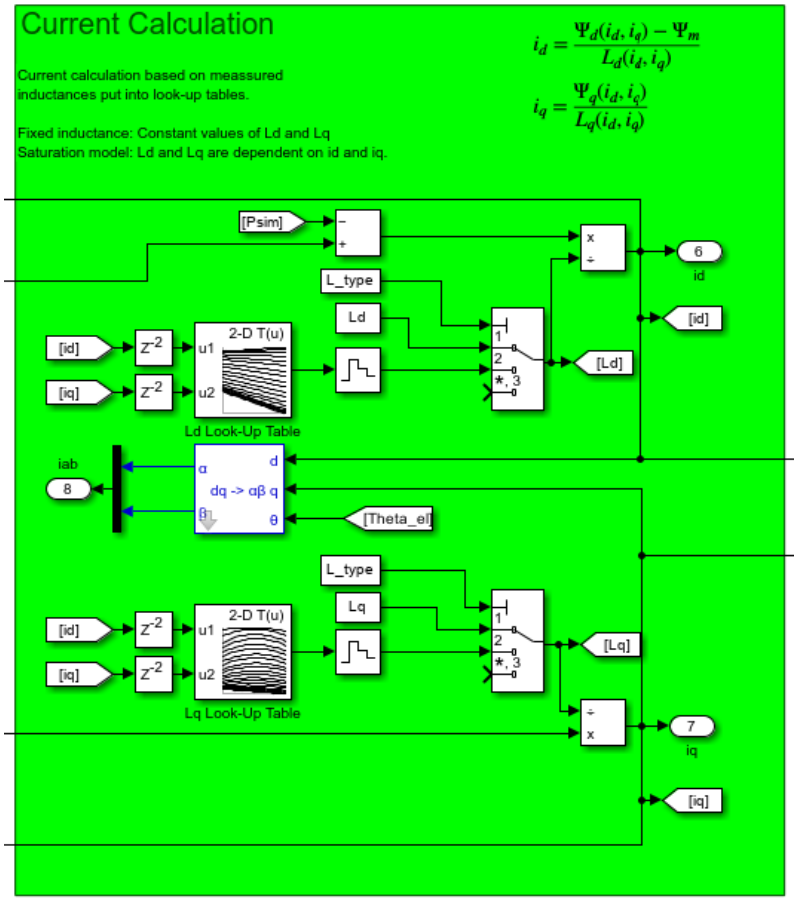

Figure 61: Simulink representation of current calculation.

Since the inductances are dependent on the current combination due to saturation effects in the core and magnetic cross-coupling, two look-up tables for L_d and L_q are implemented where measured values of the inductances for different current combinations are added. While measurements of these inductances are missing for the MGU011 machine, the inductances from the approximated Motor-CAD model are used as reference and are depicted in **Figure 62** and **Figure 63**.

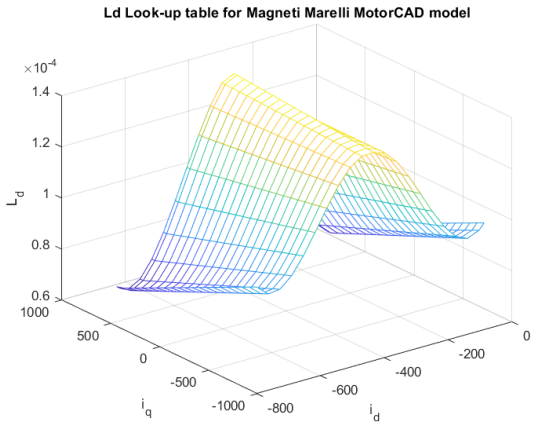

Figure 62: L_d look-up table from Motor-CAD model.

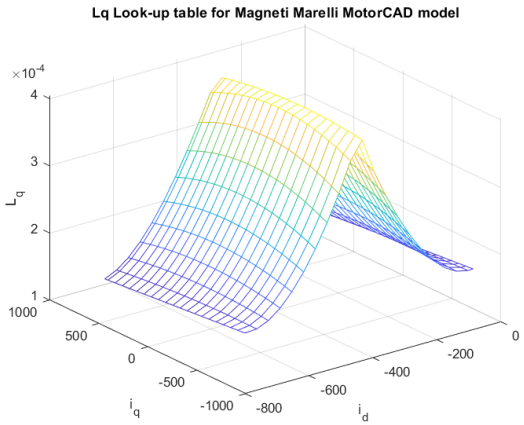

Figure 63: L_q look-up table from Motor-CAD model.

The way of calculating the currents is a bit problematic for the first time step in the simulation since both the inductances and currents are dependent on each other. Hence, a time delay of one time step with zero i_d and i_q is added before the look-up tables inputs which prevents the dependency loop. A sample and hold block is also implemented after the look-up tables in order to decrease the fluctuating currents due to too quick inductance changes.

If no look-up tables are available for the inductances, there is an option to use fixed inductances which is implemented as a multiport switch with input condition called L_type. This condition is set to either fixed inductances or saturation model in the mask of the PMSM simulation block.

3.4.6.4 Permanent magnet flux

The flux from the permanent magnets ψ_m named "Psim" in the Simulink model can either be set to a constant value or set to a current dependent flux which Simulink representation is shown in **Figure 64**.

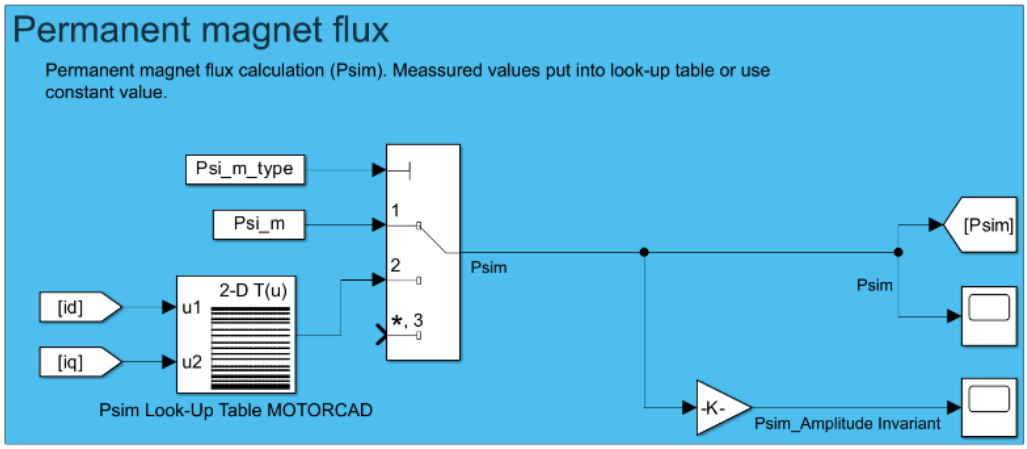

Figure 64: Simulink representation of the permanent magnet flux.

The current dependent permanent magnetic flux linkage is a look-up table based on exported data from Motor-CAD and is depicted in **Figure 65**. Although the Motor-CAD documentation does not explicitly describe how the flux linkage depends on the current, the corresponding look-up table must be implemented in the Simulink model when using the inductance values exported from Motor-CAD. This ensures that the flux linkages in the Simulink simulation are consistent with those from Motor-CAD.

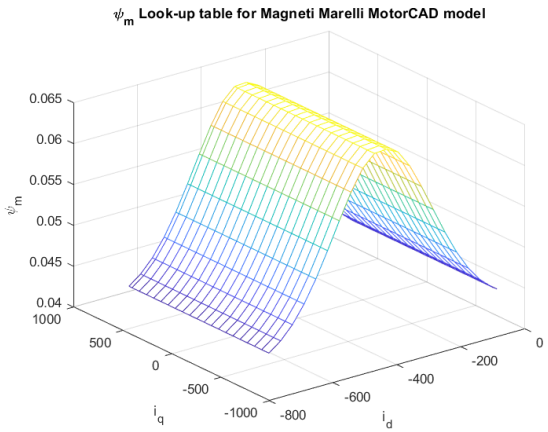

Figure 65: ψ_{m} look-up table exported from Motor-CAD.

However, if the inductance values are derived from measurements of the reference machine rather than from Motor-CAD, the flux linkage from the permanent magnets, ψ_{m}, should be treated as a constant which in this particular case is in range of 63 mVs. This is because the measured inductances, which can be calculated by rearranging the voltage equation seen in Equation (3.24) and (3.25), include the effect of the permanent magnet flux.

$$L_{\mathrm{d}} = \frac{u_{\mathrm{qs}} - R_{\mathrm{s}} i_{\mathrm{qs}} - \psi_{\mathrm{m}} \omega_{\mathrm{el}}}{\omega_{\mathrm{el}} i_{\mathrm{ds}}} \tag{3.24}$$

$$L_{\mathrm{q}} = \frac{R_{\mathrm{s}} i_{\mathrm{ds}} - u_{\mathrm{ds}}}{\omega_{\mathrm{el}} i_{\mathrm{qs}}} \tag{3.25}$$

By using a fixed value for the permanent magnet flux linkage, the inductances effectively capture the variation in flux linkage, allowing the nonlinear behavior to be represented within the inductance values themselves.

3.4.6.5 Torque Calculation

The torque is calculated using equation (2.17) which is represented in the Simulink model depicted in **Figure 66**.

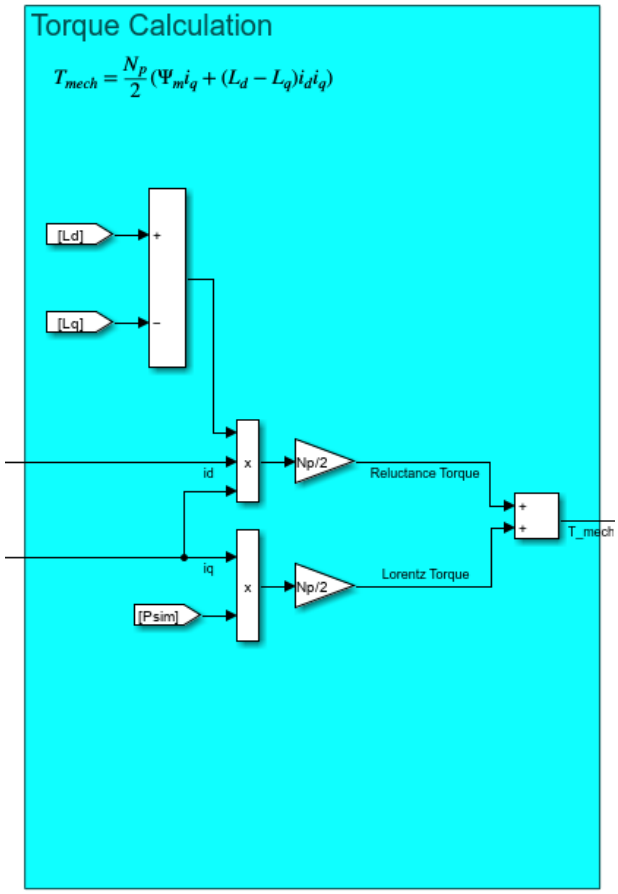

Figure 66: Simulink representation of torque equation.

3.4.6.6 Dynamic model

The rotational speed of the machine is calculated by Equation (2.20). However, since the generator is mechanically coupled to the jet turbine shaft, its rotational speed is dictated by the turbine speed during generator operation. As a result, the machine speed can be treated as constant, and the motor dynamics can be omitted. This behavior is controlled via the "Drive_Type" parameter in the PMSM model mask, which allows the user to select between two operating modes: "Dynamic" or "Fixed Speed". In addition to the rotational speed, the electrical rotor angle θ_{el} is calculated by integrating the rotational speed as can be seen in **Figure 67**.

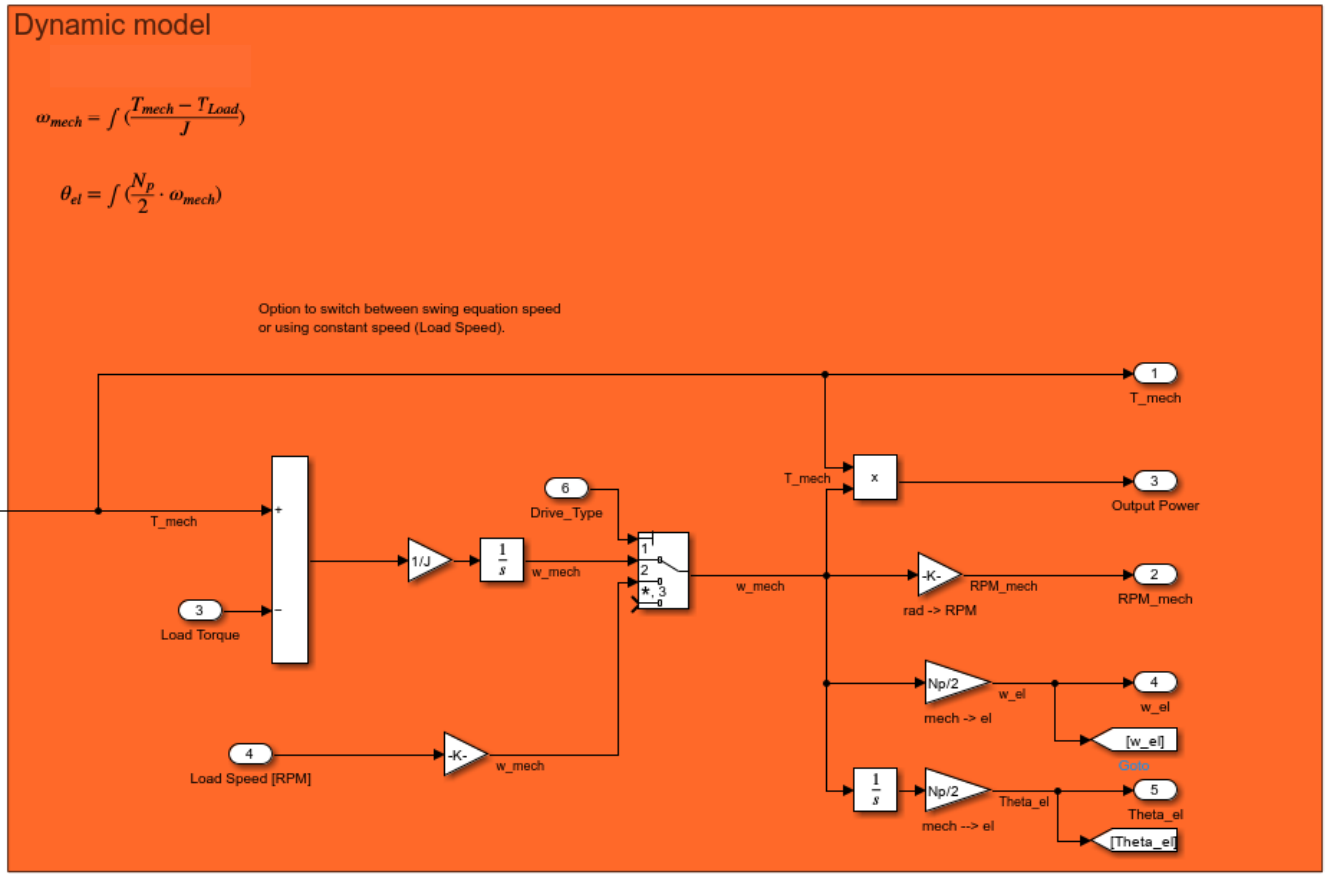

Figure 67: Simulink representation of the dynamical model

3.4.6.7 Loss estimation model

The Simulink loss model consists of resistive DC-losses and a rough estimation of iron losses which is depicted in **Figure 68**.

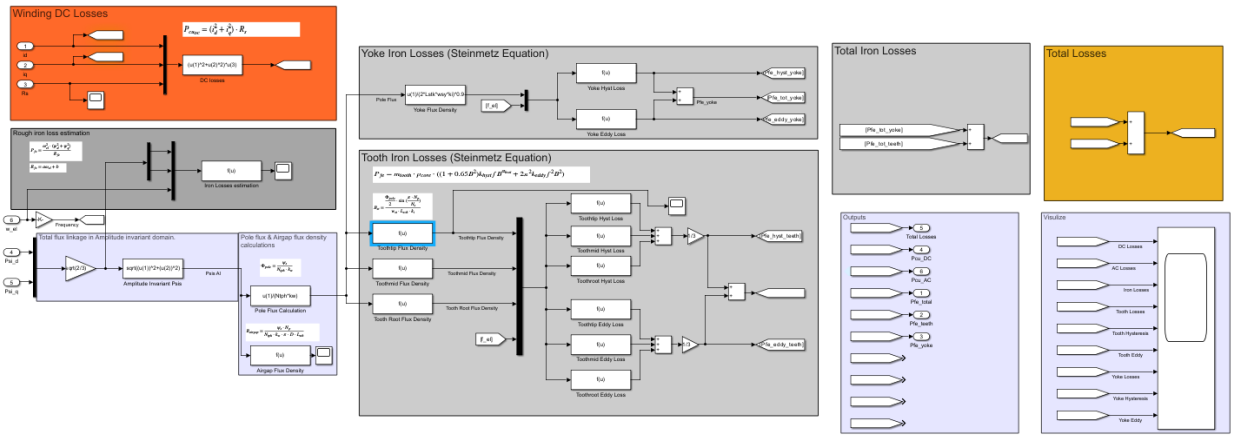

Figure 68: Simulink loss estimation model of PMSM

In the mathematical model of the PMSM, estimating losses presents several challenges, particularly in the absence of finite element analysis. The Simulink model is based on a system of differential equations that

describe the electrical and mechanical behavior of the machine but complex phenomena such as magnetic flux distribution within the iron core is hard to estimate which is crucial in order to accurately calculate the iron losses. Hence, the iron losses in the Simulink model is a rough estimation.

The iron losses are based on the Steinmetz equation (2.27) which requires the flux density in the iron core and the frequency of the varying magnetic field as explained in section 2.1.1.5. To determine the flux density in the core, the flux linkage must first be converted into the pole flux. The implementation of this conversion in the Simulink model is illustrated in **Figure 69**.

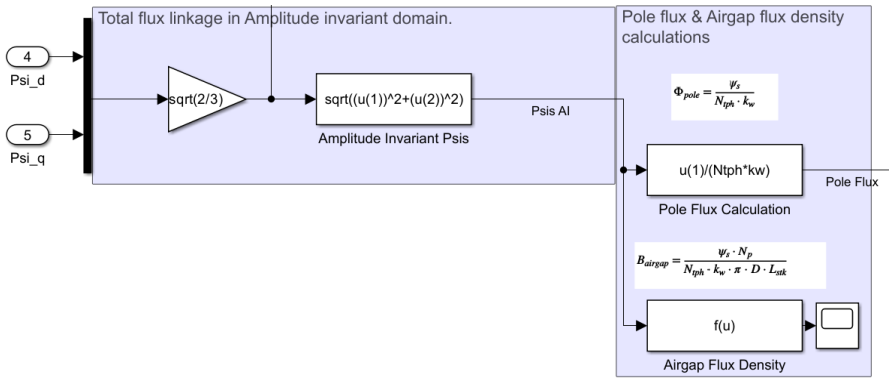

Figure 69: Simulink representation of flux linkage to pole flux conversion.

Once the pole flux is determined, the magnetic flux density in the stator tooth can be estimated. Due to the non-rectangular geometry of the tooth, three tooth widths are considered to calculate the corresponding cross-sectional areas and flux densities. These individual flux densities, calculated with equation (2.35), are then used in the Steinmetz equation (2.27) to compute the localized iron losses. Finally, the losses are averaged, yielding the mean loss in the tooth as seen in **Figure 70**.

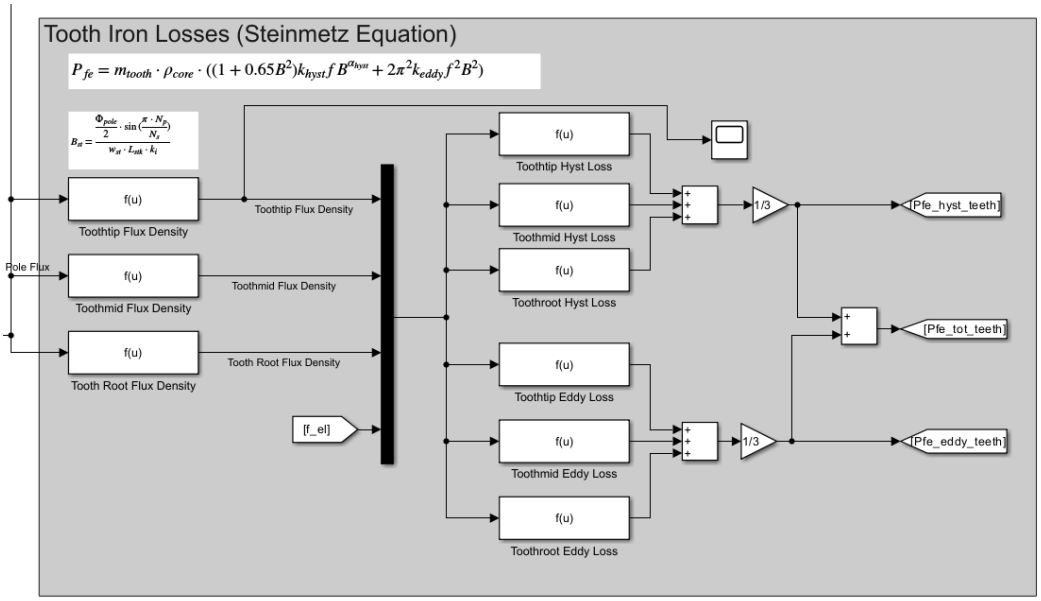

Figure 70: Simulink representation of tooth iron loss estimation.

The yoke losses are estimated in a similar way, using the Steinmetz equation, in which the magnetic flux density is determined according to Equation (2.36). The resulting Simulink representation is illustrated in **Figure 71**.

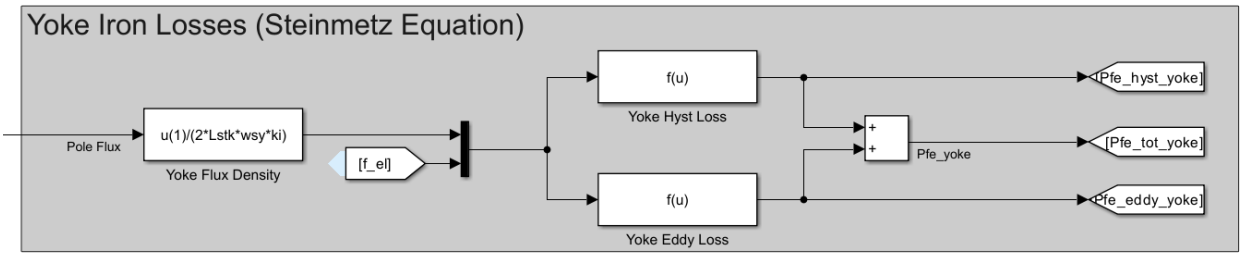

Figure 71: Simulink representation of yoke iron loss estimation.

The DC losses depend on both the winding resistance and the *d*- and *q*-axis currents shown in Equation (2.25). The resistance is provided as an input parameter, based on the measurement described in Section 3.1.4. The currents are computed in the current calculation block explained in Section 3.4.6.3 and serve as inputs to the DC loss calculation block, illustrated in **Figure 72**.

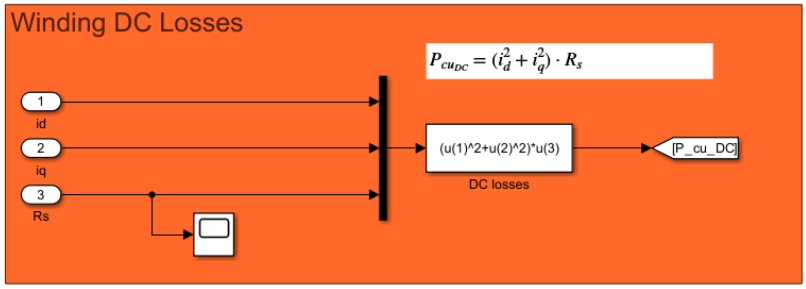

Figure 72: Simulink representation of DC-loss calculation.

3.4.7 PMSM Thermal Model

The thermal model of the electric machine is crucial since it gives an indication of how the temperature relates to the operation of the machine. In order to get an estimated thermal behavior connected to the electromagnetic model, a thermal model is built in Simulink which inputs the losses from the electromagnetic model and simulates the temperature rise in the machine. This is done by building a lumped parameter network of thermal resistances and capacitances modelling the thermal path from one slot to the cooling sleeve shown in **Figure 73**.

To accurately represent the real operating conditions of the machine in terms of operation time, the thermal model is implemented in a separate file. This separation is necessary because the power electronics model includes detailed switching behavior, which significantly slows down the simulation. In contrast, the thermal model is computationally more efficient and can simulate extended operating durations within a few seconds.

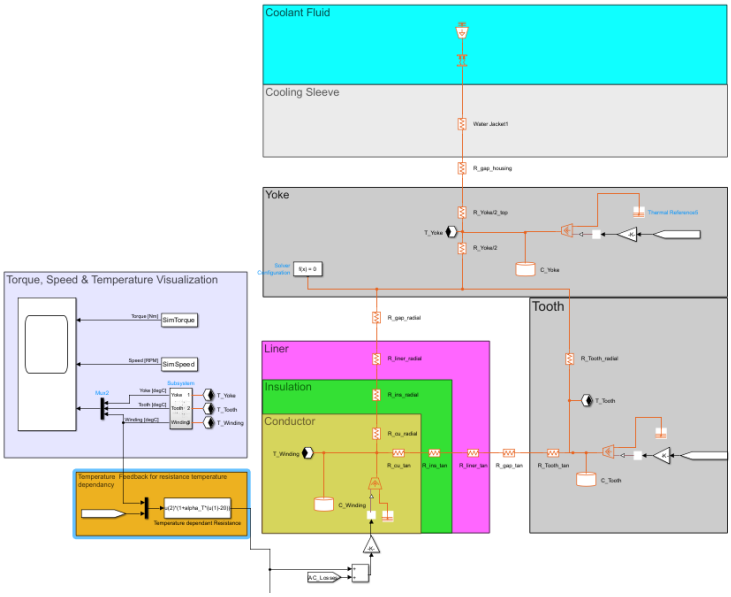

Figure 73: Simulink thermal model

The MGU011 has two temperature sensors attached at two different nodes. Since the position of these sensors are unknown, a qualified guess is made and is based on commonly used positions. In this case the nodes that are assumed as possible positions are the winding, the stator tooth and the stator yoke. Therefore, the thermal model is built around these nodes. To estimate the temperature rise in these regions of the machine, a simplified thermal model is developed depicted in **Figure 74**.

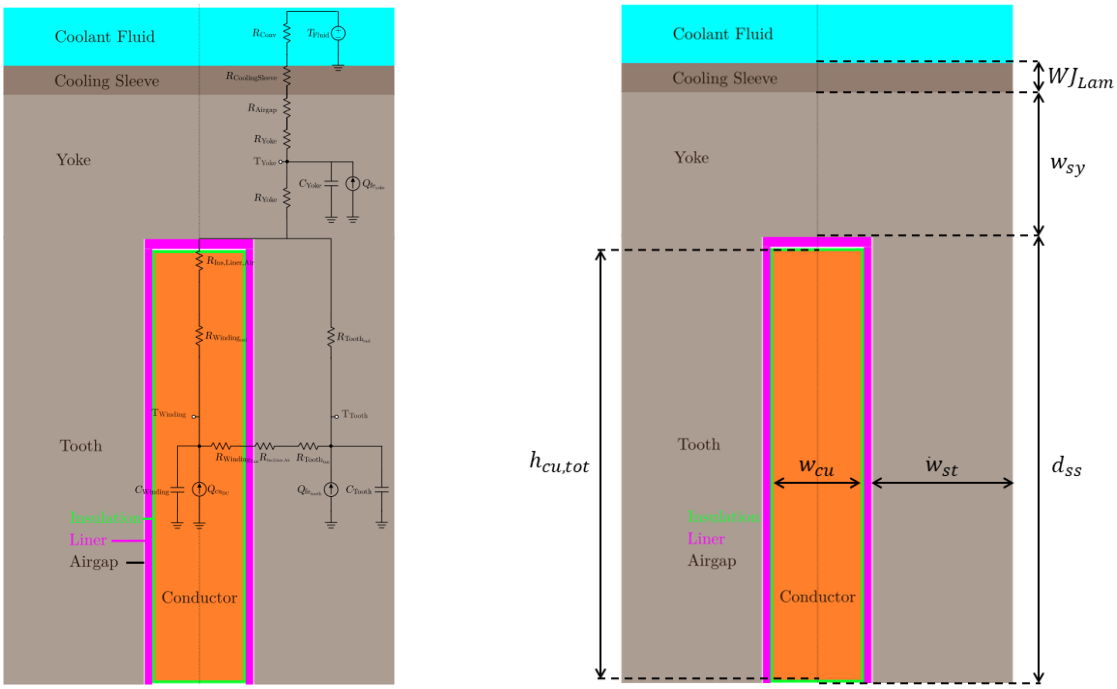

Figure 74: Lumped parameter thermal network of half a stator slot (left) and the dimensions (right).

Figure 74, illustrates a single stator slot, where the winding conductors have been simplified to a single equivalent conductor for modeling purposes. To further reduce the complexity of the thermal network, heat transfer is modeled from the center of the winding through half of a stator tooth, in series with the stator yoke and the cooling sleeve. From the center of the conductor, the thermal network branches into two parallel heat flow paths: one in the radial direction toward the stator yoke, and another in the tangential direction through the stator tooth, which is represented horizontally in **Figure 74**.

The model includes three heat sources: winding losses and iron losses from both the stator tooth and yoke which are inputs from the electromagnetic model or can be set manually. With a thermal model representing one half of a slot and tooth, the input power must be modified to represent this fraction of the machine given by:

$$P_{\mathrm{loss_{model}}} = \frac{P_{\mathrm{loss_{input}}}}{N_{\mathrm{s}} \cdot 2} \tag{3.26}$$

To simplify the model, a constant temperature is assumed for the cooling fluid, neglecting the influence of ambient temperature. To capture the transient thermal behavior, the model incorporates three thermal capacitances associated with the thermal masses of the winding, tooth, and yoke.

Since the thermal resistance and capacitance values are dependent on the geometry of the machine described in equation (2.48) and (2.50), an approximated geometry based on the Motor-CAD model is used as a reference. The calculation of the resistances and capacitances are shown in the appendix section 9.1.

Since the winding resistance is dependent on the temperature, Equation (2.26) is modified and implemented in the thermal model as seen in **Figure 75**. As an increase in resistance increases the DC-loss linearly, the resistance in Equation (2.26) is swapped with the DC-loss giving the following expression.

$$P_{\mathrm{DC}} = P_{\mathrm{DC_{20°C}}}\big(1 + \alpha_{\mathrm{T}}(T - 20)\big) \tag{3.27}$$

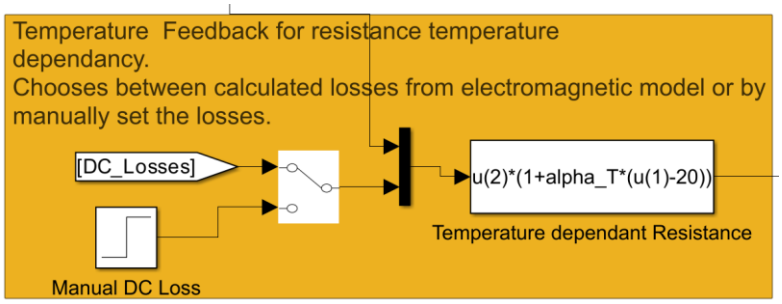

Figure 75: Simulink representation of winding DC-loss temperature dependency.

4 MACHINE TESTING

To validate the simulation models, a comparison is carried out between the simulation models and the reference machine, the MGU011 from Magneti Marelli. The validation process includes comparing the output torque for specified speed and current references, comparing the losses, and comparing the thermal behavior. To perform this comparison, experimental data from the MGU011 must be obtained. This is accomplished using the test rig provided by GKN Aerospace, shown in **Figure 76**. The test setup includes torque and speed sensors and allows for the connection of two machines on a shared axle, enabling one machine to operate as a braking machine during testing.

Figure 76: Test rig from GKN for electric machine testing.

4.1 Torque Measurements

The output torque is dependent on the different *d*- and *q*-axis current combinations due to the reluctance difference within the machine. This reluctance difference is difficult to model without knowing the actual internal geometry. Hence, the torque in the simulation models is compared to the torque from the actual machine to give an indication of how close the models match the real machine.

The measurements were conducted while the machine was operating against the speed controlled braking machine running at 1000 rpm. Fixed *d*- and *q*-axis currents references were set to the current controller while the torque was measured with the torque sensor in the test rig giving the torque measurements shown in **Table 10**.

Table 10: Torque measurements of MGU011.

Phase Angle [deg]	Is [A]	Id [A]	Iq [A]	Torque [Nm]	Speed [rpm]
45	141.42	-100	100	30	1000
63.43	223.6	-200	100	37	1000
15.95	182	-50	175	45	1000
0	300	0	300	65	1000
45	424.26	-300	300	118	1000
26.57	447.21	-200	400	122	1000

4.2 Temperature & Machine Losses Measurements

In order to validate the thermal model of the MGU011 and estimate the temperature sensor position, the machine temperature was measured while the machine was running at different operation points. During operation the machine was cooled with tap water.

The first measurement was conducted while having the machine running against a speed controlled braking machine keeping a desired axle speed while the other machine was set to different torque values by setting the *d*- and *q*-axis currents to the corresponding desired torque. While the machine was running at the desired operating point, the temperature was measured using the two pt100 sensors which are positioned within the machine at two unknown locations. The desired operating points for the temperature measurements are defined in three drive cycles but are classified and cannot be shown in the report. However, the measured temperatures from those experiments, along with the corresponding simulated temperatures for the same drive cycles, are presented in the Section 9.2.

The second temperature measurement was conducted while the machine was operating with no braking machine. This approach requires a speed-controlled current controller that modulates the *q*-axis current to control the torque, while allowing manual adjustment of the *d*-axis current. The steady-state temperature was then measured for different speed and current combinations and compared to the simulation models.

By setting different speed references, the iron loss increase can be analyzed which is dependent on the rotational frequency mentioned in Section 2.1.1.5. This measurement also includes a power analyzer in order to measure the input power to the machine and since there is no braking machine, the output power is close to zero since there is no output torque. Hence, the input power corresponds to the losses in the machine which can be used for comparison with the losses in the simulation models. The different operating points measured are listed in the table below.

Table 11. Operating points during operation without braking machine.

Speed [rpm]	Id [A]	Iq [A]
3150	-50	5.6
5987	-50	12
8975	-50	21
11976	-50	30.5
15050	-50	43
3000	-300	20
6000	-300	63
9000	-282	100
11970	-267	142

5 RESULTS & ANALYSIS

This chapter starts with the results and analysis of the PMSM model verification in Section 5.1. This is then followed by Section 5.2 which covers the sensitivity analysis of the electric machine design and finally, in Section 5.3, the results and analysis of the full Simulink model is presented.

5.1 PMSM Model Validation

In this section, the accuracy of the developed mathematical model implemented in Simulink and the Motor-CAD model are evaluated. The validation consist of comparing the models against measurements on the MGU011 from Section 4, including output torque for different *d*- and *q*-axis current combinations, losses in the machine and the thermal behavior.

5.1.1 Torque Validation

With the torque measurements of the MGU011 machine, the simulation models are compared, using the same current references. Since the Simulink model uses a power invariant transformation all current references used as inputs in the Simulink model are scaled with $\sqrt{\frac{3}{2}}$. The results are listed in **Table 12** with amplitude invariant current references.

Table 12: Torque comparison between MGU011 and simulation models where the percentage inside the parentheses shows the difference between the model and measurement.

Id* [A]	Iq* [A]	Speed [rpm]	Torque [Nm] MGU011	Torque [Nm] Motor-CAD	Torque [Nm] Simulink
-100	100	1000	30	33 (10%)	33 (10%)
-200	100	1000	37	43.86 (18.5%)	43.7 (18.1%)
-50	175	1000	45	45.38 (0.8%)	45.4 (0.9%)
0	300	1000	65	58.26 (-10.4%)	58.3 (-10.3%)
-300	300	1000	118	115.2 (-2.4%)	115.3 (-2.3%)
-200	400	1000	122	111 (-9.0%)	111.3 (-8.8%)

The torque measurements indicate that the Simulink model aligns well with the Motor-CAD model in terms of torque output across various current combinations. However, both simulation models deviate from the measured torque. The torque deviation increases as the proportion of *d*-axis current becomes more dominant. This behavior is expected, as a negative *d*-axis current contributes to the reluctance torque, which depends on the machine's inductances. With an unknown internal machine geometry and core material, it is difficult to accurately determine inductance values that closely match those of the actual machine. Hence, the reluctance torque will deviate from the actual reluctance torque.

The deviation at the operating point where only *q*-axis current is applied indicates that the permanent magnet flux is different in the models compared to the real machine. In theory, this operating point should only generate Lorentz torque as explained in Section 2.1.1.2. Hence, the flux linkage is only dependent on the permanent magnet flux linkage and the *q*-axis current. Since the flux linkage seem to be lower in the simulation models it may be due to higher saturation effects in the core. By running a FEA simulation of

the corresponding operation point depicted in **Figure 77** , the flux distribution in the yoke shows a high flux density in some regions indicating there may be saturation effects in the yoke.

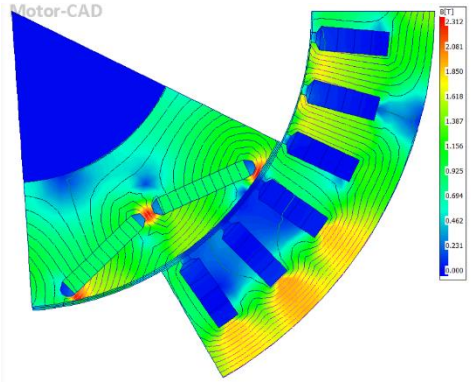

Figure 77: Flux density plot with 300A *q*-axis current & 0A *d*-axis current @1000rpm.

Increasing the yoke width by 3 mm in the Motor-CAD model, reduces the saturation effects, resulting in an overall increase in output torque, shown in **Table 13**.

Table 13: Torque comparison between MGU011 and two different Motor-CAD models.

Id* [A]	Iq* [A]	Speed [rpm]	Torque [Nm] MGU011	Torque [Nm] Motor-CAD Original Design	Torque [Nm] Motor-CAD Increased Yoke Width
-100	100	1000	30	33 (10%)	33.84 (12.7%)
-200	100	1000	37	43.86 (18.5%)	43.63(17.9%)
-50	175	1000	45	45.38 (0.8%)	48.95 (8.78%)
0	300	1000	65	58.26 (-10.4%)	65.94 (1.45%)
-300	300	1000	118	115.2 (-2.4%)	132.4(12.2%)
-200	400	1000	122	111 (-9.0%)	129.6 (6.23%)

Increasing the yoke width results in a model that more accurately matches the torque at the operating point with only *q*-axis current. However, this modification also leads to greater deviations at other operating points, highlighting the difficulty of achieving a model that consistently reflects the real machine's behavior.

5.1.2 Losses validation

From the measurements using the power analyzer, only those conducted with low *d*-axis current magnitude are considered valid. The reason for this is guessed to be the flux weakening effect which reduces the voltage magnitude which the power analyzer is using as reference for calculating the power. As a result, the power analyzer is unable to provide any power measurements under conditions of strong flux weakening with higher *d*-axis current magnitude.

The measured input power of the fundamental frequency is compared to the total losses in the simulation models. By calculating the DC losses based on the measured phase currents and winding resistance using Equation (2.25), and subtracting these losses from the measured input power, an estimation of the combined iron and AC losses can be obtained. The measured data is listed in **Table 14**.

Table 14: Current and power measurements of MGU011 with calculated DC-losses and estimated Iron & AC losses.

Speed [rpm]	Id* [A]	Iq* [A]	Ia [Arms]	Ib [Arms]	Ic [Arms]	Input Power [W]	DC-losses [W]	Iron & AC losses [W]
3150	-50	5.6	32.9	32.6	33.2	183	16	167
5987	-50	12	33	32	33.5	385	16	369
8975	-50	21	35.2	34.5	37.2	702	19	682
11976	-50	30.5	38.2	41.3	39.6	1308	24	1284
15050	-50	43	46.7	47.7	46	3000	33	2967

The Motor-CAD and Simulink model can be compared to the measurements by running the simulation with the same current and speed references. The results of those simulations are illustrated in **Table 15** and **Table 16**.

Table 15: Simulated losses with the Motor-CAD model for given speed and current combinations.

Speed [rpm]	Id* [A]	Iq* [A]	Total Losses [W]	DC-Losses [W]	Iron + AC Losses [W]	Iron & AC Losses Difference With Measured Losses [W]
3150	-50	5.6	166	19	144 + 3	-20
5987	-50	12	415	20	385 + 10	26
8975	-50	21	799	22	754 + 22	93
11976	-50	30.5	1314	26	1254 + 34	4
15050	-50	43	2030	33	1941 + 54	-972

Table 16. Simulated losses with the Simulink model for given speed and current combinations.

Speed [rpm]	Id* [A]	Iq* [A]	Total Losses [W]	DC-Losses [W]	Iron + AC Losses [W]	Iron & AC Losses Difference With Measured Losses [W]
3150	-50	5.6	154	19	135	-32
5987	-50	12	331	20	311	-58
8975	-50	21	586	22	564	-118
11976	-50	30.5	926	26	900	-384
15050	-50	43	1398	33	1365	-1602

By analyzing the simulation results, it is noticeable that the losses in the Motor-CAD model is closer to the measured losses. At 15000 rpm, the iron- and AC-losses significantly deviates from the measured loss in both simulation models. This discrepancy may be attributed either to inaccuracies in the power analyzer measurements or that the simulation models cannot accurately represent the operation point. It is also noticeable that the iron losses in the Simulink model deviates more with the increase in rotational speed indicating that the iron loss model in Simulink is not that accurate. Hence, the Motor-CAD model seems to be a better candidate for evaluating the losses of the machine.

5.1.3 Thermal model validation

To validate the thermal models in both Motor-CAD and Simulink, temperature measurements from Section 4.2 are compared with the corresponding simulation results obtained by running the same operation points in each model with tap water as coolant. Due to significant deviations in the iron loss estimations from the Simulink model compared to both the Motor-CAD model and the measured losses, the input losses for the Simulink thermal model are instead taken from the Motor-CAD simulations and inputted manually to the model. This approach allows for evaluating the accuracy of the Simulink thermal model relative to the more advanced thermal modeling capabilities of Motor-CAD.

The results from the measurements and the simulations during the three drive cycles are illustrated in Section 9.2 in the appendix. From the results, the thermal models aligns well with each other and relatively well with the measurements. Both simulation models shows a slightly lower temperature than the measurements which has to be taken into account when running further simulations. The assumption that the temperature sensors are positioned at the winding and the tooth or yoke seems valid. The simulations shows that the sensor at the winding and tooth agrees relatively well with the measurement.

The second validation of the thermal model involves comparing the steady-state temperatures obtained while operating the machine without a braking machine, during which the speed and *d*-axis current are varied. As the electromagnetic model in Simulink does not accurately represent the iron losses and neglects the AC-losses, only the Motor-CAD model is validated against these measurements. The resulting temperature values are presented in **Table 17**.

Table 17. Steady state temperature measurements and Motor-CAD simulation.

Speed [rpm]	Id* [A]	Iq* [A]	Temp-Sensor1 [C]	Temp-Sensor2 [C]	Winding Motor-CAD [C]	Tooth Motor-CAD [C]	Yoke Motor-CAD [C]
3150	-50	5.6	18.6	16.5	15.7	15.2	14.9
5987	-50	12	22.5	19.5	18.7	18	17.2
8975	-50	21	28.9	24.2	23.4	22.4	20.7
11976	-50	30.5	36.6	29.8	29.5	28	25.4
15050	-50	43	46.2	36.5	38.3	35.9	31.9
3000	-300	20	65	36.5	45.3	25.5	21.7
6000	-300	63	76.4	44.5	56	33.1	27.2
9000	-282	100	84.5	50.5	69.3	44.2	35.3
11970	-267	142	103	61.5	91.3	61.3	48.6

Similar to the transient simulations of the three drive cycles, the steady-state simulation results indicate that the winding and tooth temperatures show the closest agreement with the two temperature sensors. While the overall simulated temperatures remain slightly lower than the measured values, the results

demonstrate reasonably good agreement with the measurements. Therefore, by taking the slightly lower overall temperature into account, the thermal models can be considered reasonably reliable for representing the machine's thermal behavior.

5.2 Sensitivity Analysis of Electric Machine

To evaluate the impact of key design parameters and cooling strategies on the thermal performance of the electric machine, a sensitivity analysis is conducted. This analysis aims to identify how variations in cooling fluids, cooling topology configurations, and machine geometry influence the temperature distribution within the machine. The impact of using different magnet material is also evaluated. The purpose of this comparison is to find a direction of machine design with an acceptable ability to dissipate heat under the given operating conditions. As mentioned in Section 2.1.3, the temperature limits for the windings using conventional insulation is around 165 ℃ and the maximum magnet working temperature is 150 ℃ and are used as references for evaluating the thermal performance.

The simulations are conducted using two drive cycles that represent the system requirements of the machine, illustrated in **Table 18**.

Table 18. System requirement Drive Cycles.

Drive Cycle	Power [kW]	Speed [rpm]	Torque [Nm]	Duration [sec]
Cruise	100	17000	56.2	2700
Idle	100	12750	74.9	1350

Since the application for the electric machine is within an aircraft, there is a certain limitation of available cooling fluids. Two available fluids are water glycol mixture (EGW 60/40) and Jet A1 fuel listed in **Table 19**.

Table 19. Cooling fluid properties.

Cooling Fluid	Thermal Conductivity [W/mC]	Density [kg/m^3]	Cp [J/kgC]	Kinematic Viscosity [m^2/s]	Dynamic Viscosity [kg/ms]	Prandtl Number	Temp Min [C]	Temp Max [C]
EGW 60/40	0.3678	1068	3358	1.8e-6	0.001996	18.23	20	60
Avtur Jet A1 Fuel	0.1116	795	2039	1.22e-6	0.0009699	17.72	80	100

The different coolants has a certain estimated temperature span. However, the machine must be able to operate in the worst case scenario and therefore the max temperature of the fluids are used under the simulations.

5.2.1 Cooling Topologies

To evaluate what cooling strategy is suitable to fulfill the system requirements of the electric machine. Different cooling topologies in Motor-CAD are evaluated and simulated with the given drive cycles and cooling fluids from GKN Aerospace.

5.2.1.1 Spiral Water Jacket (Original Design)

The MGU011 is assumed to use a conventional spiral water jacket. By running a transient thermal simulation using Motor-CAD with the given cooling fluids from GKN, the heat transfer capability can be evaluated. The resulting thermal behavior is illustrated in **Figure 78** and **Figure 79**.

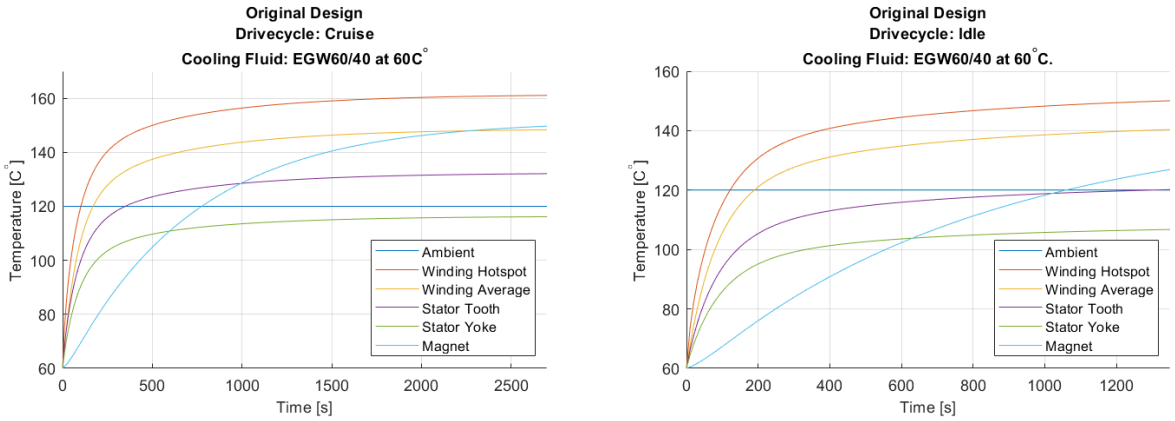

Figure 78: Transient thermal simulation of spiral water jacket using EGW60/40 as coolant.

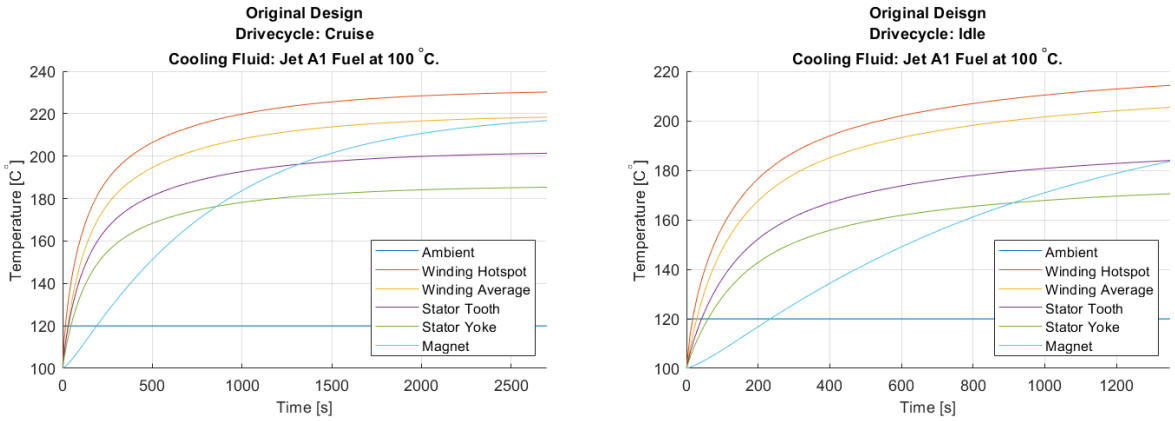

Figure 79: Transient thermal simulation of spiral water jacket using Jet A1 Fuel as coolant.

5.2.1.2 Slot Cooling

To increase the heat transfer capability, two different type of slot cooling is evaluated using built in slot cooling topologies in Motor-CAD. The first slot cooling topology is using a cooling channel close to the tooth tip as shown in **Figure 80**.

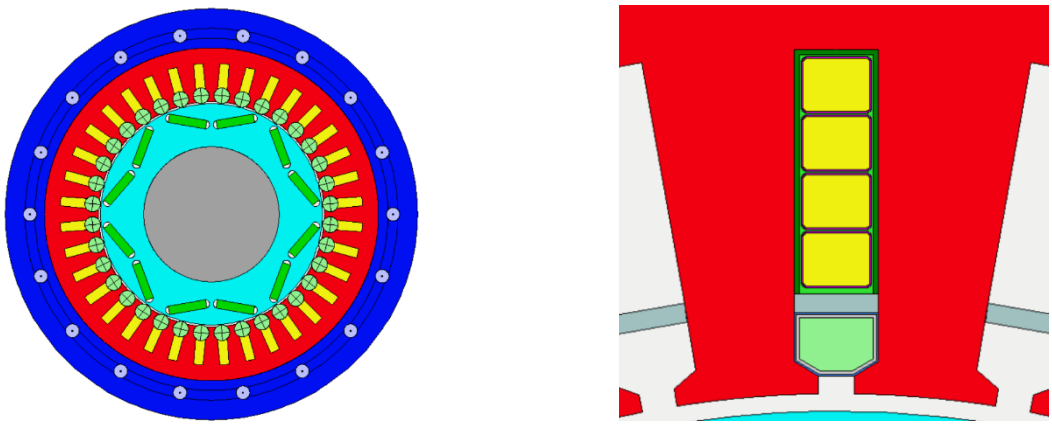

Figure 80: Slot cooling at tooth tip.

In addition to the slot cooling, the spiral water jacket is kept. Given that the total cooling fluid flow is measured at 4 liters per minute, it is assumed to be evenly divided between the two parallel cooling paths, resulting in a flow rate of 2 liters per minute in each system. As the cooling channel is added the geometry of the stator slot is adjusted to fit the channel as well as the rotor diameter is decreased. Hence, the magnets have to increase in size for the flux linkage to remain the same, resulting in the new internal geometry listed in **Table 20**.

Table 20: New dimensions with slot cooling at tooth tip.

Dimension	Value	Unit
Rotor Diameter (D_r)	113	mm
Stator Slot Depth (d_{ss})	19.5	mm
Magnet Width (w_m)	19.1	mm
Magnet Height (h_m)	4.2	mm

The second slot cooling method is similar to the previous but instead of using a cooling channel at the tooth tip, the coolant is flowing between the conductors without any channel. For this topology the geometry from the first slot cooling topology is kept to give space for the coolant to flow between the conductors. Motor-CAD has no detailed visual representation of this cooling topology and is visualized as **Figure 81**. This cooling method is representing direct contact between the coolant and the conductors which increase the heat transfer capability.

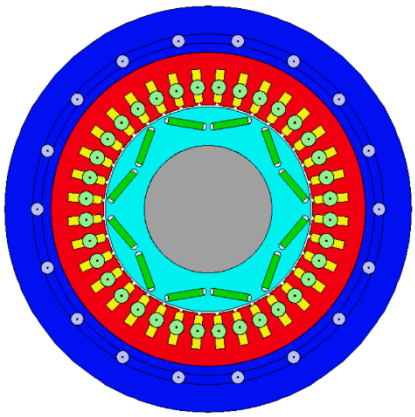

Figure 81: Slot cooling between conductors.

The resulting transient temperature simulations of the two slot cooling topologies are presented in **Figure 82**, **Figure 83** and **Figure 84**. As the slot cooling at the tooth tip, does not show any improvement, it is not simulated with jet fuel as coolant.

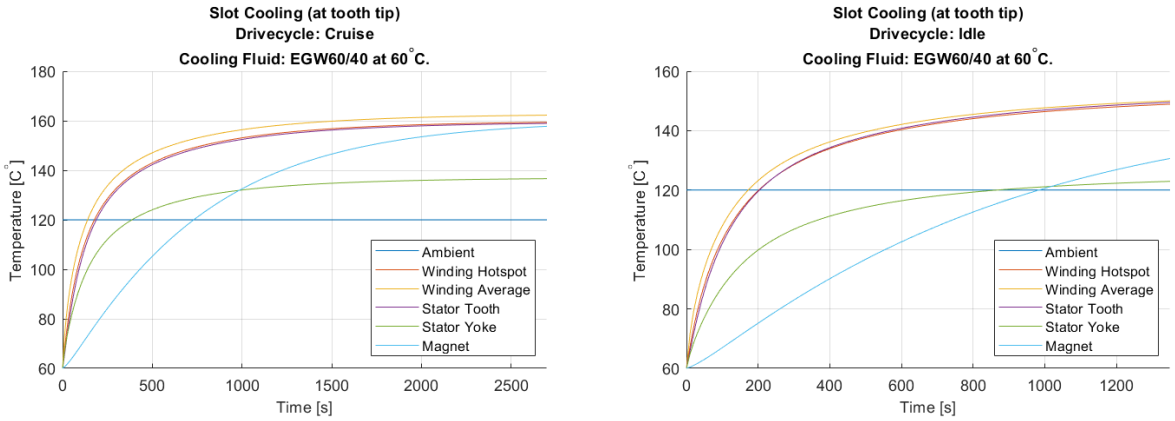

Figure 82: Transient thermal simulation of slot cooling at tooth tip using EGW60/40 as coolant.

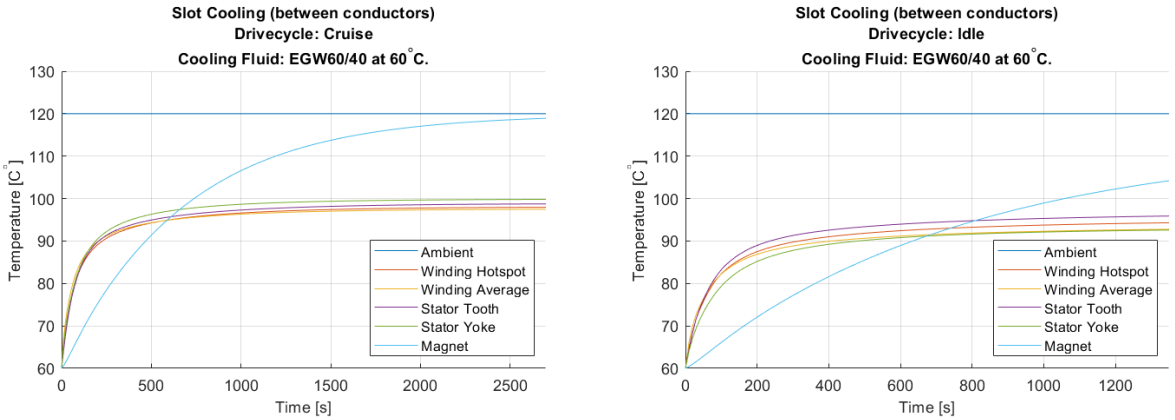

Figure 83: Transient thermal simulation of slot cooling between conductors using EGW60/40 as coolant.

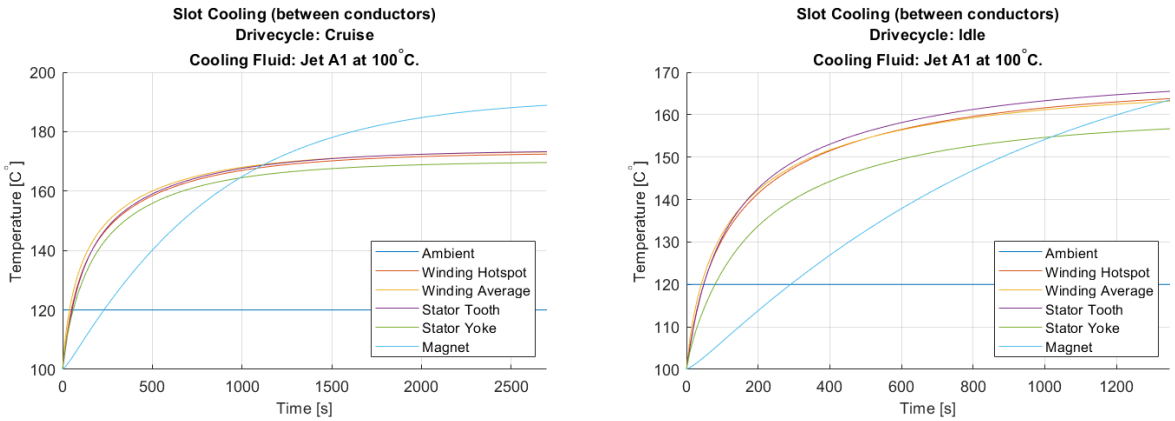

Figure 84: Transient thermal simulation of slot cooling between conductors using Jet A1 Fuel as coolant.

5.2.2 Increase of Cooling Surface Area

In the case of a cooling sleeve outside the stator, which is assumed as the cooling topology for the MGU011 machine, the cooling surface area plays a crucial role in heat transfer performance. By increasing the surface area the cooling performance should theoretically increase which is simulated in Motor-CAD with the given drive cycles from GKN.

The effective cooling surface area can be estimated as:

$$A_{\text{surface}} = \pi D_{\text{so}} l_{\text{stk}} \tag{5.1}$$

Where D_{so} is the outer diameter of the stator. By varying the so called aspect ratio of the machine which is defined as the length to diameter ratio ($\frac{l_{\text{stk}}}{D_{\text{so}}}$), the impact on increasing surface area can be evaluated.

Since the output torque of the machine can be estimated rearranging the shear stress expression given in Equation (2.51), which indicates that torque is proportional to $D_r^2 l_{stk}$ seen in:

$$T = \frac{\sigma \pi D_{\text{r}}^2 l_{\text{stk}}}{2} \tag{5.2}$$

An increase in diameter would mean a quadratic increase in torque. To maintain the same output torque as the original design, the stack length must therefore decrease quadratically with an increasing diameter. Since the surface area is linearly proportional to the stack length, an increase in machine diameter results in a decrease in outer surface area if the torque should remain unchanged. Therefore, in order to increase the cooling surface area, the stack length is increased, meaning an increase in aspect ratio. By selecting an arbitrary value of 250 mm for the stack length, the rotor diameter has to decrease in order to keep the same output torque and is calculated by:

$$D_{\text{r}} = \sqrt{\frac{2T}{\pi \sigma l_{\text{stk}}}} = \sqrt{\frac{2 \cdot 140}{\pi \cdot 35000 \cdot 0.250}} = 0.101 \tag{5.3}$$

With a new rotor diameter of 101 mm (18 mm smaller than in the original design) and a stack length extended by 70 mm, other dimensions of the machine must be adjusted accordingly. By keeping the same

winding dimensions, the slot dimensions remains unchanged. However, the reduced rotor diameter limits the available space for the permanent magnets. Therefore the dimensions of the magnets has to decrease in width and depth while the magnet length is increased due to the stack length increase.

To ensure that the magnetic flux linkage remains comparable to that of the original design, a no-load simulation is performed. The magnet dimensions are iteratively calibrated during this simulation until the resulting flux linkage matches that of the reference of 52 mVs. The resulting dimensions of the machine are listed in **Table 21** and the geometry is illustrated in **Figure 85**.

Table 21. Dimensions of the stack length modified machine.

Dimension	Value	Unit
Machine Outer Diameter (D_m)	192	mm
Machine Length (l_m)	310	mm
Housing Thickness ($w_{housing}$)	20	mm
Stator Outer Diameter (D_{so})	152	mm
Stator Bore Diameter (D_{si})	103	mm
Stack Length (l_{stk})	250	mm
Rotor Diameter (D_r)	101	mm
End Windings Length (l_{EW})	23	mm
Air Gap Length (g)	1	mm
Slot Depth (d_{ss})	15.5	mm
Slot Width (w_{ss})	4.8	mm
Magnet Depth (d_m)	3	mm
Magnet Width (w_m)	15	mm

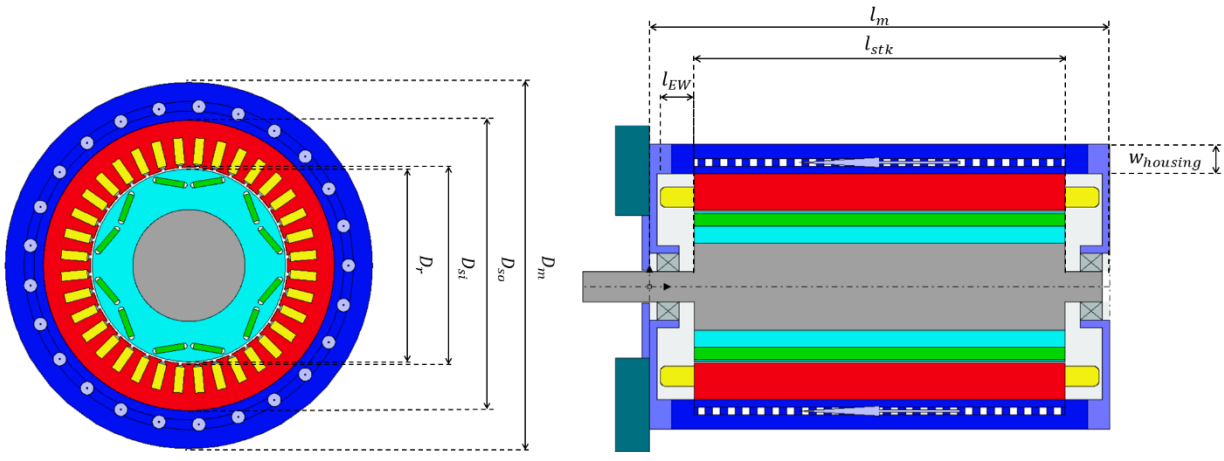

Figure 85: Radial and axial cross section view of the MGU011 Motor-CAD Model with increased aspect ratio.

This dimension modification results in an increase of surface area given by:

$$A_{original} = \pi \cdot 170 \cdot 180 \approx 96133\ mm^2 \tag{5.4}$$

$$A_{new} = \pi \cdot 152 \cdot 250 \approx 119381\ mm^2 \tag{5.5}$$

Which is an area increase of 24.2 %.

The thermal simulation result is presented in **Figure 86**.

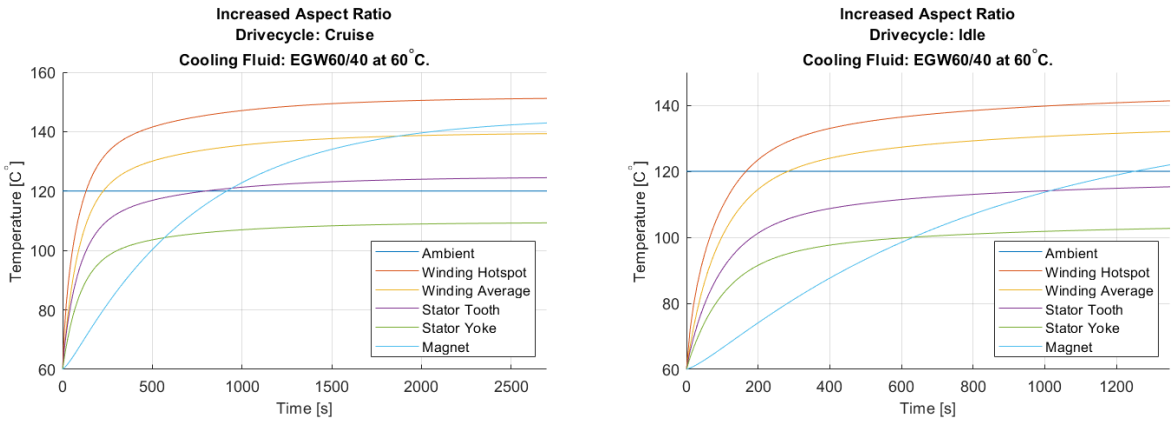

Figure 86: Transient thermal simulation of the model with increased aspect ratio using EGW60/40 Fuel as coolant.

This modification of the machine results in a slightly better cooling performance, especially for the windings which temperature decrease approximately with 10 °C. A drawback with the increased stack length is the winding resistance which increases. Due to the increased machine length, the winding length also increases, resulting in a phase resistance of $6.2\ \mathrm{m\Omega}$, approximately 24 % greater than in the original design of $5\ \mathrm{m\Omega}$ which increases the DC losses and therefore the heat generation. However, since the cooling surface area is increased, it seems to transfer the heat enough to compensate for the increased DC-losses.

5.2.3 Samarium Cobolt Magnets

In order to withstand the thermal stress from operating at high temperatures without demagnetizing the magnets, one option is to change the magnetic material. As mentioned in the Section 2.1.3.2, one alternative is the use of Samarium Cobalt magnets which has a higher coercivity and Curie temperature.

Using the approximated geometry of the Magneti Marelli machine in Motor-CAD and only change the magnets from NeFeB30H to SmCo26H reduces the permanent magnetic flux since the remanet flux of SmCo26H is lower than NeFeB30H. By performing a no-load operation simulation and measuring the resulting flux linkage, the *d*-axis flux linkage, corresponding to the permanent magnet flux, was observed to decrease from 52 mVs to 45 mVs.

As an effect of the decrease in flux linkage the output torque will decrease and in order to compensate for this loss, the magnet size has to increase. The magnet dimensions to keep a flux linkage of 52 mVs are listed in **Table 22** and are based on experimental iterations running no-load simulations in the Motor-CAD.

Table 22. Magnet dimensions to achieve a *d*-axis flux linkage of 52 mVs.

Magnet Material	Width [mm]	Depth [mm]	Length [mm]	Volume $[\mathrm{m}^3]$	Density $[\mathrm{kg/m}^3]$	Weight "Single Magnet" [kg]	Weight "All Magnets" [kg]
N30UH	19.1	3.5	180	1.2033e-5	7500	0.09	1.08
SmCo26H	21	4,2	180	1.5876e-5	8400	0.133	1.60

Increasing the magnet size to compensate for the lower remanence of SmCo compared to NdFeB results in an approximate volume increase of 45 %. Since the magnets are embedded within the rotor core, this increase in magnet volume has a corresponding reduction effect in the volume of rotor core material. Assuming the rotor core is made of M350-50A electrical steel with a density of 7650 $\mathrm{kg/m}^3$, the effective magnet weight increase is roughly 15 % instead of 45 %. Since the magnets is relatively small compared to the rest of the components in the machine, the overall weight increase of the electric machine is only 0.3 % going from 38.84 kg to 38.97 kg.

5.3 Full Simulink Simulation Model

This section presents the results from the full Simulink simulation model. Section 5.3.1 shows the simulation results of the two reference drive-cycles. Section 5.3.2 presents the simulation results of two different tests to verify the over-modulation strategy. Finally the results of the thermal simulation model is presented in Section 5.3.3.

5.3.1 Drive-cycle test

Two different drive-cycles examples (or flight missions as they are called in the aviation industry), that represents the cruise phase of a flight and machine running in idle, were used. These drive-cycle examples, which can be seen in **Table 18**, consists of cruise, which runs at a speed of 17000 rpm and a torque of 56.2 Nm and, idle, which has a speed of 12750 rpm with a torque of 74.9 Nm.

Both drive-cycles examples are simulated with the machine running in linear modulation and six-step modulation. The simulated machine and power electronics can handle both drive-cycles without having to enter over-modulation. In order to force the model to run in six-step operation at the same speed U_{dc} was lowered to 270 V as explained in 3.4.1.

5.3.1.1 *Cruise – peak efficiency*

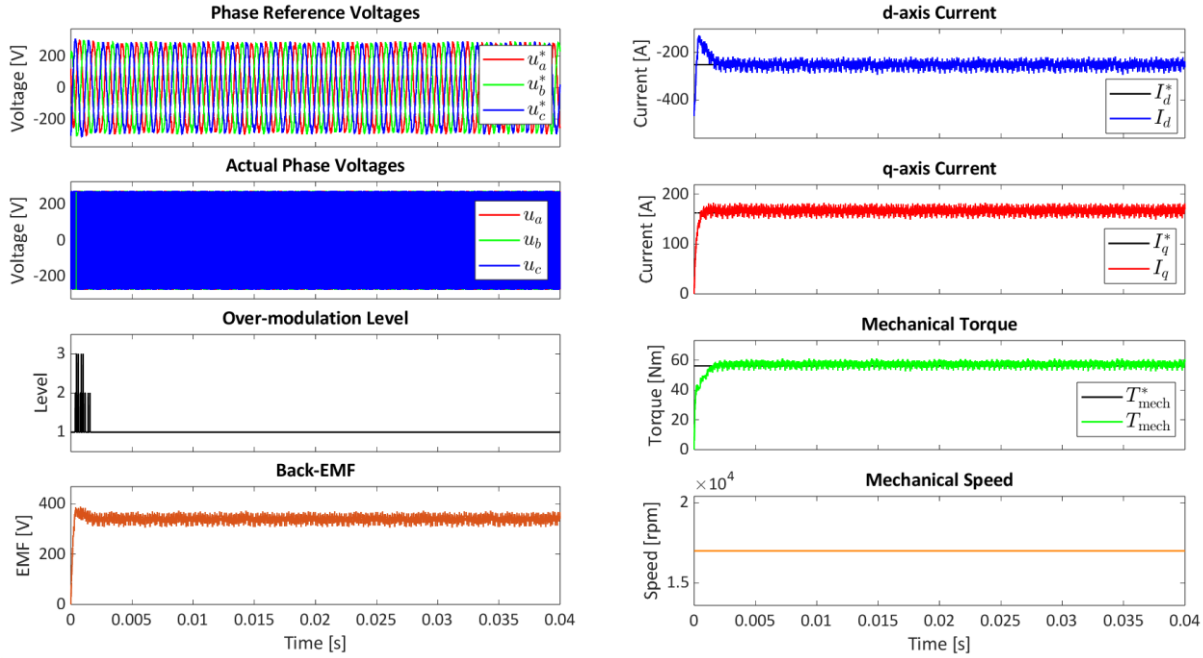

Figure 87: Drive-cycle: Cruise. 540 V DC-bus voltage.

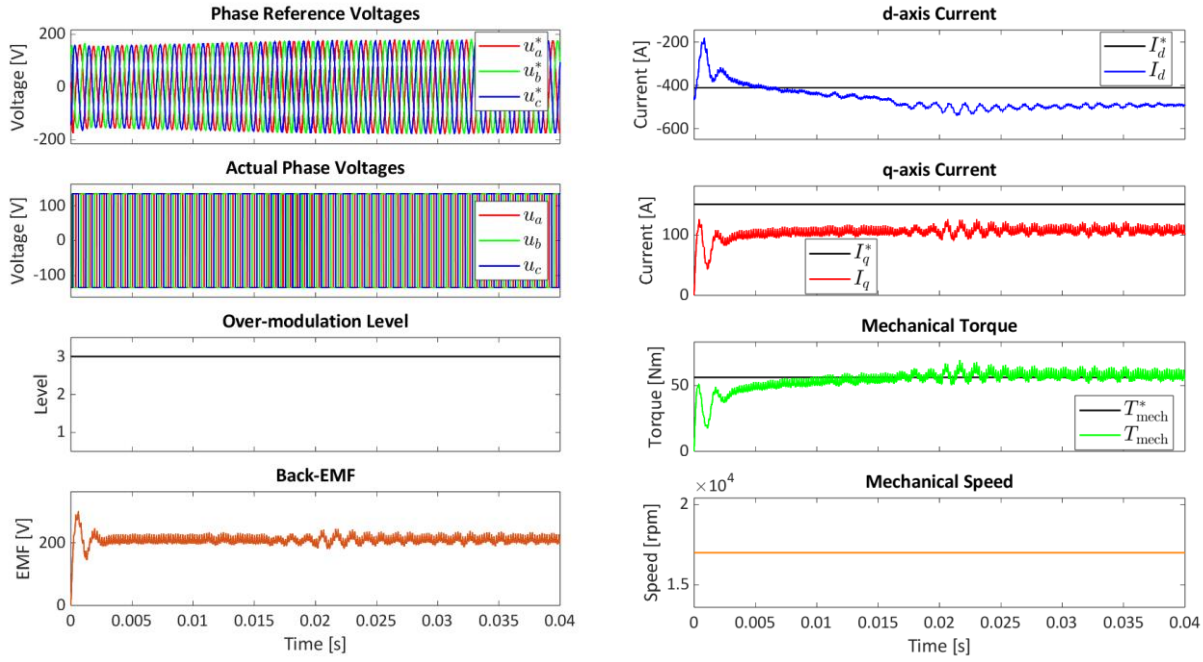

Figure 88: Drive-cycle: Cruise. 270 V DC-bus voltage in six-step modulation.

5.3.1.2 SLS – idle

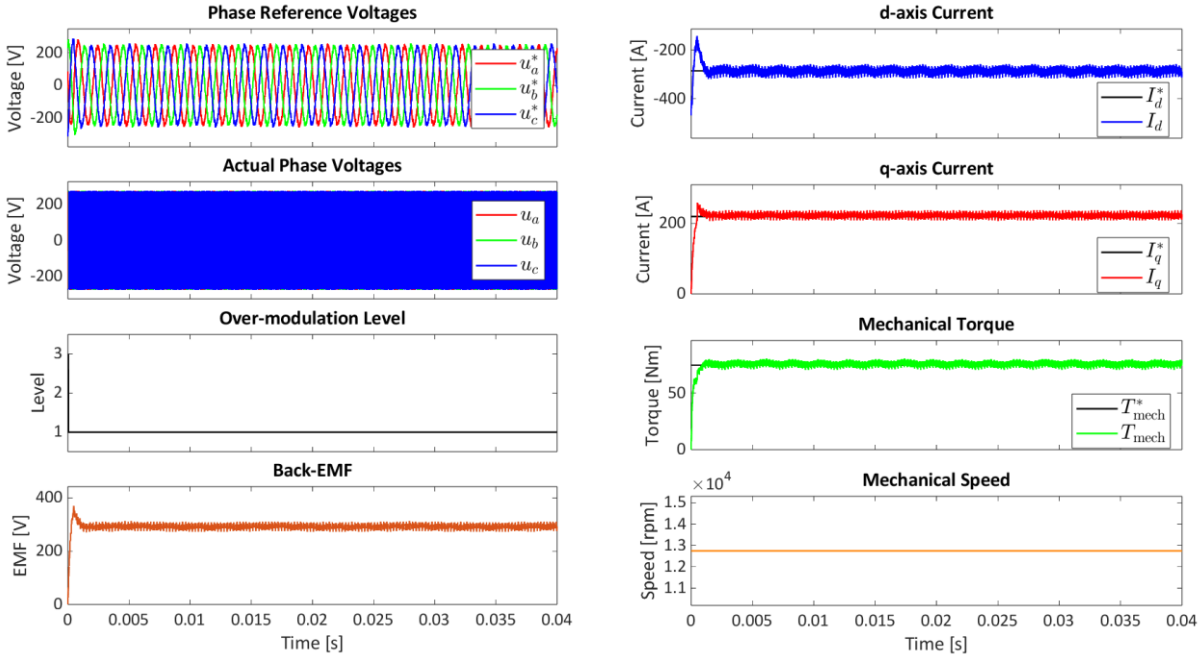

Figure 89: Drive-cycle: Idle. 540 V DC-bus voltage.

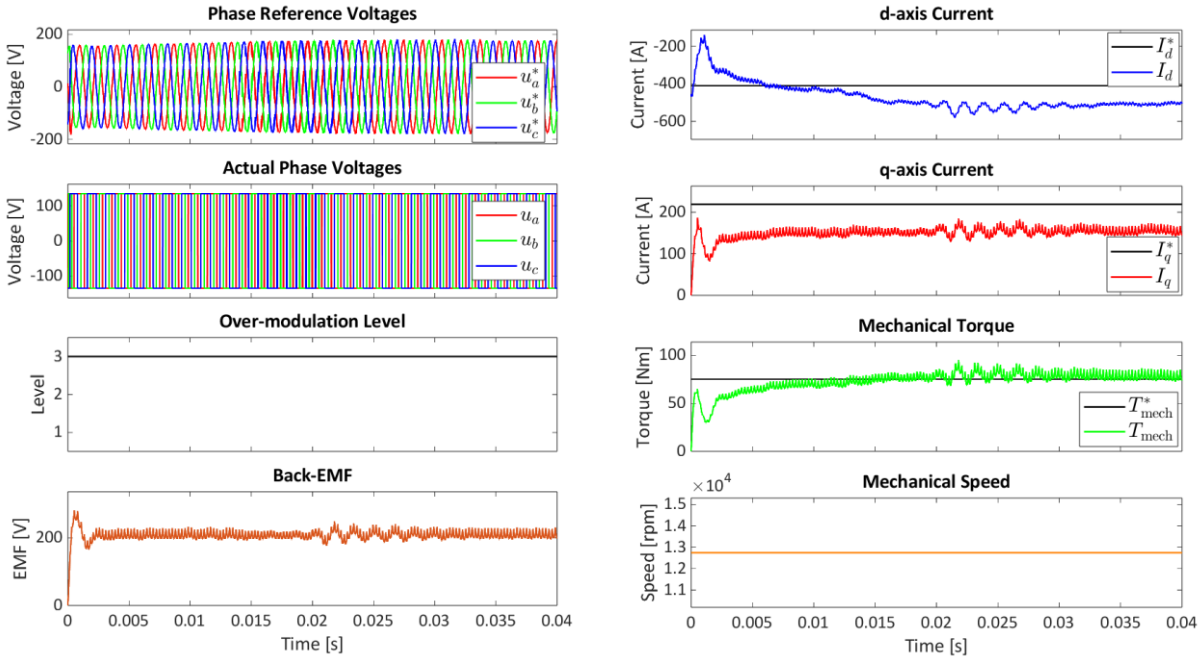

Figure 90: Drive-cycle: Idle. 270 V DC-bus voltage in six-step modulation.

5.3.2 Linear to Six-step test

To test if the model can go from linear modulation to six-step modulation, two different drive-cycles were used. Since the point of the tests is to go into six-step U_{dc} is decreased to 270 V. The first drive-cycle ramped up the speed from 0 rpm to 17000 rpm over a period of 0.01 s, held it at 17000 rpm for another 0.01 s and then ramped it down again with a constant torque of 70 Nm. The drive-cycle can be seen in **Table 23** and the **Figure 91** shows the reference voltage, over-modulation level (where 1 is linear, 2 is the transition between linear and six-step and 3 is six-step), mechanical torque, mechanical speed, *d*- and *q*-axis current and back-EMF is plotted through the drive-cycle.

The second drive cycle jumped from 7000 rpm to 16000 rpm, back down to 7000 rpm and then back up to 16000 rpm, all while holding 0 Nm of torque. The drive-cycle can be seen in **Table 24** and the plot that shows the reference voltage, over-modulation level, mechanical torque, mechanical speed, *d*- and *q*-axis current and back-EMF is shown in **Figure 93**. There are also plots for the second drive-cycle that show the α- and β-axis voltages and the α-, β-, *d*- and *q*-axis currents at different parts of the drive-cycle, which can be seen in **Figure 94** to **Figure 97**.

Finally, **Figure 98** shows a plot of how the reference and actual voltage in the transition from linear modulation to six-step modulation.

Table 23: Drive-cycle 1 for the over-modulation test.

Duration [s]	Torque [Nm] [start]	Torque [Nm] [end]	Speed [rpm] [start]	Speed [rpm] [end]
0.01	70	70	0	17000
0.01	70	70	17000	17000

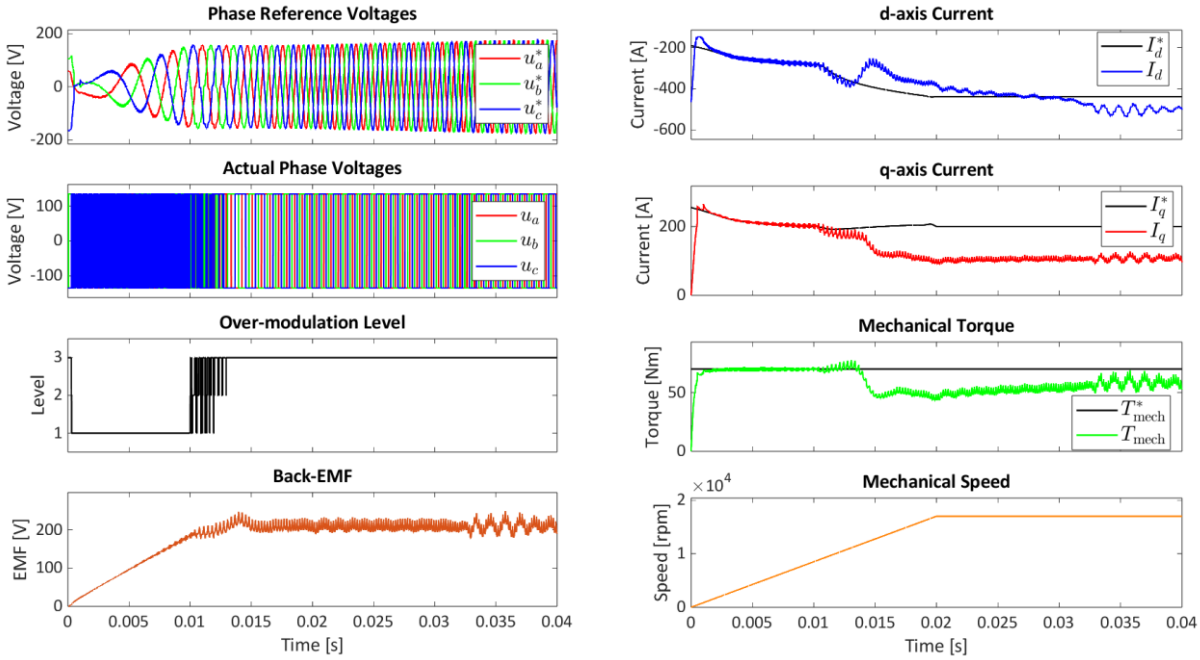

Figure 91: Plot of drive-cycle 1 for the over-modulation test.

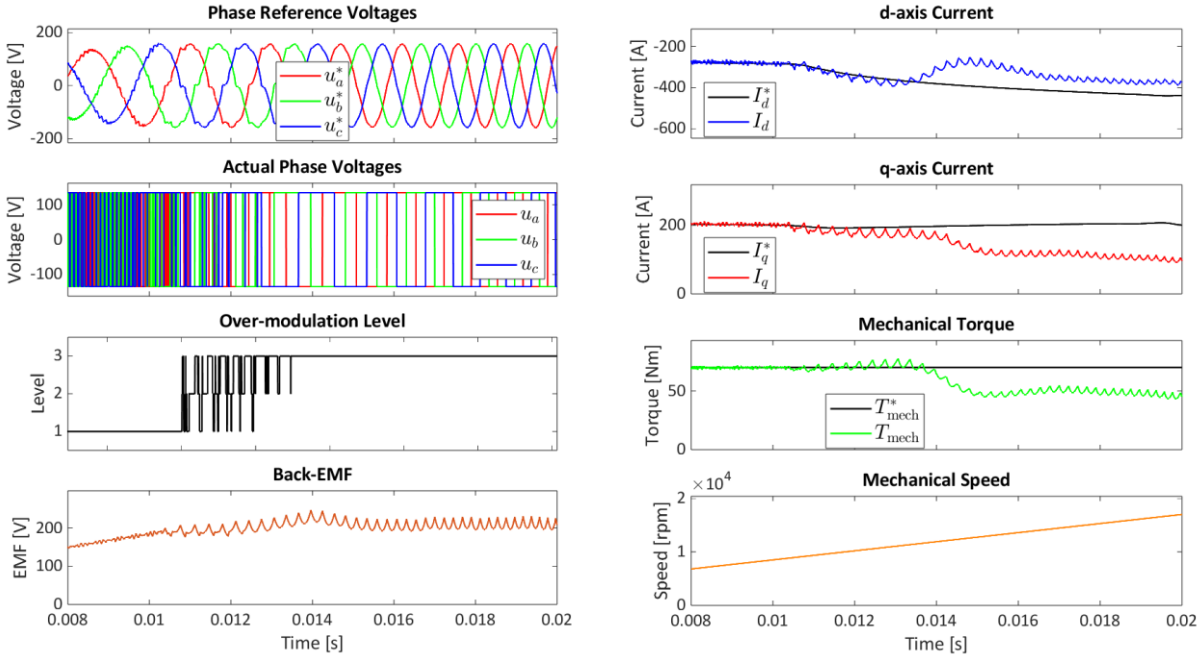

Figure 92: Plot of drive-cycle 1 for the over-modulation test, zoomed in.

Table 24: Drive-cycle 2 for the over-modulation test.

Duration [s]	Torque [Nm] [start]	Torque [Nm] [end]	Speed [rpm] [start]	Speed [rpm] [end]
0.01	0	0	7000	7000
0.01	0	0	16000	16000
0.01	0	0	7000	7000
0.01	0	0	16000	16000

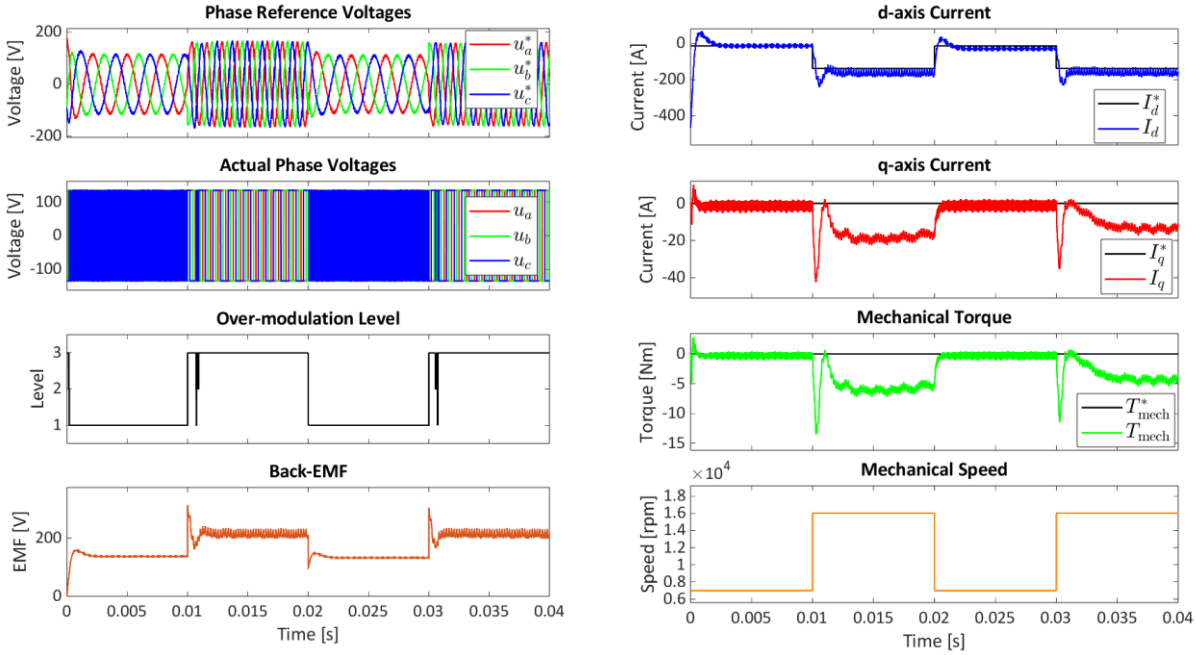

Figure 93: Plot of drive-cycle 2 for the over-modulation test.

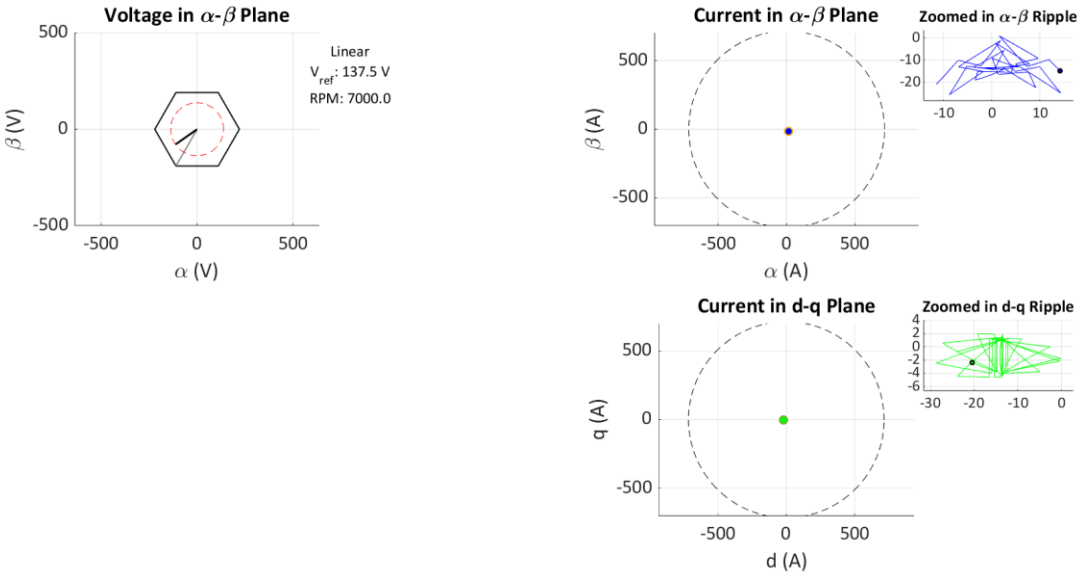

Figure 94: α-, β-axis voltages and, α-, β-, *d*- and *q*-axis currents at 0 s - 0.01 s.

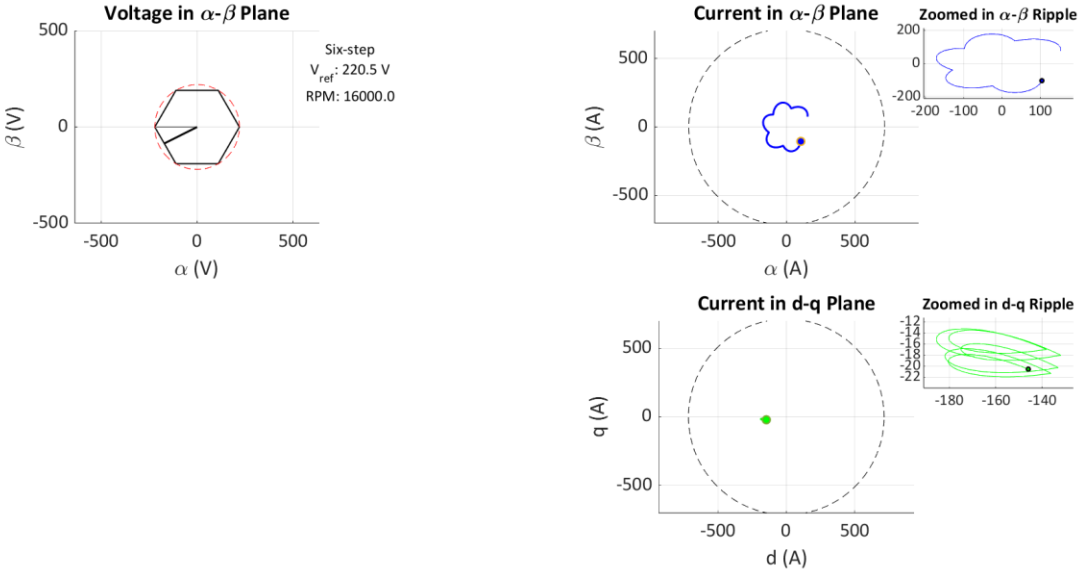

Figure 95: α-, β-axis voltages and, α-, β-, *d*- and *q*-axis currents at 0.01 s - 0.02 s.

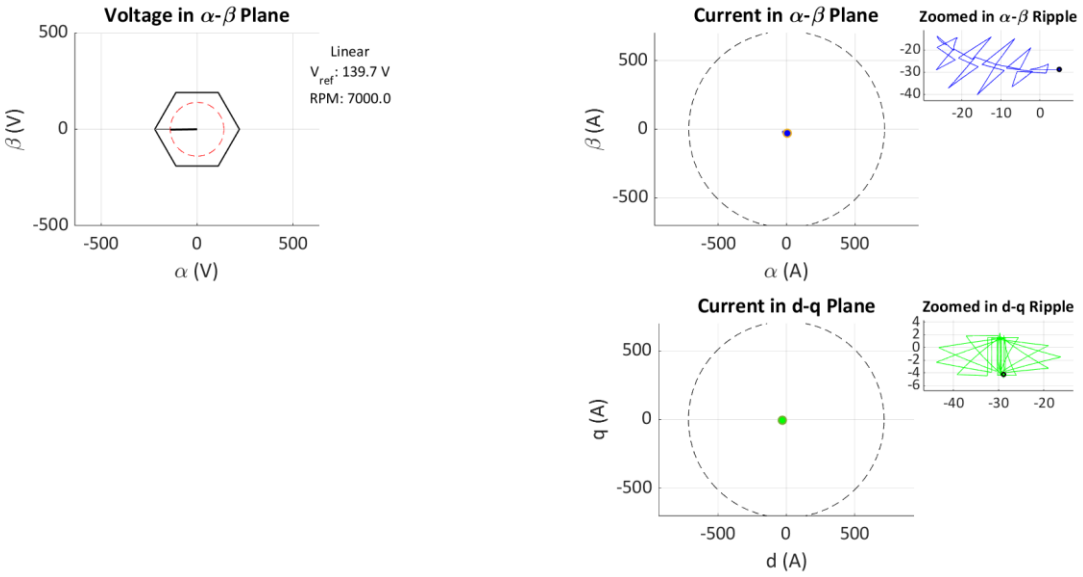

Figure 96: α-, β-axis voltages and, α-, β-, *d*- and *q*-axis currents at 0.02 s - 0.03 s.

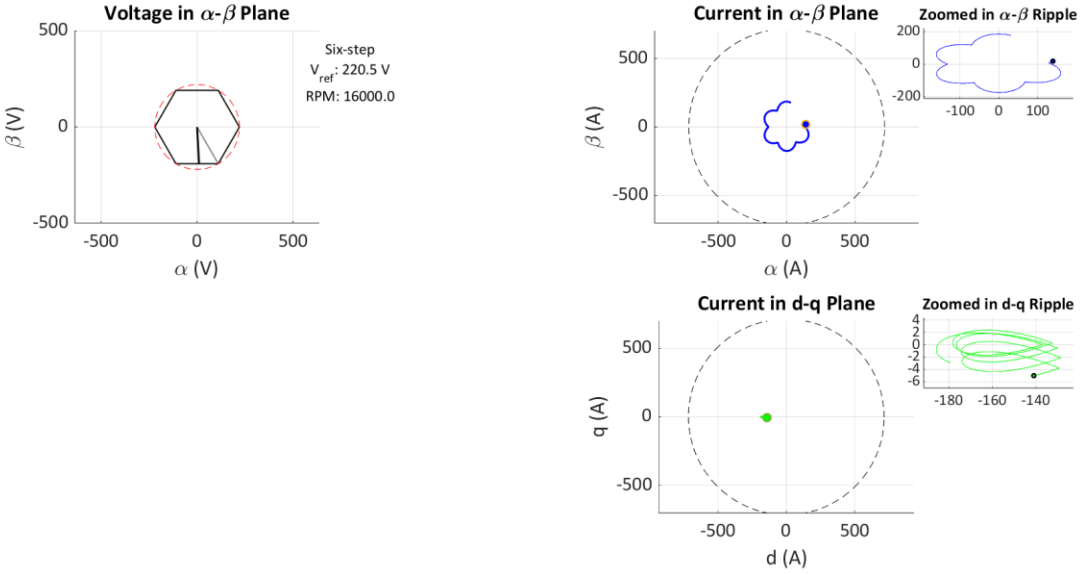

Figure 97: α-, β-axis voltages and, α-, β-, *d*- and *q*-axis currents at 0.03 s - 0.04 s.

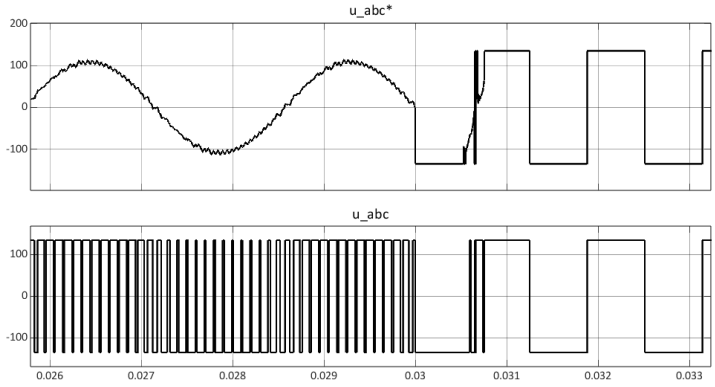

Figure 98: Reference voltage (u_abc*) and actual voltage (u_abc) during transition from linear modulation to six-step modulation.

5.3.3 Thermal model

In **Table 25** to **Table 28** the maximum thermal resistance is presented for each transistor type. For IGBT the highest thermal resistance was simulated without the temperature exceeding that specific transistors limit during switching conditions ($T_{\mathrm{vj\ op}}$ in formula sheets). This temperature limit is 125 ℃ for IGBTs and 175 ℃ for SiC. After the thermal resistances are presented, they will be compared to different commercial heat-sinks to see how the results compare to real heat-sinks.

Table 25: Maximum simulated thermal resistance for drive-cycle: cruise with linear modulation.

Cooling fluid temperature [℃]	IGBT [℃/W]	SiC (FF6) [℃/W]	SiC (FF1) [℃/W]
20	0.0875	0.0825	0.4
60	0.0425	0.05	0.29

Table 26: Maximum simulated thermal resistance for drive-cycle: cruise with six-step modulation.

Cooling fluid temperature [℃]	IGBT [℃/W]	SiC (FF6) [℃/W]	SiC (FF1) [℃/W]
20	0.05	0.025	0.235
60	0.019	0.007	0.165

Table 27: Maximum simulated thermal resistance for drive-cycle: idle with linear modulation.

Cooling fluid temperature [°C]	IGBT [°C/W]	SiC (FF6) [°C/W]	SiC (FF1) [°C/W]
20	0.0875	0.0825	0.4
60	0.0425	0.05	0.29

Table 28: Maximum simulated thermal resistance for drive-cycle: idle with six-step modulation.

Cooling fluid temperature [°C]	IGBT [°C/W]	SiC (FF6) [°C/W]	SiC (FF1) [°C/W]
20	0.0425	0.019	0.21
60	0.015	0.002	0.15

6 DISCUSSION

This section reflects on the results of the simulations of both the PMSM and the power electronics. It is divided in a discussion about the PMSM model alignment with the measurements as well as how the modified PMSM models performs. Furthermore, the component of the power electronics are compared and discussed as well as the performance of the control strategy. Lastly, the key sources of uncertainties during the project are discussed.

6.1 PMSM Model Validation

The model validation of the Motor-CAD and Simulink model of the PMSM in Section 5.1 shows that the models align relatively well with the measurements conducted on the MGU011.

In **Table 12**, there are some minor deviations in the output torque between the models and the measurements. However, the desired output torque from the system requirements is still achievable, but with other current combinations due to the different inductances in the model. With losses and thermal behavior in the Motor-CAD model being relatively close to the measured machine, it serves as a relatively good representation of the real machine. To get an even more accurate model in Motor-CAD of the machine, the internal geometry and materials are required.

However, the Simulink model should have the possibility to represent the real machine with relatively high accuracy in absence of internal geometry and material specification since it is based on the mathematical model which does not take geometry and materials into account. By measuring the voltages at different operating points with constant currents, the inductances of the machine can be calculated by Equation (3.25) and (3.26). With these inductances, look-up tables for the real machine can be built which would give a more accurate model in terms of output torque for given current combinations.

The most significant deviation between the simulation models and real measurements is the estimation of iron losses in the Simulink model. The iron losses are difficult to analytically calculate since it is dependent on saturation effects and varying flux densities within the stator core. Therefore, the Simulink model does not represent the iron losses very well.

The other approach of estimating the iron losses based on measurements at different operational points may be more convenient for achieving more accurate iron loss estimations. This could be done creating a look-up table with iron losses for different torque and speed combinations. Since the iron losses measured was measured during no load, no torque could be applied which makes it hard to map the iron losses to different operating points.

The thermal models, Simulink and Motor-CAD based, align well with each other but has an overall lower temperature compared to the measurements of the reference machine as seen in **Table 17** and in the figures in the Section 9.2. It is possible to experimentally modify the cooling sleeve in Motor-CAD and from that get an even more accurate thermal behavior but since the model is based on many assumptions, the thermal results seem to be good enough for analyzing different cooling strategies.

6.2 Electric Machine Sensitivity Analysis Insights and Design Recommendations

The sensitivity analysis of the electric machine reveals significant differences in thermal performance between the two cooling fluids, jet A1 fuel and EGW 60/40, as seen in Section 5.2.1. Jet A1 fuel, due to its relatively low thermal conductivity and specific heat capacity, is less effective as a cooling medium, particularly at an operating temperature of 100 °C. As a result, maintaining the temperature below the thermal limits with Jet A-1 alone is challenging.

To enable the use of jet fuel as a coolant, it would be necessary to replace some temperature sensitive materials within the machine. For instance, samarium cobalt (SmCo) magnets present a viable alternative to neodymium based magnets, as they offer a substantially higher maximum operating temperature, approximately 350 °C, which exceeds the maximum magnet temperatures observed in all simulations. Additionally, S2 fiberglass is a promising candidate for winding insulation in this context, given its ability to withstand temperatures up to 425 °C. However, S2 fiberglass is not currently available as a commercially established winding insulation material and may present challenges in terms of manufacturability and implementation.

If more conventional solutions are used, the use of the water glycol mixture becomes necessary to ensure that operating temperatures remain within thermal limits. With the water-glycol mixture as coolant, all evaluated cooling topologies, except for slot cooling at the tooth tip, were able to maintain temperatures below the critical thresholds. However, given that the thermal models tend to overestimate the machine's heat dissipation compared to measurement data, the only cooling strategy that can be expected, with a reasonable degree of confidence, to keep the machine within thermal constraints is slot cooling implemented between the conductors seen in **Figure 82**.

In Section 5.2 the cooling performance of different cooling topologies and cooling fluids are shown. By utilizing temperature tolerant materials in combination with the water-glycol mixture as coolant, a thermal margin between approximately 160-180 °C for the magnets and 265-325 °C for the winding insulation can be achieved, depending on the cooling topologies employed. This thermal headroom enables the possibility of increasing the current density which, although it leads to higher thermal losses due to increased DC losses, increases the torque density due to the higher current. By maintaining the same output torque, this increased torque density is expected to allow for a reduction in machine volume, thereby effectively reducing the overall mass of the machine. By keeping the thermal headroom may lead to an increased redundancy since the material are not operating at its maximum working temperature.

6.3 Component Selection

Simulation models of power electronics heat-sinks, as mentioned in section 3.4.5, do exist. However their properties, especially the thermal resistance, depends on a number of different factors. The resistance and capacitance can be characterized from the shape and size of the heat-sink, not taking convection into account. But the air-flow as well as the cooling fluid has a huge effect on the resulting cooling capabilities of the heat-sink. In order to present a result that can be used for future development of the model the maximum thermal resistance of the heat-sink is presented is simulated, to handle a given drive-cycle with a certain transistor with either linear modulation or six-step modulation. This can be used to test the model with other drive-cycles, transistors or modulation schemes, but also when modeling heat-sink. A discrete thermal resistive value can be used when researching this topic in the future. **Table 25**, **Table 26**,

Table 27 and **Table 28** shows the results of these simulations and the values vary greatly depending on the transistor used.

The SiC transistor FF1MR12KM1HP outperform all others in all drive-cycles for both linear modulation and six-step. The maximum thermal resistance allow for the heat-sink in order to keep the temperature at the requirements ranged from 0.15 ℃/W to 0.4 ℃/W.

In linear operation the IGBT and the SiC FF6MR12KM1H model gives pretty similar results. But in over-modulation the IGBT outperformed. With the IGBT the heat-sink would have to have a maximum thermal resistance of 0.0875 ℃/W to 0.015 ℃/W depending on drive-cycle and modulation.

The worst performer is the SiC FF6 MR12KM1H. It gives, as previously mentioned, similar results to the IGBT in linear modulation but in six-step modulation it performs so poorly that it is unfeasible to cool it. The maximum thermal resistance of 0.0825 ℃/W to 0.002 ℃/W, with the latter coming from a simulation in the idle drive-cycle with six-step modulation and 60 ℃ of cooling fluid temperature. A thermal resistance of 0.002 ℃/W is unrealistic when looking at available heat-sinks from suppliers, even when looking at forced cooling [36].

The big difference in cooling requirements for the SiC FF6 compared to the IGBT is partly due to the characteristics of the SiC transistor, a lower switching time decreases the power lost and thereby heat created, but also due the fact that SiC transistors can operate under higher temperature than IGBTs can. The maximum temperature under switching conditions for the SiC transistors is 175 ℃ but the IGBT can only operate at 125 ℃. SiC FF6 outperforms SiC FF1 in due to its faster switching, which decreases switching losses, and its lower internal resistance, which decreases conduction losses.

6.4 Control Strategy

The control strategy to transition from linear to six-step worked and the simulation model can run in both linear and six-step modulation as shown in section 5.3. However, a comparison of different control strategies is suggested in order to improve the control algorithm. The initial idea was to try to come up with a control strategy that contributes to the existing solution given in [31]. Developing a strategy without inspiration from published literature turned out to be an ambitious goal and the final design contains a combination of new ideas that were developed by testing and designs from already published literature in [31], where the saturation and scaling in the current controller, seen in **Figure 36**, as well as the linear to six-step block in the modulation block, seen in **Figure 40**, was the our idea. Article [31] contributed with the field weakening controller.

Even though the model can transition between the two types of modulation, it has to be further developed in order to call the transition “smooth”. Looking at the reference voltage in **Figure 98**, the transition from sinusoidal to square wave gives rise to transient (as can be seen between 0.03 s and 0.031 s of **Figure 98**). This does not make the transition between linear modulation and over-modulation as smooth as anticipated. An early idea was to alter both the magnitude and angle of the voltage reference signal and by doing that decreasing the transients when switching to six-step. Unfortunately, this was unsuccessfully developed for this thesis which is why only the magnitude is controlled. Angle alteration is used widely in over-modulation strategies [31] and should be investigated further before ruling it out.

Another problem that was found was how the look-up tables, which output reference currents in d- and q-axis from reference torque and reference speed, should be handled in six-step operation. When entering six-step the look-up tables could no longer be used since they were made under linear modulation conditions. The solution to this was the field-weakening block in the current control sub-system. This field-weakening, explained in Section 3.4.2.2, only limited the current when the total current exceeded what is allowed by the converter and when it did, it prioritized the *d*-current in order to counter the back-EMF and then redirected the rest of the available current to the *q*-axis. This gave the current controller the control it needed to regulate the voltage and current, even in six-step. In **Figure 88** and **Figure 90** a static error can be seen between the reverence current and the actual current in both the d- and the q-axis. This is because, in six-step modulation, the model tries to push the machine to its absolute limits and the reference currents don't know the limits of the actual currents. What is important is that the model still should be able run the drive-cycle without losing control of the currents.

6.5 Sources of Uncertainty

Throughout this thesis, several sources of uncertainty have been identified that may influence the accuracy of the results. These uncertainties are primarily due to limited access to detailed documentation and experimental measurements such as machine dimensions, voltage and loss measurements during different operational points. As a result, a number of assumptions were required in the development and validation of the simulation models. The following section outlines and discusses the most significant uncertainties encountered during the project.

6.5.1 MGU011 Internal Geometry

As the MGU011 machine from Magneti Marelli was used as the reference, the simulation models were developed based on this machine. However, due to the lack of verified documentation regarding its internal geometry and the lack of possibility to measure the dimensions of the machine, the model development relied heavily on a series of assumptions. The picture of the inside geometry of the MGU012, shown in **Figure 21**, was found on the web [30]. While the source of this model provides limited documentation and cannot be fully verified, it served as a valuable initial approximation.

Access to detailed drawings or verified design data would likely enhance the accuracy of the modeled machine characteristics, resulting in closer alignment with the actual machine performance.

6.5.2 Simulink Simulation Models

When trying to represent the real world in a simulation, there will always be factors that cannot be determined. Many uncertainties must be taken into account when analyzing the results, especially since the simulation results could not be verified. One component of a converter that is hard to parameterize is the transistors themselves. Just like any other component, they have tolerances. The characteristics that describe them, taken from a formula sheet, only represent the specific transistors that were tested to create the formula sheet under the specific conditions when the tests were made. Components also age as they are heated up and cooled down again, which makes their values drift. For example, for SiC,

the body diode can get an increased forward voltage and on-resistance [37]. For IGBTs the biggest concern is a decrease in breakdown voltage [38].

Another uncertainty concerns the thermal model. Making a first order equivalent circuit model thermal conduction each for three transistors pairs, the thermal grease and the heat-sink is substantial simplification. In order to create an accurate model of a heat-sink, material properties, geometric details, convective heat transfer, radiative heat transfer and fluid properties of the cooling fluid is needed. Since this cooling system is part of a bigger cooling system integrated with other sub-system in the aircraft the whole cooling system and the other subsystems need to be parameterized in order to make a model of this.

6.5.3 Measurement Data

As one of the reference machines were unavailable during most of the project, it was not possible to gather all measurements needed to actually validate the models towards the real machine as accurate as planned. Without a braking machine acting as a load on the shaft, it was not possible to test different operational points since no output torque can be held constant. Therefore it was hard to characterize the machine.

However, there were some measurements conducted at different operational points before one of the machines became unavailable. Those measurements included torque and speed for different current references shown in **Table 10** but did not include any measurements with the power analyzer. Hence it was hard to use for characterization due to the missing voltage measurements. With measurements of the voltages during certain operational points, more accurate look-up tables of the inductances would be possible to achieve, hence the model would align more with the reference machine.

The measurements conducted with the power analyzer shown in **Table 14** was a bit uncertain since it was struggling finding a voltage reference due to the strong flux weakening effect with high negative *d*-axis current. Hence, it displayed unrealistic values from time to time and therefore, only a few measurements were chosen as valid. When the machine operated at 15050 rpm a significant increase in total losses was observed. This deviation from the expected trend of loss increase with speed may be due to a measurement error.

The position of the temperature sensors inside the MGU011 are unknown. This uncertainty makes it difficult to be certain on the validation between the model temperature and the actual measurements since the measured temperatures could be at a different location.

When measuring the coolant flow in the test rig, a very simple method was conducted which gave a very rough estimation of flow. Since the water used for cooling was from the tap and the flow was manually set. It may vary between the different tests. For more accurate measurements a flow sensor would be convenient during test.

The coolant temperature was also estimated to be 10 degrees since it varies from day to day depending on the temperature in the water pipes and the outside temperature. For a better result, temperature sensors at the inlet and outlet of the machine would increase the accuracy of the thermal measurements.

7 CONCLUSION

This thesis presents the model development and simulation of a PMSM and the power electronics with its control algorithm driving the PMSM between linear and six-step modulation. In addition, two thermal models are developed to simulate the heat generation and transfer within the PMSM and transistor modules. The models are using Simulink in order to connect the PMSM model with the power electronics and analyze the synergy between those models. However, to get a more accurate representation of the PMSM, Motor-CAD is used to develop a geometry based model of the machine which could be analyzed utilizing finite element analysis to estimate the core losses with higher accuracy. The Motor-CAD model also enables evaluation of different cooling topologies with its thermal models.

In the Simulink model for the electrical drive system, it is found that the chosen approach for the over-modulation strategy is successful in being able to go from linear modulation to six-step. Even though the approach works, there is room for improvements and further research in this area has the possibility for a smoother transition between the two modulation modes. The PMSM model in Simulink is showing a good alignment with the Motor-CAD model but requires an improved iron loss estimation in order to get an accurate machine representation. With more extensive measurement data from the real machine, the PMSM model has the possibility to align with greater accuracy to the physical machine since the inductances can be calculated and the iron losses can be fitted to the measured losses.

In the thermal simulation model of the transistor module it is found that switching to SiC transistors significantly decreases the need for cooling compared to IGBTs. This is partly due to the faster switching time that of the SiC but also the fact that SiC can operate under higher temperature 175 ℃ instead of 125 ℃.

The thermal simulations of the PMSM conducted in Motor-CAD shows that the use of Jet A1 fuel as coolant is not feasable if conventional magnet and insulation materials are used. However, by incorporating more temperature resistant materials, such as Samarium Cobalt magnets and S2 glassfiber, it seems achievable to use Jet Fuel as coolant. Nevertheless, by instead using the water glycol mixture as coolant a significantly improved heat transfer performance is achieved, resulting in a greater thermal margin. This additional margin can be exploited to either keep the materials far from their maximum operating temperature, leading to longer lifetime and thereby increasing the redundancy of the machine. The thermal headroom also allows the machine to operate at higher temperatures, which can be utilized to redesign the machine to allow for higher current density or reducing the needed cooling, thereby decreasing the size of the machine or cooling system.

Therefore, to answer the research question about what thermal management strategies are necessary to ensure a reliable operation of a PMSM in aircraft environments with the limited access to effective cooling fluids. The combination of a water-glycol mixture and temperature-tolerant materials is concluded to be the most suitable solution for this application. By using direct contact cooling through the slots shows the most effective thermal performance but may be difficult to implement. By instead using a more conventional spiral sleeve together with an increased aspect ratio shows a thermal performance still under the temperature limitations and is simpler to implement.

The current control algorithm, which can go from linear modulation to six-step modulation and work in the transition region in between the two states, can be implemented by limiting the voltage reference

amplitude until the voltage reference magnitude becomes high enough for the algorithm to enter six-step modulation. In order to be able to control the currents when the reference voltage cannot be increased further, a field weakening controller (which can be seen in **Figure 37**) is used. The field weakening controller makes sure that, when the voltage magnitude has reached its limit, the d-current is prioritized in order weaken the back-EMF and thereby remain in control of the currents.

The cooling capabilities needed in order for the converter to operate without the transistors exceeding their maximum operating temperature, depends a lot on the transistor used. Where a converter with the best performing transistor (SiC FF1) only requires a small heat sink, even at very high currents. However, a converter using the worst performing transistor (SiC FF6) requires a heat sink with a very low thermal resistance, when used in linear modulation. A converter with Si CFF6 is unfeasible to cool when used in over-modulation.

8 FUTURE WORK

This chapter outlines possible directions for future research and development building on the insight gathered while doing this thesis. Section 8.1 covers the electric machine and what can be improved and further investigated in that area. Section 8.2 goes into the possibilities of the power electronics and what potentially can be improved. What can be done when it comes to the control strategy is covered in Section 8.3.

8.1 Electric Machine

To improve the PMSM Simulink model, the loss estimation method should be further developed in order to get more accurate loss estimation. This requires more measurement data of the MGU011 to fit the loss model to the actual machine. Furthermore, if the Simulink model is the simulation environment to be used for future research in this topic, the thermal model needs to be further developed. In its current state, the model does not take the ambient or magnet temperature into account, which are important to evaluate the machine's thermal performance and limitation.

The primary objective of the PMSM model development was to create a simulation model that replicates the performance of the MGU011. In aiming to mirror the characteristics of the MGU011, certain design parameters, such as permanent magnet flux, pole-slot combinations, and winding configurations, were held constant and not included in the sensitivity analyses. However, to identify an optimal machine design for the intended generator application, these parameters requires further investigation and analysis.

Additionally, a topic initially considered in the project planning, but later omitted due to time constraints, involved investigating a PMSM configuration with dual three-phase stator windings. Incorporating such a design into the Simulink model enables evaluating operation with two independent control systems, thereby enhancing system redundancy in the event of a failure. However, this configuration introduces additional complexity, and the electromagnetic cross-coupling between the windings must be thoroughly evaluated to understand the machine's behavior under fault conditions.

8.2 Electrical System

In order to reach higher currents, voltages and thereby more power in electrical systems in the aviation industry, it is essential to use new components that can handle the higher demands. As the field of semiconductors evolves, so will the electrical power generation of aircrafts. In this thesis the only comparison made is between IGBTs and two different types of SiC transistors. There are of course a wide range of transistor models, including GaN and other SiC models than those used in this thesis, to evaluate for the future electrical systems of aviation.

A topic that was not researched in this thesis is the use of multilevel converters. The converters of the electrical system used in this thesis has two levels, made up of 2 transistors per phase. Using 4 transistors per phase instead of two halves the current ripple and lowers the losses, since they partly depend on the voltage difference over the transistor being opened or closed. There are also cascade-coupled converters where there is a built-in redundancy in each phase. If one transistor were to brake, the only thing that

would happen is that that specific phase becomes level is reduced by one (e.g. that one phase of a 3-level converter becomes a 2-level).

8.3 Control Strategy

Even though the final control strategy was harder to develop than first expected which meant that there was not enough time to follow through with the original plan and evaluate different control strategies compare them to each other, the results still show the value in conducting that comparison in the future. The final results show that the control works, but leaves something to be desired. With the full simulation model as a foundation, there are a lot of possibilities to develop and evaluate other ways of controlling the current in advanced modulation schemes.

9 APPENDIX

9.1 Thermal Network Parameters

Table 29: Estimated internal dimensions of MGU011

Parameter name	Value	Unit	Description
w_{st_ave}	7.4	mm	Stator average tooth width
w_{sy}	9	mm	Stator yoke width
w_{ss}	4.8	mm	Stator slot width
d_{ss}	15.5	mm	Stator slot depth
h_{cu}	12	mm	Winding depth (including all conductors)
w_{cu}	3.8	mm	Winding width
ins	0.1	mm	Insulaion thickness
$liner$	0.3	mm	Liner thickness
$slot\_airgap$	0.1	mm	Airgap between liner and stator core
WJ_airgap	0.01	mm	Airgap between yoke and cooling sleeve
WJ_lam	5	mm	Water jacket thickness

Table 30: Material properties used for thermal modelling.

Parameter	*Value*	Unit	Description
λ_{cu}	401	W/°C	Copper thermal conductivity
λ_{core}	30	W/°C	M350-50A thermal conductivity
λ_{alu}	168	W/°C	Aluminium thermal conductivity
λ_{ins}	0.21	W/°C	Insulation thermal conductivity
λ_{liner}	0.21	W/°C	Liner thermal conductivity
λ_{air}	0.032	W/°C	Air thermal conductivity

Table 31. Thermal resistances.

Thermal Resistances	Calculation
$R_{winding_{tangential}}$	$\frac{\frac{w_{\mathrm{cu}}}{2}}{\lambda_{\mathrm{cu}} \cdot h_{\mathrm{cu_{tot}}} \cdot l_{\mathrm{stk}}}$
$R_{ins_{tangential}}$	$\frac{l_{\mathrm{ins}}}{\lambda_{\mathrm{ins}} \cdot (d_{\mathrm{ss}} - liner) \cdot l_{\mathrm{stk}}}$
$R_{liner_{tangential}}$	$\frac{l_{\mathrm{liner}}}{\lambda_{\mathrm{liner}} \cdot d_{\mathrm{ss}} \cdot l_{\mathrm{stk}}}$
$R_{airgap_{tangential}}$	$\frac{l_{\mathrm{airgap}}}{\lambda_{\mathrm{liner}} \cdot d_{\mathrm{ss}} \cdot l_{\mathrm{stk}}}$

$R_{tooth_{tangential}}$	$\frac{\frac{\overline{w}_{\mathrm{st}}}{2}}{\lambda_{\mathrm{core}} \cdot \frac{d_{\mathrm{ss}}}{2} \cdot l_{\mathrm{stk}}}$
$R_{tooth_{radial}}$	$\frac{\frac{d_{\mathrm{ss}}}{2}}{\lambda_{\mathrm{core}} \cdot \frac{\overline{w}_{\mathrm{st}}}{2} \cdot l_{\mathrm{stk}}}$
$R_{winding_{radial}}$	$\frac{\frac{h_{\mathrm{cu_{tot}}}}{2}}{\lambda_{\mathrm{cu}} \cdot \frac{w_{\mathrm{cu}}}{2} \cdot l_{\mathrm{stk}}}$
$R_{ins_{radial}}$	$\frac{l_{\mathrm{ins}}}{\lambda_{\mathrm{ins}} \cdot \frac{w_{\mathrm{cu}}}{2} \cdot l_{\mathrm{stk}}}$
$R_{liner_{radial}}$	$\frac{l_{\mathrm{liner}}}{\lambda_{\mathrm{liner}} \cdot \frac{w_{\mathrm{cu}}}{2} \cdot l_{\mathrm{stk}}}$
R_{yoke}	$\frac{w_{\mathrm{sy}}}{\lambda_{\mathrm{core}} \cdot \frac{\overline{w}_{\mathrm{st}} + w_{\mathrm{ss}}}{2} \cdot l_{\mathrm{stk}}}$
$R_{CoolingSleeve}$	$\frac{WJ_{\mathrm{lam}}}{\lambda_{\mathrm{alu}} \cdot \frac{\overline{w}_{\mathrm{st}} + w_{\mathrm{ss}}}{2} \cdot l_{\mathrm{stk}}}$

Table 32. Thermal Capacitances.

Thermal Masses	Calculation
$C_{winding}$	$h_{\mathrm{cu_{tot}}} \cdot \frac{w_{\mathrm{cu}}}{2} \cdot (l_{\mathrm{stk}} + EW_{\mathrm{MLT}}) \cdot \rho_{\mathrm{cu}} \cdot C_{\mathrm{p_{cu}}}$
C_{tooth}	$\frac{\overline{w}_{\mathrm{st}} \cdot d_{\mathrm{ss}} \cdot l_{\mathrm{stk}}}{2} \cdot \rho_{\mathrm{core}} \cdot C_{\mathrm{p_{core}}}$
C_{yoke}	$\frac{\overline{w}_{\mathrm{st}} + w_{\mathrm{ss}}}{2} \cdot w_{\mathrm{sy}} \cdot l_{\mathrm{stk}} \cdot \rho_{\mathrm{core}} \cdot C_{\mathrm{p_{core}}}$

9.2 Drive Cycle Temperature Measurements and Simulations

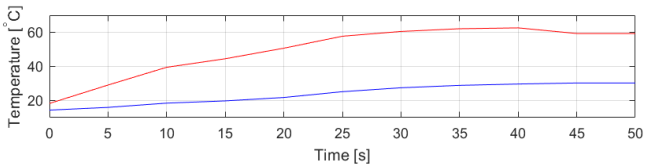

Figure 99: Temperature measurement of MGU011 during Drive Cycle 1.

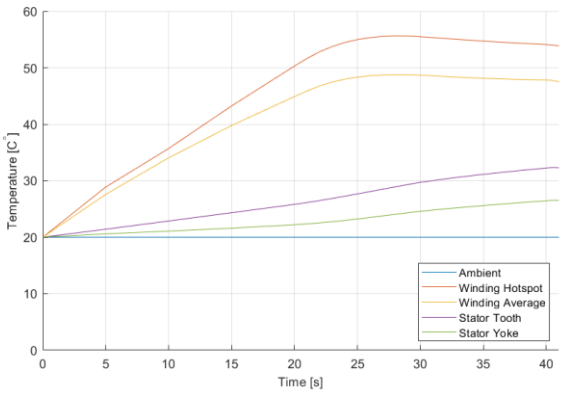

Figure 100: Motor-CAD thermal simulation of Drive Cycle 1.

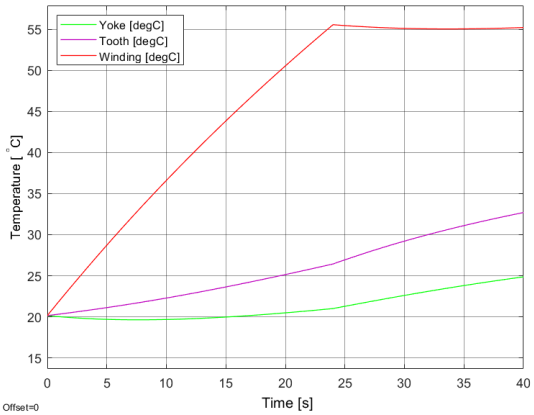

Figure 101: Simulink thermal simulation of Drive Cycle 1.

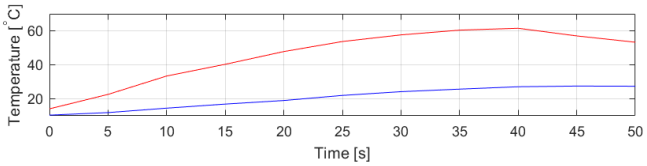

Figure 102: Temperature measurement of MGU011 during Drive Cycle 2.

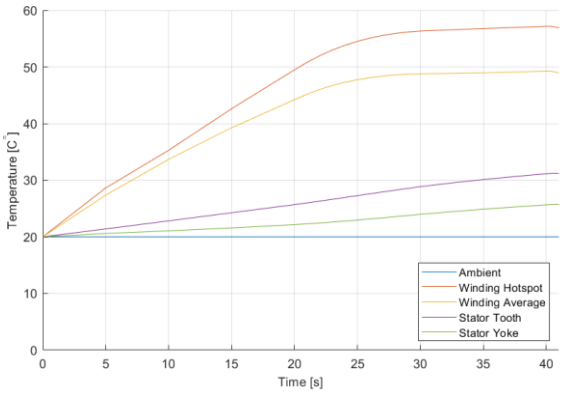

Figure 103: Motor-CAD thermal simulation of Drive Cycle 2.

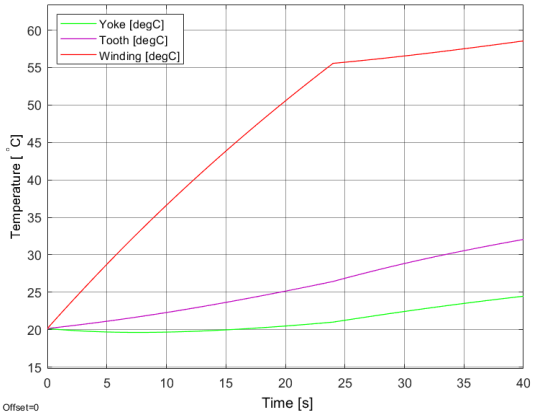

Figure 104: Simulink thermal simulation of Drive Cycle 2.

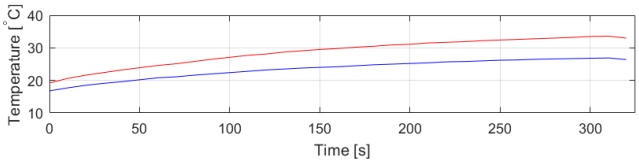

Figure 105: Temperature measurement of MGU011 during Drive Cycle 3.

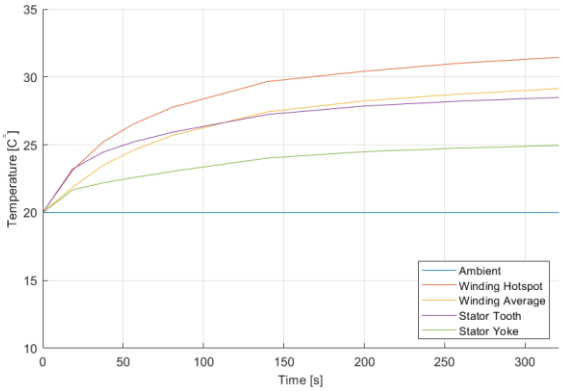

Figure 106: Motor-CAD thermal simulation of Drive Cycle 3.

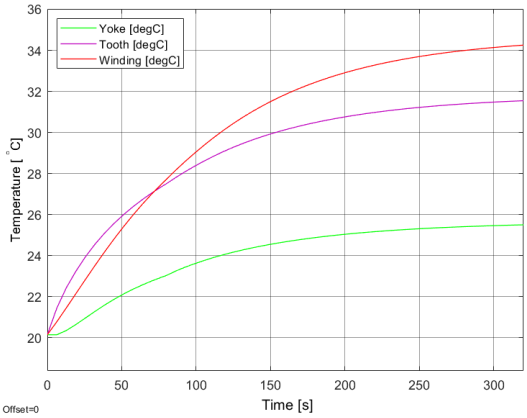

Figure 107: Simulink thermal simulation of Drive Cycle 3.

10 REFERENCES

[1] P. Wheeler, G. Buticchi and D. Boroyevich, "The More-Electric Aircraft and Beyond," *Proceedings of the IEEE*, vol. 111, no. 4, pp. 356-370, 2023.

[2] A.-F. Reyad, E. Ahmad and A.-S. Mazen, "ELECTRICAL DISTRIBUTION POWER SYSTEMS," in *International Conference on Energy Systems and Technologies*, Cairo, 2013.

[3] D. V. Muños, "Design, Simulation and Implementation of a PMSM Drive System," Chalmers University of Technology, Göteborg, 2011.

[4] Lecture Slides - General Theory of Electric Machines, *Lecture Slides - General Theory of Electric Machines*, Shiraz: Shiraz University of Technology, 2017.

[5] M. Alaküla, P. Karlsson and H. Bäntsson, Power Electronics - Devices, Converters, Control and Applications, Lund: Lund University, 2019.

[6] F. F. Jaber and A. F. Abdulhasan, "Mathematical Model of Permanent Magnet Synchronous Motor," in *Vol. 12 No. 2 (2022): Special Issue Proceedings of the 6th International Scientific Conference on Advanced Medical and Engineering Technologies (ISC-AMET 2022)*, Thi-Qar, 2022.

[7] S. Hall, F. J. Márquez-Fernández and M. Alaküla, "Dynamic Magnetic Model Identification of Permanent Magnet Synchronous Machines," *IEEE Transactions on Energy Conversion*, vol. 32, no. 4, pp. 1367-1375, 2017.

[8] W. Han, "Simulation Model Development of Electric Motor and Controller," Chalmers University of Technology, Gothenburg, 2017.

[9] V. Levisdottir, "Investigation of Loss Clculation Methods for PMSMs and Implementation of Loss Functionality on a Developed FEM Model," Norwegian University of Science and Technology, Trondheim, 2016.

[10] A. J. Fard, "ComProgExpert," [Online]. Available: https://comprogexpert.com/pdfs/Introductory%20Course%20on%20Design%20of%20V-Type%20IPM%20Motors.pdf.

[11] J. Hendershot and T. Miller, "Design of brushless Permanent-Magnet Machines," in *Design of brushless Permanent-Magnet Machines*, Venice, Magna Physics Publishing & Oxford University Press, 2022, pp. 144-148.

[12] Electrical4U, "Winding Factor, Pitch Factor, Distribution Factor," [Online]. Available: https://www.electrical4u.com/winding-factor-pitch-factor-distribution-factor/. [Accessed 22 April 2025].

[13] . A. Kačenka, A.-C. Pop, I. Vintiloiu and D. Fodorean, "Lumped Parameter Thermal Modeling of Permanent Magnet Synchronous Motor," in *2019 Electric Vehicles International Conference (EV)*, Bucharest, 2019.

[14] B. Andersson, "Lumped Parameter Thermal Modelling of Electric," Chalmers University of Technology, Göteborg, 2013.

[15] W. Limited, "Welkon.net," [Online]. Available: https://www.welkon.net/downloads/insulation_(temperature)_classes.pdf.

[16] G. W. Wires, "Basics of winding wires," [Online]. Available: https://gkwinding.com/blogs/basics-of-winding-wires/. [Accessed 10 June 2025].

[17] K. Tshiloz, A. C. Smith, P. M. Tuohy and T. Feehally, "Investigation of wire insulation for high-temperature motor windings," *The Journal of Engineering*, vol. 2019, no. 17, pp. 4442-4445, 2019.

[18] S. Magnets, "Standford Magnets," 16 April 2024. [Online]. Available: https://www.stanfordmagnets.com/maximum-operating-temperature-vs-curie-temperature.html. [Accessed 16 April 2025].

[19] G. Martinek, S. Ruoho and U. Wyss, "Magnetic Properties of Permanent Magnets & Measuring Techniques," 2025. [Online]. Available: https://www.arnoldmagnetics.com/wp-content/uploads/2021/11/White-Paper-Measurement-07.23.2021MS2a4.pdf. [Accessed 15 04 2025].

[20] E. M. Ltd., "Samarium Cobalt Magnets Datasheet," [Online]. Available: https://www.eclipsemagnetics.cn/site/assets/files/2418/samarium_cobalt_magnets_datasheet.pdf. [Accessed 15 April 2025].

[21] I. magnets, "How does cold affect magnets?," [Online]. Available: https://imamagnets.com/productos/en/blog/how-does-cold-affect-magnets/. [Accessed 10 June 2025].

[22] Y. Yongheng and Z. Keliang, "Modeling and Control of Single-Phase AC/DC Converters," in *Control of Power Electronic Converters and Systems*, Aalborg, Academic Press, 2018, pp. 93-115.

[23] A. Haque, "AC-DC converters (rectifiers)," in *Electric Renewable Energy Systems*, New Dehli, Academic Press, 2016, pp. 313-336.

[24] A. Kumar, M. Moradpour, M. Losito, W.-T. Frenke, S. Ramasamy, R. Baccoli and G. Gatto, "Wide Band Gap Devices and Their Application in Power Electronics," *Energies,* vol. 15, no. 23, 2022.

[25] R. Palanisamy, V. Thangamani Santhakumari, S. Venkatarajan, S. Hemalatha, A. Alice Hepzibah, R. Ramkumar and V. Sugavanam, "Space vector pulse width modulation reallization for three-phase voltage source inverter," *Indonesian Journal of Electrical Engineering and Computer Science*, vol. 36, no. 3, pp. 1976-1984, 2024.

[26] K. Zhou and D. Wang, "Relationship Between Space-Vector Modulation and Three-Phase Carrier-Based PWM: A Comprehensive Analysis," *IEEE Transactions on Industrial Electronics* , vol. 40, no. 1, pp. 186-196, 2002.

[27] M. Alaküla, *Presentation slide: KE1_L6_(3PhaseModulation),* Lund: Lund University, 2024.

[28] K. Gopikrishnan and S. Pramanick, "A Simple Two-zone Overmodulation Implementation for Three-Phase Two-Level Inverters," in *25th European Conference on Power Electronics and Applications*, Aalborg, Denmark, 2023 .

[29] S. Jung and J.-I. Ha, "Low Voltage Modulation Method in Six-step Operation of Three Phase Inverter," in *9th International Conference on Power Electronics-ECCE Asia*, Seoul, Korea, 2015.

[30] EHFCV, "EHFCV," 14 October 2013. [Online]. Available: https://ehfcv.com/mgu-and-hispd-technology/.

[31] K. Yong-Cheol, K. Sungmin and S. Seung-Ki, "Six-Step Operation of PMSM With Instantaneous Current Control," *IEEE Transactions on Industry Applications*, vol. 50, no. 4, pp. 2614-2625, 2014.

[32] M. Alaküla, *Modulator block in Simulink*, Lund: Mats Alaküla, 2025.

[33] Semikron, "Semikron," 03 07 2013. [Online]. Available: https://assets.danfoss.com/documents/latest/511448/AI498149497069en-000102.pdf. [Accessed 10 06 2025].

[34] Infineon, "Infineon," 17 03 2023. [Online]. Available: https://www.infineon.com/dgdl/Infineon-FF6MR12KM1H-DataSheet-v00_10-EN.pdf?fileId=8ac78c8c8afe5bd0018b18a31aa537a2. [Accessed 10 06 2025].

[35] Infineon, "Infineon," 27 02 2023. [Online]. Available: https://www.infineon.com/dgdl/Infineon-FF1MR12KM1HP-DataSheet-v00_30-EN.pdf?fileId=8ac78c8c8afe5bd0018b18a4c20537c8. [Accessed 10 06 2025].

[36] DigiKey, "Heat Sinks | Thermal | Electronic Components Distributor DigiKey," DigiKey, 26 05 2025. [Online]. Available: https://www.digikey.se/en/products/filter/thermal/heat-sinks/219. [Accessed 26 05 2025].

[37] C. Zijun , L. Mingen , Z. Dongsheng, H. Shengdong, S. Yijun, F. Shuanzhu , Z. Jianlin, C. Yiqiang and L. Guoguang , "Bipolar Degredation of SiC MOSFET Body Diode Under Constant Current Stress," in *25th International Conference on Electronic Packaging Technology (ICEPT)*, Tianjin, 2024.

[38] F. Zeng, D. Su, R. Chen, Q. Yao, L. Li and J. Tang, "Effect of Thermal Oxidative Aging on Cross-Linking Network and Electrical Property of Silicone Gel for IGBT Packaging," *IEEE Transactions on Dielectrics and Electrical Insulation*, vol. 31, no. 2, pp. 1012-1019, 2024.

[39] N. Urasaki, T. Senjyu and K. Uezato, "An Accurate Modeling for Permanent Magnet Synchronous Motor Drives," in *APEC 2000. Fifteenth Annual IEEE Applied Power Electronics Conference and Exposition*, New Orleans, 2000.

[40] A. Rahideh, *General Theory of Electric Machines*, Shiraz: Shiraz University of Technology, 2017.

[41] A. Sangwongwanich, A. Abdelhakim, Y. Yang and K. Zhou, "Control of SIngle-Phase and Three-Phase DC/AC Converters," in *Control of Power Electronic Converters and Systems*, Academic Press, 2018, pp. 153-173.

[42] C. Kizowski, S. Budzik and J. Cebulski, "Finding the Curie Temperature for Ferromagnetic Materials," *The Physics Teacher*, vol. 45, no. 1, pp. 31-33, 2007.